

The Spectral Signature of Cloud Spatial Structure in Shortwave Radiation

by

Shi Song

B.S., Nanjing University, China 2007

M.S., Nanjing University, China 2010

A thesis submitted to the

Faculty of the Graduate School of the

University of Colorado in partial fulfillment

of the requirement for the degree of

Doctor of Philosophy

Department of Atmospheric and Oceanic Sciences

2016

This thesis entitled:

The Spectral Signature of Cloud Spatial Structure in Shortwave Radiation
written by Shi Song

has been approved for the Department of Atmospheric and Oceanic Sciences

Dr. K. Sebastian Schmidt

Dr. Peter A. Pilewskie

Date _____

The final copy of this thesis has been examined by the signatories, and we find that both the content and the form meet acceptable presentation standards of scholarly work in the abovementioned discipline.

Song, Shi (Ph.D., Atmospheric and Oceanic Sciences)

The Spectral Signature of Cloud Spatial Structure in Shortwave Radiation

Thesis directed by Professor K. Sebastian Schmidt

In this thesis, we aim to systematically understand the relationship between cloud spatial structure and its radiation imprints, i.e., three-dimensional (3D) cloud effects, with the ultimate goal of deriving accurate radiative energy budget estimates from space, aircraft, or ground-based observations under spatially inhomogeneous conditions. By studying the full spectral information in the measured and modeled shortwave radiation fields of heterogeneous cloud scenes sampled during aircraft field experiments, we find evidence that cloud spatial structure reveals itself through spectral signatures in the associated irradiance and radiance fields in the near-ultraviolet and visible spectral range.

The spectral signature of 3D cloud effects in irradiances is apparent as a domain-wide, consistent correlation between the magnitude and spectral dependence of net horizontal photon transport. The physical mechanism of this phenomenon is molecular scattering in conjunction with cloud heterogeneity. A simple parameterization with a single parameter ε is developed, which holds for individual pixels and the domain as a whole. We then investigate the impact of scene parameters on the discovered correlation and find that it is upheld for a wide range of scene conditions, although the value of ε varies from scene to scene.

The spectral signature of 3D cloud effects in radiances manifests itself as a distinct relationship between the magnitude and spectral dependence of reflectance, which cannot be reproduced in the one-dimensional (1D) radiative transfer framework. Using the spectral signature in radiances and irradiances, it is possible to infer information on net horizontal photon transport from spectral radiance perturbations on the basis of pixel populations in sub-domains of a cloud scene.

We show that two different biases need to be considered when attempting radiative closure between measured and modeled irradiance fields below inhomogeneous cloud fields: the remote sensing bias (affecting cloud radiances and thus retrieved properties of the inhomogeneous scene) and the irradiance bias (ignoring 3D effects in the calculation of irradiance fields from imagery-based cloud retrievals). The newly established relationships between spatial and spectral structure lay the foundation for first-order corrections for these 3D biases within a 1D framework, once the correlations are explored on a more statistical basis.

Dedication

To all of my family, for your unconditional and everlasting love.

In particular, to my father, for your constant encouragement and inspirations. From you I learned to “enjoy the present moment,” which I find invaluable for my everyday life.

Also, to my mother, for your selfless and limitless care and support. Knowing that you are forever by my side always gives me tremendous courage to pursue my dreams.

Lastly, to my teacher Master Zhen-Ru. I am where I am and who I am all because of you. Had it not been for your guidance, company, and loving kindness, it would have been impossible for me to walk peacefully in this world, let alone make any achievement as a scientist or as a human.

Acknowledgement

I am wholeheartedly grateful to my research advisor, Professor K. Sebastian Schmidt, for his amazingly patient, humble, compassionate, and wise guidance at every single step along my Ph.D. journey. I am indebted to Sebastian for his mentorship and support, his scientific, career, and life advising, and all the coffee and tea throughout these years. I would also like to express my deep gratitude towards my academic advisor, Professor Peter Pilewskie, for initially leading me into this wonderland of clouds and radiation, as well as constantly challenging me to “think big.” I am thankful to all past and present members of the Atmospheric Radiation Group: Michael King, Scott Kittelman, Bruce Kindel, Odele Coddington, Patrick McBride, Yolanda Roberts, Samuel LeBlanc, Andrew Kren, Steven Massie, Logan Wright, Sabrina Cochrane, and Hong Chen. Your kindness, help, support, and constructive discussions are much appreciated.

I have been fortunate to participate in many field missions where I witnessed how scientists, engineers, pilots, administrative managers, and supporting staff join their efforts to advance our knowledge of nature. I would like to express my deep respect towards all the individuals who have helped and inspired me during these times.

I reserve a special expression of appreciation for Dr. Hironobu Iwabuchi who is currently a professor at the Center for Atmospheric and Oceanic Studies of Tohoku University, Japan. A number of important findings we made over the past four years were

based on the three-dimensional radiative transfer model—the Monte Carlo Atmospheric Radiative Transfer Simulator (MCARaTS)—that Dr. Iwabuchi developed. He patiently addressed countless questions regarding radiative transfer modeling over emails and in person, for which I am truly thankful.

I would like to also thank my dearest friend and mentor, Antonia L. Johnson, for all her advice on accent reduction, grammar, punctuation, life, and spirit. She has a genuine talent for initiating inspirational conversations. Talking to her is one of the greatest enjoyments in my life.

Wholeheartedly, I would like to thank all my mentors and friends at P151 of GWBI: Venerable Yvonne, Venerable Sabrina, Tanya, Linda, Tina, Yufan, Cadence, and Careen, for your wealth of guidance and endless support throughout the last year of my Ph.D. Having you in my life has been a great honor.

Finally, I would like to acknowledge the faculty of the Department of Atmospheric and Oceanic Sciences. Thank you for your dedication to teaching.

Contents

Chapter 1 Introduction	1
1.1 Motivation	1
1.2 Terms and definitions	5
1.3 Field experiments, instruments, and data	6
1.3.1 Tropical Composition, Cloud and Climate Coupling Experiment (TC ⁴ , 2007).....	8
1.3.2 Studies of Emissions and Atmospheric Composition, Clouds and Climate Coupling by Regional Surveys (SEAC ⁴ RS, 2013)	9
1.3.3 Solar Spectral Flux Radiometer (SSFR).....	10
1.3.4 SSFR data processing	12
1.4 Three-dimensional radiative transfer model and input parameters	14
1.4.1 Monte Carlo Atmospheric Radiative Transfer Simulator (MCARaTS)	15
1.4.2 Spectral surface albedo	17
1.4.3 Henyey-Greenstein phase function in the irradiance calculation	19
 Chapter 2 The spectral signature of cloud spatial structure in shortwave irradiance	 22
2.1 Introduction.....	22
2.2 Net horizontal photon transport and cloud radiative effect	25
2.3 Cloud Data.....	30

2.3.1 Sub-scene from ER-2 passive and active remote sensors	30
2.3.2 Large-scale field from ER-2 data merged with geostationary imagery	32
2.4 Model calculations	33
2.5 Relationship between cloud spatial structure, net horizontal photon transport, and its spectral dependence	35
2.6 Physical mechanism and parameterization	39
2.7 Scale dependence and spatial aggregation	46
2.8 Significance for cloud radiative effect	50
2.9 Summary and conclusions	54

Chapter 3 Quantifying the spectral signature of heterogeneous clouds in

shortwave radiation measurements.....	59
3.1 Introduction.....	59
3.2 Data	63
3.3 Model calculations	70
3.4 Spectral signature of 3D cloud effects in radiance observations.....	72
3.5 Spectral signature of 3D cloud effects in irradiance observations	77
3.6 Connecting the spectral signature of 3D cloud effects in radiances and irradiances	79
3.7 Radiation closure in transmitted irradiances	82
3.8 Summary and conclusions	85
3.A Approximating the remote sensing bias.....	89
3.B Supplementary results from case 2	92
3.B.1 Spectral signature of 3D cloud effects in radiances and irradiances	92

3.B.2 Connecting the spectral signature of 3D cloud effects in radiances and irradiances	95
3.B.3 Radiation closure in transmitted irradiances.....	96
Chapter 4 Net horizontal photon transport: dependence on scene parameters and applications in airborne and ground-based cloud radiation measurements..	99
4.1 Physical and optical parameters that modulate net horizontal photon transport and its spectral dependence: modeling analysis	99
4.2 Extracting layer absorption from aircraft vertical flux divergence measurements	110
4.3 Incorporating spectral information to the estimate of 1D bias in surface transmittance below heterogeneous clouds.....	119
Chapter 5 Summary	124
Bibliography	130

Figures

- Figure 1.1: Percentage differences in the response function with respect to the first field calibration, obtained on August 11, 2013, at two SSFR channels, 550 (blue) and 1640 nm (red), of the nadir spectrometer deployed on the ER-2 during SEAC⁴RS. 11
- Figure 1.2: The cosine response as a function of μ , the cosine of incidence angle, of the light collector mounted in the nadir position of the ER-2 at two SSFR channels, 550 (blue) and 1640 nm (red). 12
- Figure 1.3: Clear sky absorptance spectra (absorption normalized by incident radiation) for the atmospheric layer between 0 and 37 km, calculated by the SSFR-specific 1D radiative transfer model (black) and the MCARaTS model in 1D mode (red). 16
- Figure 1.4: The eMAS RGB imagery of the geographical area between -90.2° and -93.4° longitude and between 33.3° and 33.5° latitude. It was taken from 1558 to 1621 UTC on August 23, 2013, over southern Arkansas during SEAC⁴RS. 17
- Figure 1.5: MODIS 16-day climatology of surface albedo spectrum (the MCD43C3 product) over the area of the 20130823 cloud case. The light and deep blue spectra were directly extracted from the MCD43C3 data, and the black spectrum was the mean over the geographical area. The orange spectrum was obtained by interpolating a MODIS spectrum to match the spectral reflectance of “dry grass” obtained from the ASTER spectral library, whereas the red spectrum was obtained

by interpolating a MODIS spectrum to match the spectral reflectance of “deciduous trees.”	18
Figure 1.6: The 20-km albedo and 2-km transmittance along the nadir track of the 20130816 SEAC ⁴ RS cloud case calculated from two 3D radiative transfer experiments using the Mie phase function and HG phase function. The dashed orange line denotes the cloud optical thickness averaged over the eMAS swath along the nadir track.	20
Figure 2.1: Cloud optical thickness from MAS along an ER-2 leg from July 17, 2007 (length: 192 km, swath: 17.5 km), re-gridded to a horizontal resolution of 500 m. The red dashed line indicates the ER-2 flight track in the center of the MAS swath. Results for the eight highlighted pixels are shown in Table 2.1 and Figure 2.3a.	31
Figure 2.2: Optical thickness of the large-scale cloud field. The green rectangle marks the embedded MAS swath (Figure 2.1); the red squares mark 20 km “super-pixels” within the scene. Radiative transfer model output outside the dashed green square is discarded (see §2.7).	32
Figure 2.3: (a) The H_λ spectra of pixels {5,6,7,8} from Figure 2.1 and Table 2.1 with (•) and without (*) molecular scattering in the 3D calculations, as well as a fit based on Eq. (2.12) from §2.6 (dashed lines). (b) Spectral slope (S_0) vs. net horizontal photon transport (H_0) from (a) (both at 500 nm) for all the pixels from Figure 2.1. Only 3D calculations with molecular scattering (black dots) show the systematic correlation between H_0 and S_0 . Disabling molecular scattering (gray dots) incorrectly predicts a spectrally neutral (flat) H_λ ($S_0 \approx 0$ for all pixels). By definition, 1D calculations	

(IPA, red dots) do not reproduce net horizontal photon transport at all ($H_0=0$ for all pixels). 37

Figure 2.4: Profiles of (a) downwelling, (b) net, and (c) upwelling irradiance at 1000 nm for cloud field from Figure 2.1. The location of the cloud layer is marked in gray. Both IPA (dashed line, hollow symbols) and 3D calculations (solid line, full symbols) are shown, averaged over the full domain (black), over all columns with $\tau < 1$ (blue) and over columns with $\tau > 120$ (red). 39

Figure 2.5: Conceptual visualization of the mechanism of horizontal photon transport. 41

Figure 2.6: (a) An example of the linear regression between $\log(\delta\lambda)/H_\infty$ versus $\log(\lambda/\lambda_0)$, from which the values of x and ε can be derived. (b) The scatter plot of x versus ε for all pixels, joint PDFs $p(x,\varepsilon)$ (contours) as well as the marginal PDFs $p(x)$ and $p(\varepsilon)$ (histograms). The peak of $p(x,\varepsilon)$, and thus the most likely $\{x,\varepsilon\}$ values for the cloud field, is located at $\{3.85, 0.065\}$, and the domain-averaged values are $\{3.91, 0.070\}$ 44

Figure 2.7: PDF of ε for all pixels with $\Delta(\varepsilon) < 5\%$, median (purple dashed line), and domain-wide effective ε derived from regression of S_0 vs. H_0 (blue dashed line). 45

Figure 2.8: Scatter plot of S_0 versus H_∞ as obtained from linear regression of Eq. (2.12) for (a) the small domain from Figure 2.1 and (b) the large-scale domain from Figure 2.2, spatially aggregated to different scales, including the 20-km “super pixels” as highlighted in Figure 2.2 (red squares). The dashed lines indicate the range for 15 km pixels. (c) Spatial distribution of S_0 from (b). Red (blue) indicates net photon “donor” (“recipient”) pixels, and green “neutral zones” ($H_\lambda \approx S_0 \approx 0$). (d) Dependence of

$\max(H)$ and $\min(H)$ on spatial aggregation scale (km). The color is the same as in (b)..... 47

Figure 2.9: (a) Transmittance biases (IPA-3D transmittance) for the eight super-pixels from Figure 2.2. (b) Correlation between net horizontal photon transport from Figure 2.8b and transmittance bias for multiple spatial aggregation scales. The dashed lines indicate the range of variability for 20 km super-pixel size. (c) Correlation of the *slopes* of the quantities from (b). (d) Same as (c), but for a bracket from the surface to cloud top, rather than the cloud layer only..... 51

Figure 2.10: H_0 is only weakly correlated with ΔR_0 at scales below 15 km, which means that, statistically, biases introduced by horizontal photon transport propagate primarily into transmittance, not albedo. This changes for larger scales..... 52

Figure 3.1: Visualization of the three science questions (SQ). The cloud distribution in a given scene (blue) translates into a reflected radiance field, which is measured by eMAS (orange) and mapped to an optical thickness field on the basis of 1D radiative transfer calculations (1D retrieval). The *remote sensing bias* ($\Delta\tau_1$) is the difference between retrieved and true cloud optical thickness. For SQ1, the retrieved cloud field is used in lieu of the unknown truth to calculate the associated radiance field with and without consideration of 3D effects (green). The modeled radiance field is then compared to the measurements, and the spectral radiance perturbations caused by 3D effects are linked to those in the associated irradiance fields (SQ2). For SQ3, the modeled irradiance field is validated with measurements by SSFR (orange) below the cloud field. The bias can be partitioned into the difference between 3D and 1D calculations (*irradiance bias*) and the *remote sensing*

bias ($\Delta\tau_1$) that propagates into both 3D and 1D irradiances calculations. The impact of $\Delta\tau_1$ on the calculated irradiance can be estimated through $\Delta\tau_2$, the difference between the original eMAS retrieval and τ_{model} (retrieved from the 3D-modeled radiance field in the same way as τ_{eMAS} was obtained from the observed radiance field). 63

Figure 3.2: eMAS-retrieved cloud optical thickness fields for the four SEAC⁴RS cloud cases listed in Table 3.1. Note that the color bar varies from case to case. 66

Figure 3.3: (a) eMAS-measured reflectance field at 470 nm (\mathfrak{R}_0) for case 1 (2013/08/16); the four pixels marked by triangles and numerical labels are placed in a shadow zone (1), on a cloudy pixel of cell #1 and #2 (2 and 3) and on a clear-sky pixel with enhanced reflectance (4); (b) Comparison of the measured (black), 1D- (red) and 3D-modeled (blue) reflectance along the dashed line in (a), plotted together with the eMAS-retrieved cloud optical thickness. The arrow “sunlit” marks a zone with enhanced reflectance. 73

Figure 3.4: eMAS (black stars), 1D- (red diamonds) and 3D-modeled (blue dots) reflectance spectra (\mathfrak{R}_λ) as well as the linear regressions for the four pixels marked in Figure 3.3a. 74

Figure 3.5: (a) The scattered plot of the measurement-derived (black), 1D- (red) and 3D-modeled (blue) reflectance at 470 nm (\mathfrak{R}_0) against spectral dependence (ζ_0) of reflectance for nadir pixels of case 1 (2013/08/16). The four pixels marked in Figure 3.2a are represented by their 3D-modeled \mathfrak{R}_0 - ζ_0 pairs. (b) Measurement-derived \mathfrak{R}_0 - ζ_0 relationships for all cases (nadir observations only). 76

- Figure 3.6: (a) Measurement-derived (black) and 3D-modeled (blue) H_0-S_0 relationships for nadir pixels of case 1. (b) Measurement-derived H_0-S_0 relationships for the three cases with collocated SSFR observations. 78
- Figure 3.7: (a) 3D-modeled $\mathfrak{R}_0-\zeta_0$ relationships for all pixels of case 1; (b) 3D-modeled H_0-S_0 relationships for pixels of the same colors in (a); (c) 3D-modeled $\mathfrak{R}_0-\zeta_0$ relationship for low reflectance pixels ($\mathfrak{R}_0 < \sim 0.2$); (d) Histograms of H_0 for pixels of the same colors in (c). The mean H_0 of the distributions from top-left to bottom-right are +17.1%, +13.1%, +0.43%, -0.91%, -18.4%, and -22.7%. 80
- Figure 3.8: (a) 3D-modeled transmitted irradiance of case 1 at 470 nm ($F^{\downarrow,470nm}$) at the DC-8 altitude, over-plotted with the SSFR-measured $F^{\downarrow,470nm}$ along the DC-8 flight track using the same color code; (b) Comparison of the measured (black) and 1D- (red) and 3D-modeled (blue) $F^{\downarrow,470nm}$ along the flight track. 83
- Figure 3.9: Measured (black line), 1D- (red dots) and 3D-modeled (blue dots) downward irradiance spectra ($\overline{F^{\downarrow}_\lambda}$) averaged over (a) clear sky pixels around cell #1; (b) cloudy pixels below cell #1; (c) clear sky pixels around cell #2; and (d) cloudy pixels below cell #2. 84
- Figure 3.10: Probability distribution functions of (a) the retrieval bias in cloud optical thickness ($\Delta\tau_2$) due to remote sensing bias of 3D cloud effects; and (b) corresponding bias in cloud transmittance at 470 nm (ΔT_{470nm}) due to $\Delta\tau_2$; for pixels along the DC-8 flight track below cell #1 shown in Figure 3.8. The means in both quantities are indicated by the blue line. 91

Figure 3.11: (a) The eMAS reflectance field at 470 nm (\mathfrak{R}_0) of case 2; (b) Comparison of the measured (black) and 1D- (red) and 3D-modeled (blue) \mathfrak{R}_0 along the nadir track, plotted together with the eMAS-retrieved cloud optical thickness; (c) The scatterplot of the measurement-derived (black stars), 1D- (red diamonds) and 3D-modeled (blue dots) \mathfrak{R}_0 against ζ_0 for nadir pixels; (d) The scatterplot of the measurement-derived (black stars) and 3D-modeled (blue dots) H_0 against S_0 for nadir pixels. 93

Figure 3.12: (a) 3D-modeled \mathfrak{R}_0 - ζ_0 relationships for all pixels of case 2; (b) 3D-modeled H_0 - S_0 relationships for pixels of the same colors in (a); (c) 3D-modeled \mathfrak{R}_0 - ζ_0 relationship for low reflectance pixels ($\mathfrak{R}_0 < \sim 0.2$); (d) Histograms of H_0 for pixels of the same colors in (c). 95

Figure 3.13: (a) 3D-modeled downward irradiance of case 2 at 470 nm ($F^{\downarrow,470nm}$) below clouds at the DC-8 altitude, over-plotted with SSFR-measured downward irradiances along the flight track using the same color code; (b) Comparison of the measured (black) and 1D- (red) and 3D-modeled (blue) $F^{\downarrow,470nm}$ along the flight track; (c) Measured (black line), 1D- (red dots) and 3D-modeled (blue dots) downward irradiance spectra ($\overline{F_{\lambda}^{\downarrow}}$) averaged over clear sky pixels; (d) same as (c) but for cloudy pixels. 97

Figure 4.1: A single isolated cloud (optical thickness 25) surrounded by clear sky. 100

Figure 4.2: Vertical profiles of 3D-modeled net irradiance at 500 nm for the P1_tau25 experiment. The gray shaded area marks the location of the cloud layer. The dashed lines mark the vertical bracket of calculating H_0 . 3D calculations are

averaged over all cloudy columns (red) and clear sky columns within 3-km of the cloud (blue)..... 103

Figure 4.3: (a) Cross-sections of H_0 along the x - z plane at $y=30$ km in the model domain (Figure 4.1) for the P3 experiments. The gray shaded area denotes cloudy regions. The blue shaded area denotes clear sky regions that are 3-km near clouds. (b) same as (a) but for S_0 104

Figure 4.4: Scatterplot of S_0 versus H_0 for the experiments P1-P4..... 105

Figure 4.5: Vertical profiles of 3D-modeled net irradiance at 1000 nm for the P4 experiments. The gray shaded area marks the location of the cloud layer. The dashed lines mark the vertical bracket for calculating H , which brackets the layer from the bottom of the cloud to 1-km above. 3D calculations are averaged over all cloudy columns (red) and clear sky columns 3-km near the cloud (blue). 109

Figure 4.6: (a) Correlation between $H_{1600\text{nm}}$ and $H_{1000\text{nm}}$ calculated from the 8-13 km bracket. The red dashed line denotes the linear regression between the two variables. The yellow dashed lines denote x-axis and y-axis. (b) Correlation between the retrieved cloud absorption $A'_{1600\text{nm}}$ and $A_{1600\text{nm}}$ within the atmospheric layer of 8-13 km. The blue dashed line denotes the 1:1 relationship. (c) Same as (a) but for the 8-20 km bracket. (d) Same as (b) but for the 8-20 km layer. (e) Same as (a) but for the 2-20 km bracket. (f) Same as (b) but for the 2-20 km bracket. All quantities were normalized by the incident solar radiation at 20 km. 113

Figure 4.7: The scatterplot of $V_{600\text{nm}}$ and $A_{600\text{nm}}$ calculated from the vertical bracket of 3-6 km..... 117

Figure 4.8: (a) Scatterplot of ΔT_{470nm} [calculated from Eq. (4.7)] against $T_{470nm}^{residual}$ [calculated from Eq. (4.8)] for all cloudy (black), optically thin (blue, $\tau < 2$), and optically thick (red, $\tau > 50$) columns of the 20130816 SEAC⁴RS cloud case. (b) Probability distributions of ΔT_{470nm} within five $T_{470nm}^{residual}$ ranges for both low (solid lines) and high (dashed lines) cloud optical thickness columns. The mean of each distribution is listed in Table 4.3..... 122

Tables

Table 1.1: Summary of the field data used for this thesis study.	7
Table 1.2: Cloud cases studied in this thesis work.	8
Table 2.1: Cloud optical thickness τ , effective radius r_e , and values of H_0 and S_0 for the eight pixels highlighted in Figure 2.1 (sorted by H_0). For pixels 5, 6, 7, 8, Figure 2.3a shows the spectral shape of H_λ	35
Table 3.1: Descriptions of the SEAC ⁴ RS cloud cases.	64
Table 3.2: Data obtained during SEAC ⁴ RS, with instruments and platforms (boldface)....	67
Table 4.1: Details for experiments P1-P4 as discussed in §4.1, labeled by main variable under consideration.	101
Table 4.2: Range of H_0 and S_0 , as well as the effective ε calculated from the H_0 – S_0 relationships shown in Figure 4.4.	106
Table 4.3: Retrieved heterogeneity and the mean of probability distribution, calculated from ΔT_{470nm} within five $T_{470nm}^{residual}$ ranges for both optically low (solid lines in Figure 4.8) and high (dashed lines in Figure 4.8) cloudy columns.	122

Chapter 1

Introduction

1.1 Motivation

Cloud radiative effects remain the most significant source of uncertainty in estimates and interpretations of the Earth's changing energy budget [Randall *et al.*, 2007]. Deriving consistent radiative energy budget quantities, such as top-of-atmosphere (TOA) and surface flux densities, as well as atmospheric absorption, is challenging, especially in the shortwave (solar) spectral range [Charlock *et al.*, 2006; Kato *et al.*, 2013]. One of the main reasons is that, mostly out of necessity, current cloud radiation studies largely neglect a key phenomenon in the three-dimensional (3D) radiative transfer in cloudy atmospheres, namely, the net horizontal photon transport (H) that results from the inhomogeneous structure of clouds (i.e., 3D cloud effects). Ramifications of neglecting 3D cloud effects can be seen in both cloud remote sensing (radiance) and radiative energy budget (irradiance) applications.

Reflected radiance fields above heterogeneous clouds, measured by passive remote sensing instruments from space and aircraft, are affected by 3D cloud effects in the form of radiative smoothing and roughening. Over some spatial scales, the radiance field of a cloud

scene is smoother than that predicted by a one-dimensional (1D) radiative transfer model, due to lateral radiation exchange between pixels [Marshak *et al.*, 1995]. Radiative roughening can also occur when side illumination and shadowing effects are pronounced under low Sun conditions [Zuidema and Evans, 1998; Oreopoulos *et al.*, 2000]. Most algorithms for retrieving cloud properties from passive imagery are performed within the 1D framework, which considers the reflected radiance from a given pixel as independent of its surroundings (i.e., independent pixel approximation or IPA). As a result, the retrieved cloud fields may be biased with respect to the truth [Chambers *et al.*, 1997; Loeb and Coakley, 1998; Zinner and Mayer, 2006; Zhang *et al.*, 2010]. For the purposes of this thesis work, we refer to this phenomenon as the remote sensing bias of 3D cloud effects. Some studies have proposed quantitative 3D corrections to retrieval algorithms [e.g., Faure *et al.*, 2001; Iwabuchi and Hayasaka, 2003]. However, most of these studies were limited to model-constructed rather than realistic clouds.

Not accounting for 3D cloud effects is also problematic for radiative energy budget applications, perhaps even more so than for remote sensing, especially in regard to deriving surface energy budget estimates from space [Ham *et al.*, 2014]. The first source of error comes from the remote sensing bias that is inherent in the cloud retrievals, and can propagate into model calculations of radiative budget quantities such as irradiances. In addition, errors arise when H is neglected in radiative budget studies using a 1D radiative transfer model, since performing full 3D radiative transfer calculations remains unaffordable for operational purposes [Davis and Marshak, 2010]. Hereafter, we refer to the second type of error as the irradiance bias of 3D cloud effects.

The root of this problem lies in the non-local nature of horizontal photon transport, which needs to be understood not only at the pixel level but also for a cloud scene in

general. Existing methods cannot isolate 3D cloud signals from shortwave radiation fields for a cloud scene as a whole because our knowledge of 3D cloud effects heretofore could not be easily parameterized or generalized to the entire pixel population of the cloud field. For example, previous studies of 3D cloud effects in radiance observations focused on the reflectance enhancement in the clear-sky regions in the vicinity of clouds [Wen *et al.*, 2007; Marshak *et al.*, 2008; Wen *et al.*, 2008; Várnai and Marshak, 2009]. They found that the magnitude of reflectance enhancement cannot simply be correlated with scene parameters such as the distance to the nearest clouds (e.g., Figure 7 in [Wen *et al.*, 2007]) or the optical thickness of the surrounding clouds (e.g., Figure 6 in [Marshak *et al.*, 2008]).

Recently, cloud-radiation studies began to investigate the *spectral* characteristics of cloud radiation fields. For example, most above-cited studies of 3D cloud effects in radiance observations found that 3D cloud effects are *spectrally dependent* in the near-ultraviolet and visible spectral range. This finding coincides with recent discoveries made from the contiguous full-spectrum cloud irradiance observations in the shortwave by airborne spectrometers [Pilewskie *et al.*, 2003; Schmidt and Pilewskie, 2012]. Schmidt *et al.* [2010b] and Kindel *et al.* [2011] discussed H using information from aircraft vertical flux divergence (see definition in §1.2) measurements for an anvil outflow (ice phase) and marine stratus layer (liquid water phase). Although based on two distinct cloud scenes, both studies reported that H is *spectrally dependent* in the near-ultraviolet and visible spectral range under inhomogeneous cloud conditions. Motivated by these studies, this dissertation pursued the overarching question whether the observed spectral dependence might carry information about the spatial inhomogeneity of a scene.

In this context, the following specific questions were considered: First, do heterogeneous clouds leave systematic imprints in the shortwave radiation fields that can

be understood and quantified by exploiting the full spectral information? If so, can the spectral signature of 3D cloud effects be detected from measurements of spectral radiance and irradiance and consequently serve as an additional observable for remote sensing and energy budget studies of heterogeneous clouds in the future? What are the practical implications for upcoming and planned field experiments?

The next three chapters are dedicated to discussing the series of studies that we undertook to address these questions. In Chapter 2 (i.e., [Song *et al.*, 2016a]), we study the spectral dependence of H reported by Schmidt *et al.* [2010b] over the entire cloud scene. We discuss the physical mechanism that gives rise to the spectral dependence of H , investigate the relationship between cloud spatial structure and the spectral signature of 3D cloud effects in irradiances, present a simple parameterization of the spectral signature, and explore the ramifications for radiative energy budget estimates. In Chapter 3 (i.e., [Song *et al.*, 2016b]), we use field observations as well as model calculations to examine the spectral signature of 3D cloud effects in radiances and irradiances, explore the connection between the two, and discuss the implications for deriving surface energy budget from cloud imagery. In Chapter 4, we extend the analysis of 3D cloud effects from conservative scattering wavelengths to non-conservative scattering wavelengths. We also discuss some practical applications for the spectral signature of 3D cloud effects. In Chapter 5, we summarize the knowledge that we have gained with respect to the questions posed above. The remainder of this chapter presents essential background for the thesis: §1.2 of this chapter provides the definitions of the radiometric quantities discussed in this work, §1.3 provides an overview of the relevant field experiments, instruments, and field data, and §1.4 introduces the three-dimensional radiative transfer model and input parameters.

1.2 Terms and definitions

The spectral radiance I_λ , also known as intensity, is the radiant energy flux transported through a unit area that is orthogonal to the direction of the radiation beam per unit time per unit wavelength per unit solid angle. The unit of spectral radiance is $\text{W m}^{-2} \text{nm}^{-1} \text{sr}^{-1}$. By definition, radiance is a directional quantity. Spaceborne and airborne passive remote sensing instruments, such as the Moderate-resolution Imaging Spectroradiometer (MODIS [King *et al.*, 1992]) and the MODIS Airborne Simulator (MAS [King *et al.*, 1996]), measure spectral radiances.

The spectral irradiance F_λ , also known as radiant flux density or flux, is the radiant energy flux transported through a horizontal plane per unit area per unit time per unit wavelength. The unit of spectral irradiance is $\text{W m}^{-2} \text{nm}^{-1}$. F_λ is the integral of the normal component of I_λ transported from all directions over an entire hemisphere. One can also consider I_λ to be the derivative of F_λ with respect to solid angle. The spectral irradiance is a radiative energy budget parameter and can be directly measured by airborne and ground-based radiation instruments. For example, the Solar Spectral Flux Radiometer (SSFR [Pilewskie *et al.*, 2003], introduced in §1.3.4) is an instrument that can be deployed on research aircraft to measure the spectrally resolved downward (F_λ^\downarrow) and upward (F_λ^\uparrow) irradiances in the shortwave.

Considering an atmospheric voxel, i.e., one of the sub-volumes that constitute an atmospheric layer, net horizontal photon transport H_λ is quantified by the horizontal flux divergence that represents the outward (lateral) flux transport through the side walls of the voxel. Therefore, for any cloud layer of interest, H_λ is not observable from space at the domain or pixel level. Airborne cloud-radiation instruments such as SSFR cannot provide direct measurements of H_λ because it is very difficult, if not impossible, to simultaneously

sample the horizontally transported flux through all sides of the cloud. However, H_λ can be derived from vertical flux divergence measurements by two collocated aircraft. The vertical flux divergence V_λ is the difference between net irradiances above and below the cloud layer:

$$V_\lambda = F_{\lambda,top}^{net} - F_{\lambda,bot}^{net} = (F_{\lambda,top}^\downarrow - F_{\lambda,top}^\uparrow) - (F_{\lambda,bot}^\downarrow - F_{\lambda,bot}^\uparrow) \quad (1.1)$$

where the net irradiance is the difference between downward and upward irradiances. In airborne cloud-radiation observations, V_λ is also referred to as the ‘‘apparent’’ absorption of a cloud layer because it differs from its ‘‘true’’ counterpart (A_λ) by the amount of horizontal flux divergence¹:

$$V_\lambda = A_\lambda + H_\lambda. \quad (1.2)$$

At conservative scattering wavelengths where A_λ vanishes, aircraft measurements of V_λ can be used to obtain H_λ . Unless otherwise noted, for the analysis presented in this thesis, H_λ , V_λ , and A_λ are normalized with respect to the incident irradiance from the top ($F_{\lambda,top}^\downarrow$). This is done in order to remove the spectral dependence in $F_{\lambda,top}^\downarrow$.

1.3 Field experiments, instruments, and data

In this section, we introduce the two field missions that are relevant to this work: the Tropical Composition, Cloud and Climate Coupling Experiment (TC⁴ [Toon *et al.*, 2010]) and the Studies of Emissions and Atmospheric Composition, Clouds and Climate Coupling

¹ Note the sign convention for H : The flux divergence Δ comprises a vertical and a horizontal term: $\Delta=V+H=A$, where V is the vertical flux divergence from the equation above, and A is the true absorption. For $A=0$, $V=-H$. In this thesis, we define H with opposite sign, i.e., $V=A+H$. This convention is more convenient for aircraft applications, where the measured vertical flux divergence is partitioned into true and apparent absorption (or net horizontal photon transport).

by Regional Surveys (SEAC⁴RS [Toon *et al.*, 2015]). This section gives a brief summary of the field data used throughout this thesis, along with the corresponding instruments (Table 1.1). Table 1.2 provides an overview of the studied cloud cases.

Table 1.1: Summary of the field data used for this thesis study.

Field mission	Instrument	Data Used
TC ⁴	Solar Spectral Flux Radiometer (SSFR [Pilewskie <i>et al.</i> , 2003])	Spectral solar irradiance
	MODIS Airborne Simulator (MAS [King <i>et al.</i> , 1996; King <i>et al.</i> , 2010])	Spectral radiance and cloud retrievals (optical thickness, effective radius, thermodynamic phase, and cloud top height)
	Cloud Radar System (CRS [Li <i>et al.</i> , 2004])	Reflectivity vertical profiles (§2.3.2)
	Geostationary Operational Environmental Satellite West (GOES-11) [Walther and Heidinger, 2012]	Large-scale cloud optical thickness field (§2.3.2)
SEAC ⁴ RS	Solar Spectral Flux Radiometer (SSFR [Pilewskie <i>et al.</i> , 2003])	Spectral solar irradiance
	Enhanced MODIS Airborne Simulator (eMAS [King <i>et al.</i> , 1996; Meyer <i>et al.</i> , 2016])	Spectral radiance and cloud retrievals (optical thickness, effective radius, thermodynamic phase, and cloud top height)
	NASA Langley Airborne Differential Absorption Lidar – High Spectral Resolution Lidar (DIAL–HSRL [Hair <i>et al.</i> , 2008])	Vertical position of cloud and aerosol layers (§3.2)
	Spectrometer for Sky-Scanning, and Sun-Tracking Atmospheric Research (4STAR [Dunagan <i>et al.</i> , 2013])	Spectral aerosol optical thickness (§3.3)
	In-Situ Measurements of Aerosol Optical Properties (AOP [Brock <i>et al.</i> , 2011])	Aerosol asymmetry parameter (§3.3)
	In-situ optical aerosol measurements by The NASA Langley Aerosol Research Group (LARGE [Schafer <i>et al.</i> , 2014])	Aerosol single scattering albedo (§3.3)
	MODIS Albedo product (MCD43C3 ² , [Schaaf <i>et al.</i> , 2002; 2011])	Spectral land surface albedo (§1.4.2)

² Land Processes Distributed Active Archive Center (LP DAAC), 2013, MODIS Albedo 16-Day Level 3 Global 0.05 Degree Climate Modeling Grid (MCD43C3). Version 5. NASA EOSDIS Land Processes DAAC, USGS Earth Resources Observation and Science (EROS) Center, Sioux Falls, South Dakota (<https://lpdaac.usgs.gov>), accessed October 1, 2013, at <http://e4ftl01.cr.usgs.gov/MOTA/MCD43C3.005/>.

Table 1.2: Cloud cases studied in this thesis work.

Field mission	Cases	Cloud type	Cloud phase	Cloud top height	Surface type
TC ⁴	20070717	Anvil outflow	Ice	~13 km	Ocean
SEAC ⁴ RS	20130816	Convective cells	Liquid	Isolated cell at ~7 km	Bare Soil
	20130823	Scattered boundary layer	Liquid	~2 km	Forest and scattered farmland
	20130913	Anvil outflow	Ice	~13 km	Ocean
	20130916	Scattered boundary layer	Liquid	~0.5-2 km	Ocean

1.3.1 Tropical Composition, Cloud and Climate Coupling Experiment (TC⁴, 2007)

The TC⁴ field mission, based in Costa Rica and Panama during July and August 2007, provided the first opportunity to obtain spectrally resolved aircraft vertical flux divergence measurements for extended periods of time. During TC⁴, the SSFR was deployed on both the NASA ER-2 and NASA/University of North Dakota DC-8 aircraft. For a number of flight legs (of approximately half an hour duration each), the ER-2 flew at its nominal altitude of 20 km, and the DC-8 flew below or within cloud layers in close coordination with the ER-2. The collocated SSFR spectral irradiance measurements led to the finding that H is spectrally dependent in the near-ultraviolet and visible spectral range under inhomogeneous conditions [*Schmidt et al.*, 2010b; *Kindel et al.*, 2011]. In addition, the MODIS Airborne Simulator (MAS [*King et al.*, 1996]) was deployed on the ER-2 and provided cloud imagery. The associated irradiance field could be computed using a radiative transfer model to help interpret the SSFR measurements and examine the characteristics of H under measurement conditions with various degrees of spatial heterogeneity. For

example, *Schmidt et al.* [2010b] compared the modeled H_λ spectra with the measurements for two locations along the collocated flight track for a cloud case observed on July 17. Chapter 2 is based on the same case, but it extends the analysis to the entire pixel population of the cloud scene and thus establishes a generalized relationship between the spectral dependence of H and cloud spatial structure.

1.3.2 Studies of Emissions and Atmospheric Composition, Clouds and Climate Coupling by Regional Surveys (SEAC⁴RS, 2013)

The SEAC⁴RS field mission was conducted near Houston, Texas, in August and September of 2013. Similar to TC⁴, two identical SSFR systems were deployed on the NASA ER-2 and DC-8 aircraft. Vertical flux divergence data were collected by the SSFR systems during a number of ER-2/DC-8 collocated flight legs, which covered a wide range of measurement conditions that were lacking in the TC⁴ dataset in terms of cloud types, cloud spatial distributions, surface types, and aerosols. In addition, the quantity and quality of the SSFR data were improved due to the installation of a stabilizing platform to the SSFR system in the zenith position of the ER-2 (introduced in §1.3.5).

The Enhanced MODIS Airborne Simulator (eMAS [*Meyer et al.*, 2016]), with enhancement/modifications primarily in the thermal infrared from MAS [*King et al.*, 1996] was deployed on the ER-2 during SEAC⁴RS. The eMAS spectral radiance data provided the opportunity to explore the spectral signature of 3D cloud effects in radiance observations. In addition, the eMAS cloud imagery was used to compute the irradiance fields for interpreting the SSFR measurements. Aerosols were present for some of the cases. We included aerosols in our model calculations to maintain consistency with observations. This

was made possible by using the data of aerosol properties from a number of instruments listed in Table 1.1.

1.3.3 Solar Spectral Flux Radiometer (SSFR)

The Solar Spectral Flux Radiometer (SSFR [*Pilewskie et al.*, 2003]) measures contiguous, moderate-resolution downwelling (zenith-viewing) and upwelling (nadir-viewing) spectral irradiance from 350 to 2150 nm, encompassing more than 90% of the incident solar radiation. The zenith and nadir SSFR systems each contain two spectrometers. The visible to very near infrared (350-1000 nm) spectrometer has a spectral resolution of 8 nm as measured by the full-width-half-maximum (FWHM) with 3 nm sampling resolution. The near and shortwave infrared (1000-2200 nm) spectrometer has a spectral resolution of 12 nm with 4.5 nm sampling resolution. Data from the two spectrometers are typically joined between 900 to 940 nm. The zenith and nadir spectrometers are connected through a fiber optic to a light collector with a hemispherical field-of-view mounted on the top and bottom of the aircraft, respectively. The SSFR records one nadir and one zenith spectrum every second.

Pre- and post-campaign laboratory calibrations as well as field calibrations of the SSFR systems are conducted jointly by the Atmospheric Radiation Group at University of Colorado Boulder and the NASA Ames Atmospheric Physics Radiation Laboratory at the NASA Ames Airborne Sensor Facility. Before and after each field mission, the spectrometers are radiometrically calibrated in the laboratory with a NIST-traceable blackbody (tungsten-halogen 1000W FEL lamp). This provides the primary calibration, from which response functions are obtained for translating raw counts measured by the spectrometers (in voltage per unit integration time) to the physical unit of $\text{W m}^{-2} \text{nm}^{-1}$. The

uncertainty of the calibration light source dominates the nominal 3% radiometric accuracy of the SSFR. The primary calibration is then transferred to a portable field radiometric calibration system, which is used to conduct regular field calibrations. By tracing changes in the response functions, one can monitor the stability of the spectrometers during a field mission.

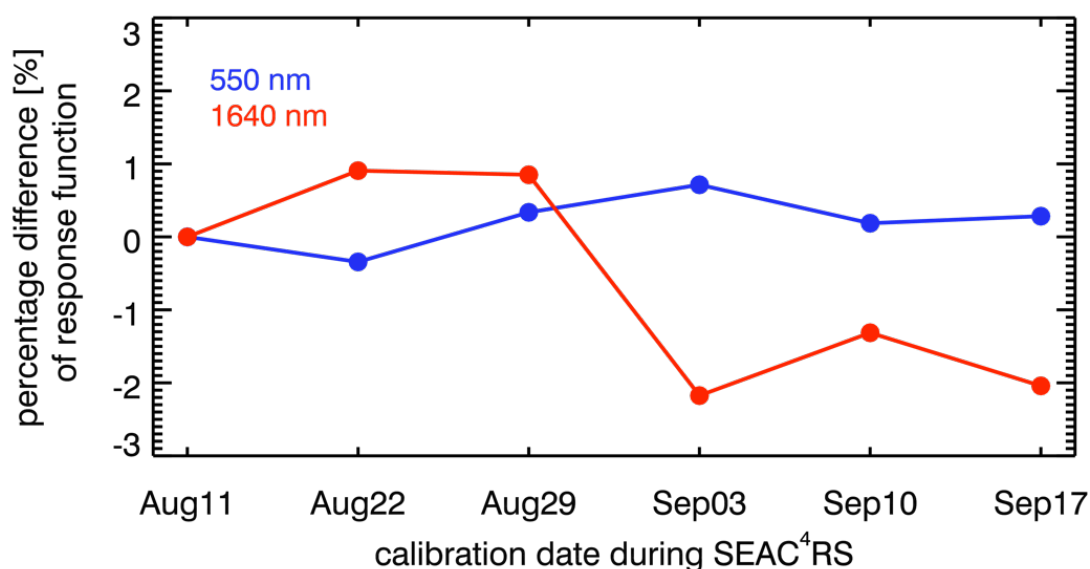


Figure 1.1: Percentage differences in the response function with respect to the first field calibration, obtained on August 11, 2013, at two SSFR channels, 550 (blue) and 1640 nm (red), of the nadir spectrometer deployed on the ER-2 during SEAC⁴RS.

As an example, Figure 1.1 illustrates the stability of the nadir SSFR spectrometers deployed on the ER-2 during SEAC⁴RS. The first field calibration was taken on August 11 after the ER-2 SSFR system was integrated. The last one was taken close to the end of the mission on September 17. For every calibration, the response function was compared against the August 11 calibration as a percentage difference at all SSFR wavelengths. Figure 1.1 shows the results at 550 and 1640 nm, which represent the general

performance of the visible to very near infrared spectrometer and the near and shortwave infrared spectrometer, respectively. In general, over the course of a multiple-week field mission such as SEAC⁴RS, the flight-to-flight calibration stability of the SSFR is better than 3%.

1.3.4 SSFR data processing

To properly measure irradiances, the incident radiation measured by a light collector must be weighted by the cosine of incidence angle (μ) with respect to the light collector reference plane. The cosine response, also referred to as the angular response, of all light collectors as a function μ is characterized before each deployment. It is used later to apply so-called cosine-corrections to field data when the response deviates from μ .

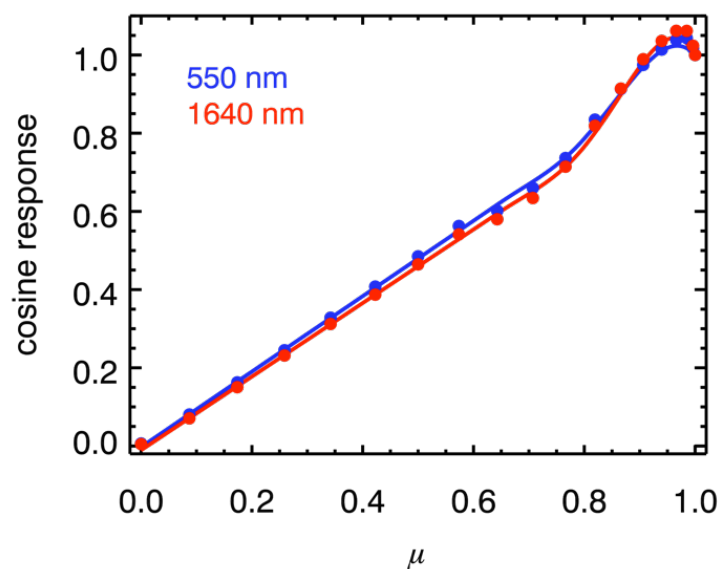


Figure 1.2: The cosine response as a function of μ , the cosine of incidence angle, of the light collector mounted in the nadir position of the ER-2 at two SSFR channels, 550 (blue) and 1640 nm (red).

Figure 1.2 shows the cosine response for one of the light collectors used during SEAC⁴RS. Measurements (dots) were taken at 19 incidence angles from 0° to 90° at a resolution of 5° and normalized by those of the normal incidence ($\mu = 1$). Then an interpolation was performed to obtain the cosine response at other incidence angles (lines). For μ smaller than 0.8 (i.e., incidence angle greater than 37°), the cosine response was linear, and a linear interpolation was used. Around 0.95 (18°), there was a so-called hotspot where the dependence of the cosine response as a function of μ was slightly higher than μ . For $\mu > 0.8$, an interpolation was performed by fitting a fourth-degree polynomial to the measurements. In addition, as shown in Figure 1.2, the cosine response varied slightly with respect to wavelength and was thus characterized for all SSFR channels.

Irradiance data collected from light collectors that are fix-mounted to aircraft need to be further corrected or filtered to address the sensor misalignment problem, i.e., the deviation of the light collector reference plane from the horizontal plane due to aircraft movements such as turns, ascents, descents, and maneuvers. For the solar zenith angles of the cloud cases studied in this thesis (18-35°), a misalignment of 3° could introduce 2-4% uncertainties to the downward irradiance [Wendisch *et al.*, 2001]. Typically, when the deviation of the aircraft attitude from the horizontal plane is less than 3°, attitude corrections are applied to the SSFR data [Schmidt *et al.*, 2010a]. Outside of these limits, data cannot be properly corrected and are discarded.

The cosine-corrected and attitude-corrected SSFR data can be used for scientific purposes. The accuracy of the SSFR is determined by uncertainties in the absolute radiometric calibration of the spectrometers, cosine response of the light collectors, and aircraft attitude during flights. According to Schmidt *et al.* [2010b], an empirical estimate of the maximum total error was 7% for the downward irradiance ($e(F^\downarrow)$) and 5% for the

upward irradiance ($e(F^\uparrow)$) for TC⁴, where e denotes systematic absolute instrument uncertainties. *Schmidt et al.* [2010b] also suggested estimating the error of the net irradiance by: $e(F^{net}) \approx |e(F^\downarrow)| + |e(F^\uparrow)|$ and the error of the vertical flux divergence by:

$$e(V) \approx \left((e(F_{top}^{net}))^2 + (e(F_{bot}^{net}))^2 \right)^{1/2}.$$

During SEAC⁴RS, a stabilizing platform, similar to the one described by *Wendisch et al.* [2001], was integrated to the SSFR system in the zenith and nadir position of the ER-2. The stabilizing platform actively compensated for changes in aircraft roll and pitch within $\pm 10^\circ$, which allowed the light collectors to remain level most of the time. As expected, the integration of the stabilizing platform reduced the attitude-related uncertainties in the irradiance data and improved the accuracy of the SSFR [*Wendisch et al.*, 2001; *Bucholtz et al.*, 2008] for a few reasons. First, it largely reduced the uncertainties in the attitude-correction routines for the downward irradiance data. Since the nadir light collector was also actively leveled, the quality of the upward irradiance data was improved. This helped retain a large quantity of valid data that would otherwise have been discarded due to sensor misalignments. For example, approximately 10% of the total data collected on August 23, 2013 would be discarded by applying the $\pm 3^\circ$ filter of the attitude deviation. When the criterion was relaxed to $\pm 10^\circ$ because of the leveling platform, 90% of these filtered data could be retained.

1.4 Three-dimensional radiative transfer model and input parameters

In this section, the three-dimensional radiative transfer model used in this work – the Monte Carlo Atmospheric Radiative Transfer Simulator (MCARaTS [*Iwabuchi*, 2006]) – and its input parameters are introduced. Two of the challenges were to obtain spectral

surface albedo and the scattering properties of clouds as input. While MCARaTS is capable of using the exact phase function, this is computationally more expensive than the Henyey-Greenstein (HG) phase function approximation [*Henyey and Greenstein, 1941*]. We therefore explore whether the HG approximation suffices for calculating the irradiance field for liquid water clouds (confirmed in §1.4.3).

1.4.1 Monte Carlo Atmospheric Radiative Transfer Simulator (MCARaTS)

The MCARaTS model simulates 3D radiative transfer in both radiance and irradiance mode in the solar wavelength range. A number of inhomogeneous elements can be prescribed in the model atmosphere, such as multi-layer heterogeneous clouds with user-prescribed phase functions, multiple aerosols, and complex surface reflectance. In addition, the model can perform 1D radiative transfer calculations with the IPA option enabled.

In order to calculate irradiances at wavelengths where gaseous absorption is not negligible, we incorporated the molecular absorption coefficients of an entire atmospheric column into the MCARaTS model. This is especially important for the study of §4.2 where we discuss the retrieval of true atmospheric layer absorption from aircraft irradiance measurements. We adopted the absorption coefficients generated by the correlated k-distribution method described by *Coddington et al. [2008]*. The absorption coefficients were computed based on the HITRAN 2004 molecular spectroscopic database [*Rothman et al., 2005*]. The calculations were performed in an SSFR-specific 1D radiative transfer model that uses DISORT (Discrete Ordinates Radiative Transfer Program [*Stamnes et al., 1988*]) as the radiative transfer solver. As a validation, we compared the clear sky absorptance spectra (absorption A_λ normalized by incident irradiance $F_{\lambda,top}^\downarrow$) computed by the SSFR-specific 1D model and the MCARaTS model in 1D mode (Figure 1.3). The calculations were

done for a purely absorbing underlying surface and the standard tropical atmosphere. The solar zenith angle was prescribed as 0° .

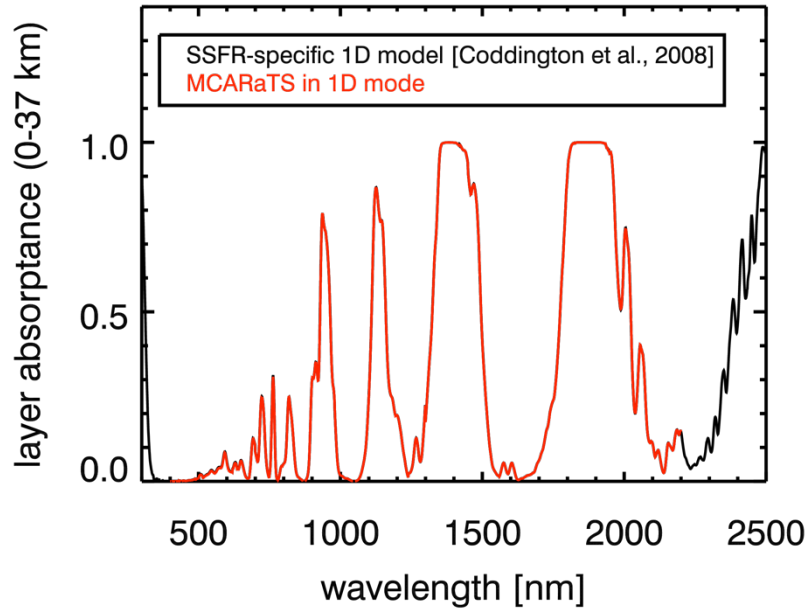


Figure 1.3: Clear sky absorptance spectra (absorption normalized by incident radiation) for the atmospheric layer between 0 and 37 km, calculated by the SSFR-specific 1D radiative transfer model (black) and the MCARaTS model in 1D mode (red).

The results show that with the same input atmospheric absorption profiles, the two models generate nearly identical layer absorptance spectra, which confirms that we introduced absorption by atmospheric constituents properly in the MCARaTS model input. Some of the major absorption features shown in Figure 1.3 include the Chappuis-band of ozone absorption between 500 and 700 nm, the Oxygen A-band around 760 nm, and the water vapor absorption bands around 940, 1140, 1400, 1900 nm.

1.4.2 Spectral surface albedo

The spectral surface albedo is a necessary input for performing radiative transfer calculations. For cloud cases observed over ocean, we used the ocean surface albedo from *Coddington et al.* [2010]. For cloud cases observed over land, we prescribed spectral surface albedo based on the MODIS Albedo product (MCD43C3 [*Schaaf et al.*, 2002; *Schaaf et al.*, 2011]), which provides the 16-day climatology of surface albedo at 5.6-kilometer spatial resolution (0.05° latitude/longitude Climate Modeling Grid). Our method was to obtain the climatology of the MODIS spectral albedo at the specific geographic locations of the observed cases and then interpolate and (or) extrapolate the albedo from MODIS channels onto wavelengths of our study.

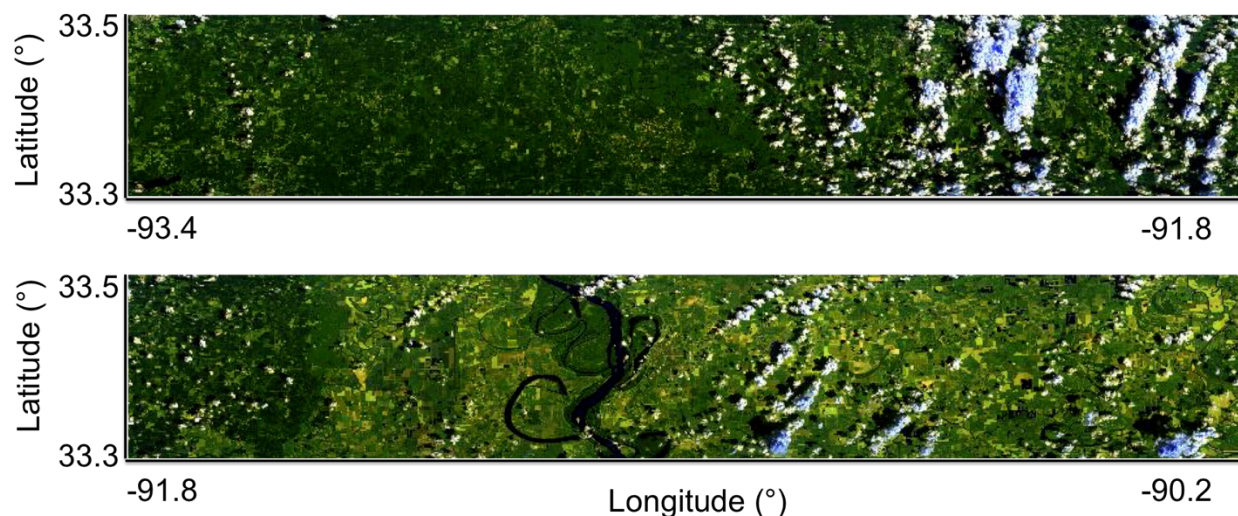


Figure 1.4: The eMAS RGB imagery of the geographical area between -90.2° and -93.4° longitude and between 33.3° and 33.5° latitude. It was taken from 1558 to 1621 UTC on August 23, 2013, over southern Arkansas during SEAC⁴RS.

However, obtaining a representative surface albedo spectrum for a geographic area over several hundred kilometers posed a challenge. This difficulty is illustrated with the

20130823 case, observed from 2004 to 2028 UTC on August 23, 2013 over southern Arkansas (between -90.03° and -93.3° longitude, and between 33.2° and 33.6° latitude). Figure 1.4 shows the eMAS RGB imagery of approximately the same geographical area that was acquired earlier that day when it was mostly cloud-free. It suggests that this area consisted of mainly forests and scattered, less vegetated farmland. Since the spatial variability of surface albedo as shown by the eMAS imagery is not fully captured by the MODIS product, we did not consider the spatial inhomogeneity of surface albedo in our model calculations. Instead, we obtained the most representative surface albedo spectrum as the input to the radiative transfer model.

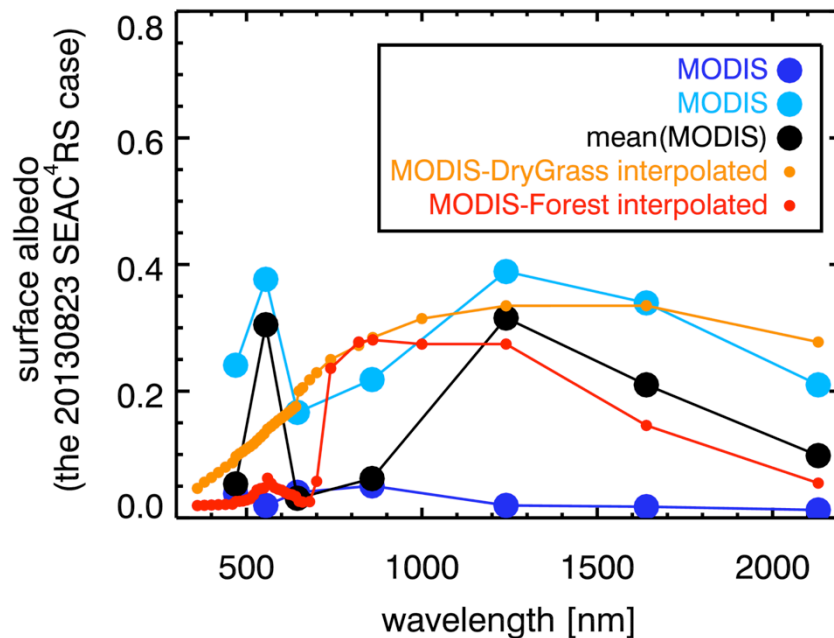


Figure 1.5: MODIS 16-day climatology of surface albedo spectrum (the MCD43C3 product) over the area of the 20130823 cloud case. The light and deep blue spectra were directly extracted from the MCD43C3 data, and the black spectrum was the mean over the geographical area. The orange spectrum was obtained by interpolating a MODIS spectrum to match the spectral reflectance of “dry grass” obtained from the ASTER spectral library, whereas the red spectrum was obtained by interpolating a MODIS spectrum to match the spectral reflectance of “deciduous trees.”

Figure 1.5 shows a few representative surface albedo spectra from the MODIS product and the mean over the domain, which confirms a large spread in the magnitude and spectral dependence over this longitude/latitude region. The light and deep blue spectra were directly extracted from the MCD43C3 data, and the black spectrum was the mathematical mean over this region. It is worth noting that the albedo at 555 nm in the light blue and black spectra is unlikely physical.

Since the MODIS surface albedo itself has a wide range, and we know that there are at least two surface types over this area, there is obviously more than one approach for interpolation and (or) extrapolation. For example, the orange spectrum in Figure 1.5 was obtained by interpolating one MODIS spectrum to mimic the spectral reflectance of dry grass obtained from the ASTER spectral library [Baldrige *et al.*, 2009]. The red spectrum was obtained by interpolating another MODIS spectrum to mimic the spectral reflectance of deciduous trees, also obtained from the ASTER spectral library. Both interpolations are realistic given the large spread in MODIS surface albedo. Since this area mainly consists of forests, we decided to use the red spectrum as the prescribed surface albedo over the entire domain. However, as evidenced in §3.4, the variability in the spectral surface albedo explains some of the spectral features in measured radiance fields that are absent from the modeled results. When performing the interpolations, we relied mostly on the reflectance spectra from the ASTER spectral library to obtain information at this wavelength (orange and red spectra).

1.4.3 Henyey-Greenstein phase function in the irradiance calculation

All radiative transfer calculations involving scattering depend on the phase function that prescribes the probability of a photon being scattered from its incident direction to an

emergent direction. For computing irradiances in liquid water cloud scenes, using an approximation such as the Henyey-Greenstein (HG) phase function is often adequate and can largely increase the computational efficiency [Liou, 2002; Zender, 2001]. The HG phase function parameterizes the full phase function using its first Legendre moment, i.e., the asymmetry parameter g .

To justify the application of the HG phase function in 3D radiative transfer irradiance calculations, we first obtained the scattering phase function and corresponding Legendre expansion coefficients (including g) for liquid water droplets from Mie scattering calculations [Wiscombe, 1980] within the libRadtran (library for radiative transfer: www.libradtran.org) package [Mayer and Kylling, 2005]. Then we used the 3D mode in the MCARaTS model to calculate the irradiance field of the 20130816 cloud scene, first with the full Mie phase function and then with the HG approximation.

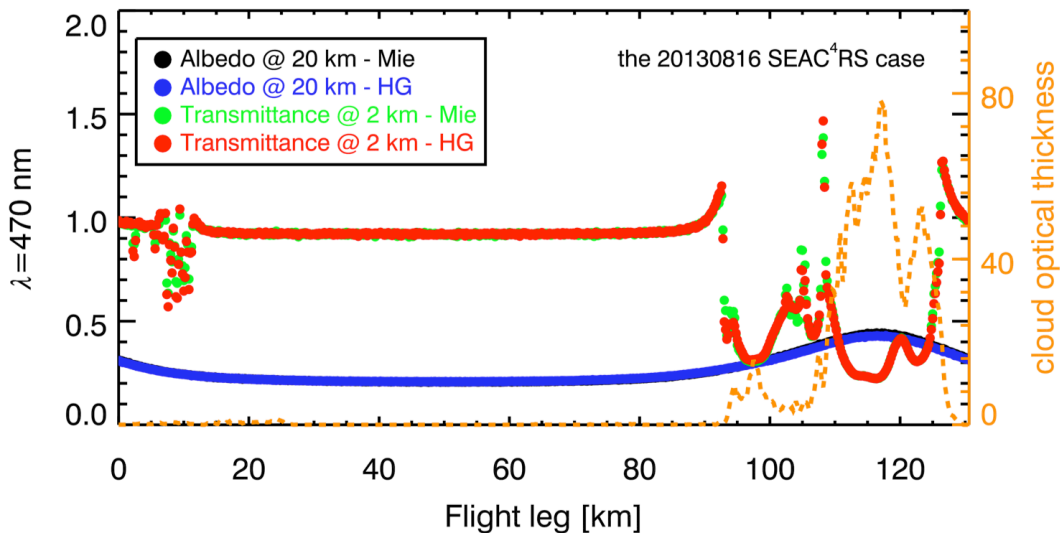


Figure 1.6: The 20-km albedo and 2-km transmittance along the nadir track of the 20130816 SEAC⁴RS cloud case calculated from two 3D radiative transfer experiments using the Mie phase function and HG phase function. The dashed orange line denotes the cloud optical thickness averaged over the eMAS swath along the nadir track.

Figure 1.6 shows that both calculations yielded nearly identical answers to the albedo at the ER-2 altitude (20 km) and the transmittance at the DC-8 altitude (2 km) along the flight track. Averaged over the entire leg, results from the HG experiment deviated from those of the Mie experiment by less than 1.5%. In this way, we justified using the HG approximation for our irradiance calculations. However, the full phase function was used for all radiance calculations.

Chapter 2

The spectral signature of cloud spatial structure in shortwave irradiance

2.1 Introduction

Determining cloud radiative effects for scenes with a high degree of spatial complexity remains one of the most persistent problems in atmospheric radiation, especially at the surface where satellite observations can only be used indirectly to infer energy budget terms. In the shortwave (solar) spectral range, it is especially challenging to derive consistent albedo, absorption, and transmittance from spaceborne, aircraft, and ground-based observations for inhomogeneous cloud conditions [*Kato et al.*, 2013; *Ham et al.*, 2014]. This problem is closely related to the long-debated discrepancy between observed and modeled cloud absorption [*Stephens et al.*, 1990] since energy conservation for a three-dimensional (3D) atmosphere [*Marshak and Davis* [2005], Eq. (12.13)]

$$R + T = 1 - (A + H) \quad (2.1)$$

connects reflectance³ R , transmittance T , and absorptance A of a layer. The term H accounts for lateral net radiative flux from pixel to pixel (which we will call net horizontal

³ albedo for reflected irradiance (flux density).

photon transport⁴). Out of necessity, most algorithms for deriving R , T , and A from passive imagery inherently presume isolated pixels by relying on one-dimensional (1D) radiative transfer (independent pixel approximation) which does not reproduce H . Net horizontal photon transport has therefore long been a common explanation not only for inconsistencies between measured and calculated broadband cloud absorption [*Fritz and MacDonald*, 1951; *Ackerman and Cox*, 1981] but also for remote sensing artifacts [*Platnick*, 2001].

Observational evidence for this explanation emerged with the availability of spectrally resolved aircraft measurements of shortwave irradiance (Solar Spectral Flux Radiometer, SSFR: [*Pilewskie et al.*, 2003]). *Schmidt et al.* [2010] derived *apparent absorption*, the sum of A and H , from irradiance measurements aboard the NASA ER-2 and DC-8 aircraft that flew along a collocated path above and below a heterogeneous anvil cloud during the Tropical Composition, Cloud and Climate Coupling Experiment (TC⁴) [*Toon et al.*, 2010]. The spectral dependence of apparent absorption as well as its pixel-to-pixel variability showed that in absolute terms, H at visible wavelengths (where cloud and gas absorption are negligible) can assume similar values as the absorbed irradiance A at near-infrared wavelengths (where $|H| \ll A$). Horizontal photon transport thus has the potential to mimic substantially enhanced absorption in broadband measurements. Three-dimensional (3D) calculations confirmed the measurements, and radiative closure was achieved within measurement and model uncertainties without invoking proposed enhanced gaseous absorption [*Arking*, 1999] or big cloud droplets [*Wiscombe et al.*, 1984]. The results also suggested that the overestimation of absorption would persist even when averaging over long distances as proposed by *Titov* [1998]. This is simply because radiation

⁴ Our use of the term “photon” is rooted in Monte Carlo radiative transfer.

flight legs are often preferentially targeted at cloudy regions ($\langle H \rangle > 0$) and do not adequately sample clear-sky areas where photons are depleted ($\langle H \rangle < 0$), which is interpreted as *apparent emission* in measurements.

Perhaps the most significant finding by *Schmidt et al.* [2010] was the distinct spectral shape of H from the near-ultraviolet well into the visible wavelength range, leading to the notion of “colored” net horizontal photon transport [*Schmidt et al.*, 2014].⁵ Strategies for mitigating the overestimation of cloud absorption [*Ackerman and Cox*, 1981; *Marshak et al.*, 1999] require that H be more or less constant in the visible wavelength range [*Welch et al.*, 1980], and so the discovery of the spectral dependence of H suggested that they should be applied with caution.⁶

Further analysis of the relationship between cloud structure and its spectral signature, presented here, revealed a surprisingly robust correlation between the *magnitude* of H and its *spectral slope*, $dH/d\lambda$. In the course of this paper, we provide evidence for molecular scattering as the physical mechanism behind this correlation and develop a simple parameterization based on this knowledge. In an accompanying paper [*Song et al.*, 2016b], we will demonstrate that cloud spatial inhomogeneities also manifest themselves in spectral *radiance* perturbations via $dH/d\lambda$, which can be used for deriving H correction terms for cloud radiative effects of inhomogeneous scenes from space-borne observations.

⁵ A previous study addressing horizontal photon transport from an energy budget point of view [*Kassianov and Kogan*, 2002] had focused on the wavelength range of 0.7-2.7 μm , specifically to avoid molecular scattering at shorter wavelengths.

⁶ For example, *Marshak et al.* [1999] in their conditional sampling technique require that $H = 0$ for at least two different wavelengths. *Kindel et al.* [2011] applied such a modified scheme for boundary layer clouds.

We complete our paper by examining at which spatial aggregation H can be ignored and whether the discovered correlation between H and $dH/d\lambda$ is scale invariant. Finally, we consider the ramifications of our findings on the shortwave surface energy budget and find that while cloud transmittance biases may be significant even after spatial averaging, they are also accompanied by spectral perturbations similar to the ones we encountered for H . These biases may thus be detectable and correctable using adequate ground-based radiometers.

Following this introduction, we provide definitions of relevant terms and explain how H relates to top-of-atmosphere (TOA) and surface cloud radiative effects (CRE). We then discuss the data and model calculations that lay the basis for our study (§2.3 and §2.4). In §2.5, we discuss the correlations between H and $dH/d\lambda$, followed by the underlying physical mechanism and parameterization presented in §2.6. The discovered relationship is then examined as a function of spatial scale (§2.7) and interpreted in terms of the surface CRE (§2.8). In the conclusions, we discuss the significance of our findings and propose multi-spectral or spectral techniques for deriving first-order correction factors in CRE estimates from space, aircraft, and from the surface that may render 3D calculations unnecessary.

2.2 Net horizontal photon transport and cloud radiative effect

The instantaneous radiative effect of any atmospheric constituent is the difference of net irradiance (flux density) in its presence (all-sky) and absence (clear-sky). For clouds, we define

$$CRE_{\lambda} = \left[\frac{(F_{\lambda}^{\downarrow} - F_{\lambda}^{\uparrow})_{all-sky}}{F_{\lambda}^{\downarrow,TOA}} - \frac{(F_{\lambda}^{\downarrow} - F_{\lambda}^{\uparrow})_{clear-sky}}{F_{\lambda}^{\downarrow,TOA}} \right] \times 100\%, \quad (2.2)$$

where F_{λ}^{\downarrow} and F_{λ}^{\uparrow} are downwelling and upwelling irradiance and their difference is net irradiance. For this paper, we normalize the *absolute* radiative effect by the TOA downwelling irradiance ($F_{\lambda}^{\downarrow,TOA}$) and consider the *relative* radiative effect as percentage of the incident irradiance. Also, we use spectrally resolved rather than broadband quantities, indicated by subscript λ .

The TOA shortwave CRE is always negative (*cooling* effect) because the reflected irradiance $F_{\lambda}^{\uparrow,TOA}$ in presence of clouds is larger than for clear-sky conditions. The surface shortwave CRE is also negative because clouds decrease the transmitted irradiance $F_{\lambda}^{\downarrow,SUR}$, at least for homogeneous conditions; broken clouds can locally increase surface insolation. In contrast to the shortwave CRE at TOA and at the surface, homogeneous clouds have a *warming* effect on the layer in which they reside. This can be quantified in terms of the layer property absorptance

$$A_{\lambda} = \left[\frac{F_{\lambda}^{\downarrow,top} - F_{\lambda}^{\uparrow,top}}{F_{\lambda}^{\downarrow,top}} - \frac{F_{\lambda}^{\downarrow,base} - F_{\lambda}^{\uparrow,base}}{F_{\lambda}^{\downarrow,top}} \right] \times 100\% \quad (2.3)$$

for a cloud located between h_{top} and h_{base} with the same normalization as used above for the relative CRE. It can be determined from aircraft measurements by collocated legs above and below the cloud [Schmidt *et al.*, 2010b]. The warming within the layer arises from absorption ($A > 0$) primarily in the near-infrared wavelength range ($1 \mu\text{m} < \lambda < 4 \mu\text{m}$). Similarly, as absorptance, layer transmittance and reflectance are defined as

$$T_\lambda = \left(\frac{F_\lambda^{\downarrow,base}}{F_\lambda^{\downarrow,top}} \right) \times 100\% \quad (2.4)$$

$$\text{and } R_\lambda = \left(\frac{F_\lambda^{\uparrow,top} - F_\lambda^{\uparrow,base}}{F_\lambda^{\downarrow,top}} \right) \times 100\%. \quad (2.5)$$

Related to layer reflectance is the albedo $\alpha_\lambda = F_\lambda^\uparrow / F_\lambda^\downarrow$ (identical to R_λ for zero surface albedo). The sum of layer absorptance, transmittance, and reflectance defined in this way is 100% and thus satisfies energy conservation for horizontally homogeneous layers. For individual pixel sub-volumes within an inhomogeneous layer (voxels), A_λ in Eq. (2.3) can be replaced with $A_\lambda + H_\lambda \equiv V_\lambda$ where V_λ stands for the vertical flux divergence (the net irradiance difference above and below a layer). In this way, energy conservation including horizontal transport [Eq. (2.1)] is retained.

The difference of the CRE at TOA and at the surface from Eq. (2.2) can be related to Eq. (2.3) as follows:

$$CRE^{TOA} - CRE^{surface} = \left[\frac{\left(F_\lambda^{net,cloud} - F_\lambda^{net,clear} \right)^{TOA}}{F_\lambda^{\downarrow,TOA}} - \frac{\left(F_\lambda^{net,cloud} - F_\lambda^{net,clear} \right)^{surface}}{F_\lambda^{\downarrow,TOA}} \right] \times 100\% \quad (2.6a)$$

$$= \left[\frac{\left(F_\lambda^{net,TOA} - F_\lambda^{net,surface} \right)^{cloud}}{F_\lambda^{\downarrow,TOA}} - \frac{\left(F_\lambda^{net,TOA} - F_\lambda^{net,surface} \right)^{clear}}{F_\lambda^{\downarrow,TOA}} \right] \times 100\% \quad (2.6b)$$

The first term inside the brackets of Eq. (2.6b) is identical to A_λ from Eq. (2.3) if the boundaries of the layer h_{top} and h_{base} are extended to the TOA and surface, respectively.

We denote this by \hat{A}_λ and distinguish full-column properties using a caret (\hat{A} , \hat{H} , \hat{R} , \hat{T}) from the layer properties that bracket only the cloud itself (A , H , R , T). The second term in

Eq. (2.6b) stems from “clear-sky” absorption by atmospheric constituents other than clouds (gases and aerosols). Eq. (2.6b) can then be re-written as

$$\hat{A}_\lambda = CRE^{TOA} - CRE^{surface} + \left[\frac{\left(F_\lambda^{net,TOA} - F_\lambda^{net,surface} \right)^{clear}}{F_\lambda^{\downarrow,TOA}} \right] \times 100\% \quad (2.6c)$$

which simply means that the total atmospheric column absorption comprises contributions from the cloud itself as well as from clear-sky absorption.⁷ In presence of horizontal inhomogeneities, the left and right side of Eq. (2.6c) may be inconsistent unless \hat{A}_λ is replaced with $\hat{V}_\lambda = \hat{A}_\lambda + \hat{H}_\lambda$ as above.

Presented in this way, the central role of absorptance and horizontal transport in linking the net irradiances above and below a cloud [Eq. (2.3)], as well as the TOA and surface CRE [Eq. (2.6c)], becomes clear. While the global TOA CRE can directly be derived from reflected radiances [Loeb *et al.*, 2005], for example from the Clouds and the Earth’s Radiant Energy System (CERES) on the Aqua and Terra satellites [Wielicki *et al.*, 1996], the derivation of the surface CRE also requires the knowledge of atmospheric absorptance or transmittance. In the case of CERES, the required cloud properties are obtained from retrievals of the accompanying imager, the Moderate Resolution Imaging Spectroradiometer (MODIS) [Minnis *et al.*, 2011]. As stated in the previous section, this is accomplished through lookup tables that are based on 1D calculations and therefore do not provide H .

⁷ The cloud contribution term $CRE^{TOA} - CRE^{surface}$ also contains multiple scattering enhancements of gas absorption due to clouds [Kindel *et al.*, 2011], which may lead to a considerable increase of the gas absorption [Schmidt and Pilewskie, 2012].

Recognizing the crucial significance of horizontal photon transport for obtaining an accurate surface CRE, *Barker et al.* [2012] and *Illingworth et al.* [2015] described the ambitious goal of using 3D radiative transport operationally in the European radiative budget experiment Earth Clouds, Aerosols and Radiation Explorer (EarthCARE). They tested their algorithm with A-Train data. As a metric for 3D effects, they employed the commonly used difference between 3D and IPA calculations (e.g., [*Scheirer and Macke*, 2003]). In a similar manner, *Ham et al.* [2014] calculated the effect of horizontal photon transport on cloud absorption, transmission, and reflected radiance. They found these three quantities to be correlated when stratifying their results by cloud type after spatial aggregation to at least 5 km.

Since the studies cited above pertained to EarthCARE and CERES, they only considered broadband effects. This does not allow distinguishing between A_λ and H_λ by means of their distinct spectral characteristics. Our approach, first presented by *Schmidt et al.* [2014], bridges this gap. In this paper, we will focus exclusively on the near-ultraviolet and visible wavelength range and explore the spectral fingerprint from cloud inhomogeneities in conjunction with molecular scattering in H_λ , which also imprints itself on reflected radiances [*Song et al.*, 2016b]. We chose not to include aerosols in either study, primarily to isolate the spectral signature of heterogeneous clouds before considering the more general case of clouds and aerosols in combination.

The spectral dependence of the horizontal photon transport across the full shortwave range will be published separately (Chapter 4). Our expectation for the future, discussed in the conclusions (§2.9), is that future energy budget studies will capitalize on the spectral fingerprint of cloud inhomogeneities and derive H by way of the associated spectral radiance perturbations.

2.3 Cloud Data

Our study builds upon the results by *Schmidt et al.* [2010b] and therefore uses the same cloud case, a tropical convective core with anvil outflow, observed during the TC⁴ experiment on July 17 2007 (from 1519 to 1535 UTC) by the NASA ER-2 aircraft about 300 km south of Panama. Two realizations of the observed cloud field were used as input to 3D radiative transfer calculations, one based on airborne imagery only (as in the earlier study, §2.3.1), and one based on merged airborne and geostationary imagery (§2.3.2) to study large-scale effects.

2.3.1 Sub-scene from ER-2 passive and active remote sensors

Level-2 cloud retrievals of the Moderate Resolution Imaging Spectrometer (MODIS) Airborne Simulator (MAS: [*King et al.*, 1996; *King et al.*, 2010]) were combined with reflectivity profiles from the Cloud Radar System (CRS: [*Li et al.*, 2004]) as described in detail by *Schmidt et al.* [2010]. The primary information originates from MAS optical thickness, thermodynamic phase, effective radius, and cloud top height retrievals for each pixel (x,y) within the imager’s swath (roughly 20 km for a cloud top height of 10 km), derived using the MODIS cloud optical properties algorithm [*Platnick et al.*, 2003] adapted to the MAS airborne imagery. The imagery-derived information was extended into the vertical dimension z by simple approximations:

- (1) The effective radius from MAS, $r_e(x,y)$, was used throughout the vertical dimension z although representative only of the topmost layer. Since the study is limited to the near-ultraviolet and visible wavelength range where cloud absorption is negligible, this simplification only affects the scattering phase function. Approximating it with

that at cloud top is acceptable because to first approximation, 3D radiative transfer is determined by the distribution of cloud extinction.

- (2) The MAS-retrieved optical thickness $\tau(x,y)$ for each pixel was vertically distributed by using the water content profile from CRS: $WC(z) = 0.137 \times Z^{0.64}$ [Liu and Illingworth, 2000], where Z is the radar reflectivity from CRS in dBZ. Since $WC(z)$ is only available along the flight track, nadir-only CRS profiles were also used across the entire MAS swath (shifted vertically by z_0 to match the MAS cloud top height at off-nadir pixels). Cloud extinction β for each voxel (x,y,z) was thus obtained as

$$\beta(x,y,z) = \tau_{MAS}(x,y) \times WC(z+z_0) / \sum_z WC(z)$$

Along the flight track, the mismatch between MAS- and CRS-retrieved cloud top height is ≤ 0.5 km. The CRS-derived average cloud top height is 10.8 km, and the mean geometrical thickness is 3.3 km.

The resulting cloud field was gridded to a resolution of 0.5 km horizontally and 1.0 km vertically (chosen larger than the mismatch between CRS and MAS in cloud top height).

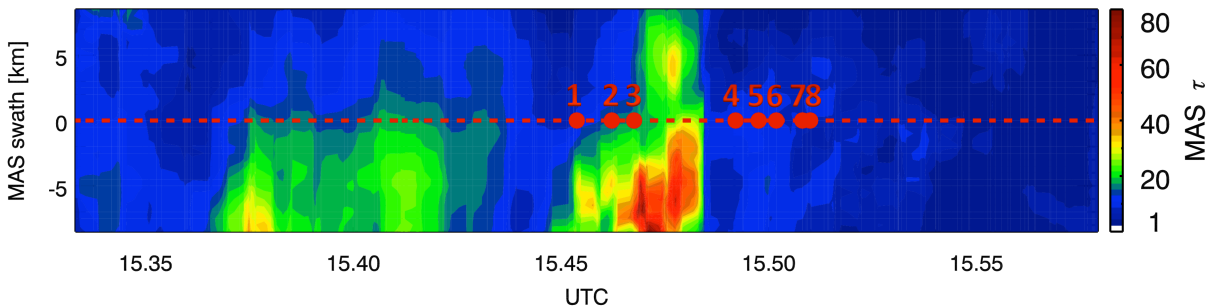


Figure 2.1: Cloud optical thickness from MAS along an ER-2 leg from July 17, 2007 (length: 192 km, swath: 17.5 km), re-gridded to a horizontal resolution of 500 m. The red dashed line indicates the ER-2 flight track in the center of the MAS swath. Results for the eight highlighted pixels are shown in Table 2.1 and Figure 2.3a.

Figure 2.1 shows the cloud optical thickness field from MAS after regridding, with the nadir track highlighted as a dashed line. The length of this scene is 192 km (384 pixels in x), and the width is 17.5 km (35 pixels in y).

2.3.2 Large-scale field from ER-2 data merged with geostationary imagery

To generalize our findings to larger scales than 17.5 km, we embedded the sub-scene from the ER-2 remote sensors in the context of the large-scale cloud field as retrieved from the Geostationary Operational Environmental Satellite West (GOES-11). The imager onboard GOES-11 has five channels centered at 0.65, 3.9, 6.7, 10.7 and 12.0 μm . In the sampling region, cloud property retrievals were produced at 1515 and 1545 UTC [Walther and Heidinger, 2012], of which we chose the earlier one because it was more consistent with the MAS retrieval.

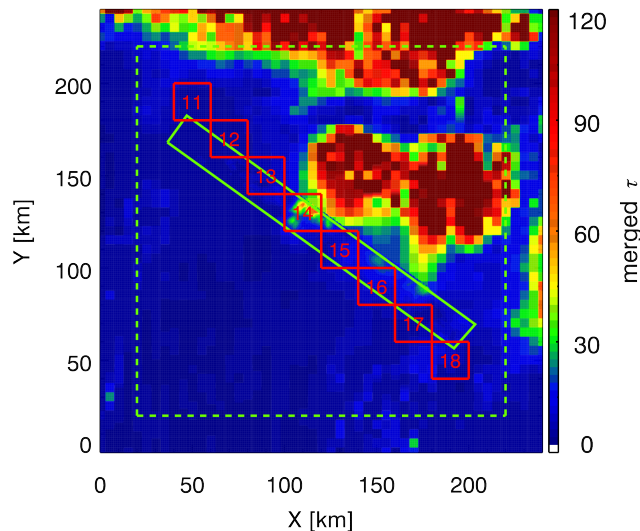


Figure 2.2: Optical thickness of the large-scale cloud field. The green rectangle marks the embedded MAS swath (Figure 2.1); the red squares mark 20 km “super-pixels” within the scene. Radiative transfer model output outside the dashed green square is discarded (see §2.7).

Figure 2.2 shows the extended cloud scene ($240 \text{ km} \times 240 \text{ km}$). Outside the MAS swath, GOES-11 retrievals were used instead of those from MAS. Similarly, as for the sub-scene cloud, the effective radius retrieval was extended throughout the vertical dimension. The optical thickness was distributed vertically using the CRS profile with the closest match in column-integrated water path (as compared to the retrieved value from GOES) and adjusted in altitude to match the cloud top height retrievals from GOES-11. This approach for distributing profile information from active instrumentation across the swath of a passive imager is more simplistic than that developed by *Barker et al.* [2011] who used multi-spectral radiances from MODIS. Transferring radar information to off-nadir pixels as far away as 120 km is not necessarily justified due to spatial de-correlation of cloud systems [Miller et al., 2014]. However, in the absence of any other information, it was considered the best alternative to estimating the cloud vertical structure without any *a priori* knowledge.

2.4 Model calculations

The calculations in this study were performed with the 3D Monte Carlo Atmospheric Radiative Transfer Simulator (MCARaTS: [Iwabuchi, 2006]). MCARaTS is an open-source code written in FORTRAN-90, which can be obtained at sites.google.com/site/mcarats/. It calculates shortwave and longwave spectral or broadband radiances and irradiances based on a forward propagating photon transport algorithm. It is optimized to run efficiently on parallel computers.

In addition to the two 3D cloud fields described in §2.3, the standard tropical summer atmosphere as distributed within the libRadtran radiative transfer package (www.libradtran.org: [Mayer and Kylling, 2005]) was used to prescribe the vertical profile of temperature, pressure, water vapor, and other atmospheric gases. For gas molecular

scattering, we calculated the optical thickness for each layer with the approximation by *Bodhaine et al.* [1999] and selected the Rayleigh scattering phase function from MCARaTS. For gas molecular absorption, we adopted the correlated k -distribution method described by *Coddington et al.* [2008]. It was originally based on *Mlawer and Clough* [1997], modified for the shortwave by *Bergstrom et al.* [2003], and was specifically developed for the Solar Spectral Flux Radiometer (SSFR: [*Pilewskie et al.*, 2003]). The SSFR instrument line shape (6-8 nm full-width half-maximum) defines the width of the channels in this study (narrower than MODIS or MAS channels). The spectrum by *Kurucz* [1992] served as the extraterrestrial solar spectrum.

Calculations were performed at eleven wavelengths ranging from the near ultraviolet to the very-near infrared (350, 400, 450, 500, 550, 600, 650, 700, 750, 800, 1000 nm) to capture the spectral dependence of horizontal photon transport over a wide range of molecular scattering. At 1000 nm, molecular scattering is negligible and water vapor absorption is small; cloud absorption is negligible for all wavelengths. For pixels dominated by ice clouds, the scattering phase function and single scattering albedo were used from the general habit mixture of the ice cloud bulk models developed by *Baum et al.* [2011] (parameterized by the effective radius). For liquid water clouds (minority of cloud pixels), single scattering albedo and asymmetry parameter from Mie calculations were used in conjunction with a Henyey-Greenstein phase function (which generally simplifies irradiance calculations). In this study, all calculations were performed for an ocean surface albedo [*Coddington et al.*, 2010] and for a solar zenith angle of 35° for consistency with the earlier publication by *Schmidt et al.* [2010]. The solar azimuth angle was 60° (northeast). This will be generalized in future work. For each wavelength, 10^{11} (10^{12}) photons were used for the sub-scene (large-scale) cloud field, respectively. MCARaTS was run in the

forward irradiance mode with periodic boundary conditions. For each 3D model run, calculations were also performed using the independent pixel approximation (IPA) where horizontal photon transport is deactivated.

2.5 Relationship between cloud spatial structure, net horizontal photon transport, and its spectral dependence

This section discusses the relationship between spatial structure and spectrally dependent horizontal photon transport based on the small sub-scene. Since true absorption, A_λ , is negligible, H_λ is equal to V_λ , the vertical flux divergence of an inhomogeneous cloud layer as defined in §2.2, with $h_{\text{top}} \approx 13$ km and $h_{\text{base}} \approx 8$ km.

Table 2.1: Cloud optical thickness τ , effective radius r_e , and values of H_0 and S_0 for the eight pixels highlighted in Figure 2.1 (sorted by H_0). For pixels 5, 6, 7, 8, Figure 2.3a shows the spectral shape of H_λ .

Pixel	τ	r_e [μm]	H_0 [%]	S_0 [%/100 nm]
6	10.3	27.5	28.92	2.36
1	13.0	30.1	21.17	1.56
3	21.2	30.0	13.04	1.08
2	18.1	30.6	9.92	1.63
5	12.2	27.5	4.95	0.48
7	8.0	27.8	-5.18	-0.78
4	11.8	28.2	-18.7	-1.54
8	7.7	24.2	-24.13	-2.46

Table 2.1 shows the optical thickness and effective radius for the eight highlighted pixels from Figure 2.1 along with H_0 , the horizontal photon transport at $\lambda=500$ nm, expressed in percent of the incident irradiance. Positive values of H_0 are related to net photon loss to other pixels (“radiation donors”), negative values to net photon gain (“radiation recipient” pixels). In the small domain, values as high as 50% and as low as –125% were attained. H_0 cannot exceed 100%, but may go below –100%, in which case the radiation received through the sides of a column or voxel exceeds that from the top of the domain. Table 2.1 is sorted by H_0 rather than by optical thickness. It shows immediately that there is no relationship between the optical thickness (or cloud reflectance) and horizontal photon transport. For example, pixel #6 is a “radiation donor,” whereas pixel #4 with roughly the same optical thickness is a recipient. For the extreme case of zero cloud optical thickness, the effect of horizontal photon transport had previously been observed as clear-sky radiance enhancement in the vicinity of clouds [Wen *et al.*, 2007; Várnai and Marshak, 2009]. Statistically, this enhancement is a function of the distance of a pixel to the nearest cloud. However, the horizontal scale of this dependence varies with the spatial context. Consequently, the distance to a certain cloud element cannot generally be used to parameterize 3D cloud effects for individual pixels, whether cloud-free or cloud-covered. This is illustrated when considering pixels #4-#8 in the anvil outflow, which have low optical thickness (around 10) compared to the convective core (optical thickness ≥ 40) overflown from 15.45-15.48 UTC. The small contrasts in optical thickness (reflectance) between the pixels in close proximity tend to drive the sign of H_0 to a greater extent than the exchange of radiation with the (bright) core (for example, #6→#7, #5→#4, #7→#8, but not #5→#6). On the other hand, pixels #2 and #3 have relatively low values of H_0 although they have the largest optical thickness of all eight pixels. While still donors, the magnitude

of net horizontal flux to other pixels seems to be diminished by the vicinity to the convective core. Overall, the direction, let alone the magnitude of net horizontal flux, is difficult to predict from the distribution of optical thickness, emphasizing 3D effects as a non-local phenomenon.

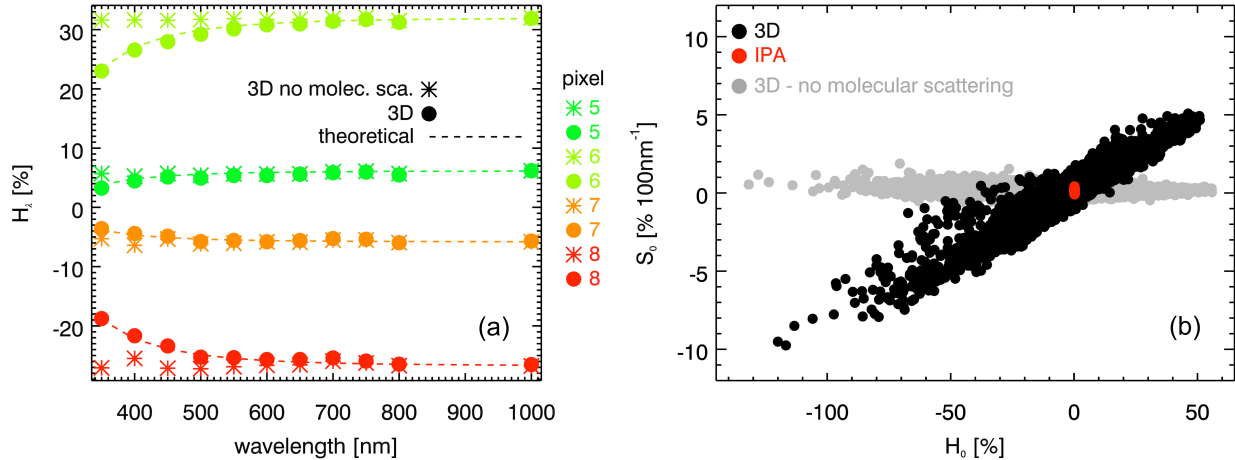


Figure 2.3: (a) The H_λ spectra of pixels {5,6,7,8} from Figure 2.1 and Table 2.1 with (•) and without (*) molecular scattering in the 3D calculations, as well as a fit based on Eq. (2.12) from §2.6 (dashed lines). (b) Spectral slope (S_0) vs. net horizontal photon transport (H_0) from (a) (both at 500 nm) for all the pixels from Figure 2.1. Only 3D calculations with molecular scattering (black dots) show the systematic correlation between H_0 and S_0 . Disabling molecular scattering (gray dots) incorrectly predicts a spectrally neutral (flat) H_λ ($S_0 \approx 0$ for all pixels). By definition, 1D calculations (IPA, red dots) do not reproduce net horizontal photon transport at all ($H_0 = 0$ for all pixels).

For the highlighted pixels in Table 2.1 (#5-#8), Figure 2.3a shows the spectral shape of H_λ . The absolute value H_λ increases with wavelength until it reaches an asymptotic value towards near-infrared wavelengths, which we denote H_∞ . Donor pixels ($H_\lambda > 0$) are associated with a positive spectral slope, $S_\lambda \equiv dH_\lambda/d\lambda > 0$; recipient pixels have a negative spectral slope. Remote sensing studies (e.g., [Marshak et al., 2008; Várnai and Marshak, 2009]) had previously established that the above-mentioned *radiance enhancement* for

clear-sky pixels near clouds was associated with “apparent bluing,” and proposed molecular scattering as the underlying cause for this spectral dependence. To demonstrate that the same effect is at work here, molecular scattering was deactivated in MCARaTS, keeping everything else the same in the calculations. In the resulting spectra (* symbols in Figure 2.3a), the wavelength dependence in the near-ultraviolet and visible range disappears almost entirely, suggesting molecular scattering as the primary cause for the spectral shape not only for clear-sky, but also for cloudy pixels. This begs the question (addressed in the next section) of how it is possible to observe such a significant spectral effect for cloudy pixels, given that cloud scattering outweighs molecular scattering by far. After turning molecular scattering off, the remaining variability in H_λ is due to the weak dependence of cloud scattering properties on wavelength and droplet or crystal effective radius, as well as minor gas absorption features.

To first order, the spectral shape over the range of 350 to 650 nm can be characterized by a single number—the spectral slope at $\lambda = 500$ nm, S_0 (obtained from a linear fit to $H_{\lambda=350-600}$ nm). Table 2.1 lists the value of S_0 for the eight pixels from Figure 2.1, whereas Figure 2.3b depicts the relationship between H_0 and S_0 for *every* pixel. It shows that not only the sign, but also the magnitude of the net horizontal photon transport, is surprisingly well correlated with its slope at 500 nm (in %/100 nm). This suggests that the phenomenon observed by *Schmidt et al.* [2010] for a few isolated data points is a general occurrence throughout a heterogeneous cloud field. The close relationship between the magnitude and spectral shape of net horizontal photon transport is the basis for the spectral parameterization of H_λ , developed in the next section.

In H_0 – S_0 space, all IPA calculations (red dots in Figure 2.3b) are reduced to the origin because they do not allow pixel-to-pixel radiation exchange by definition. Owing to

periodic boundary conditions, the cloud domain average of H is zero. The calculations without molecular scattering (gray dots) confirm that molecular scattering dominates the spectral shape throughout the domain. The vertical spread of the gray data points is due to the other factors mentioned above (e.g., variability in cloud microphysics). To some extent, it is also apparent in the IPA calculations.

2.6 Physical mechanism and parameterization

Our interpretation of Figure 2.3 is that H_λ can be understood as the combination of two terms:

$$H_\lambda = H_\infty + \delta(\lambda). \quad (2.7)$$

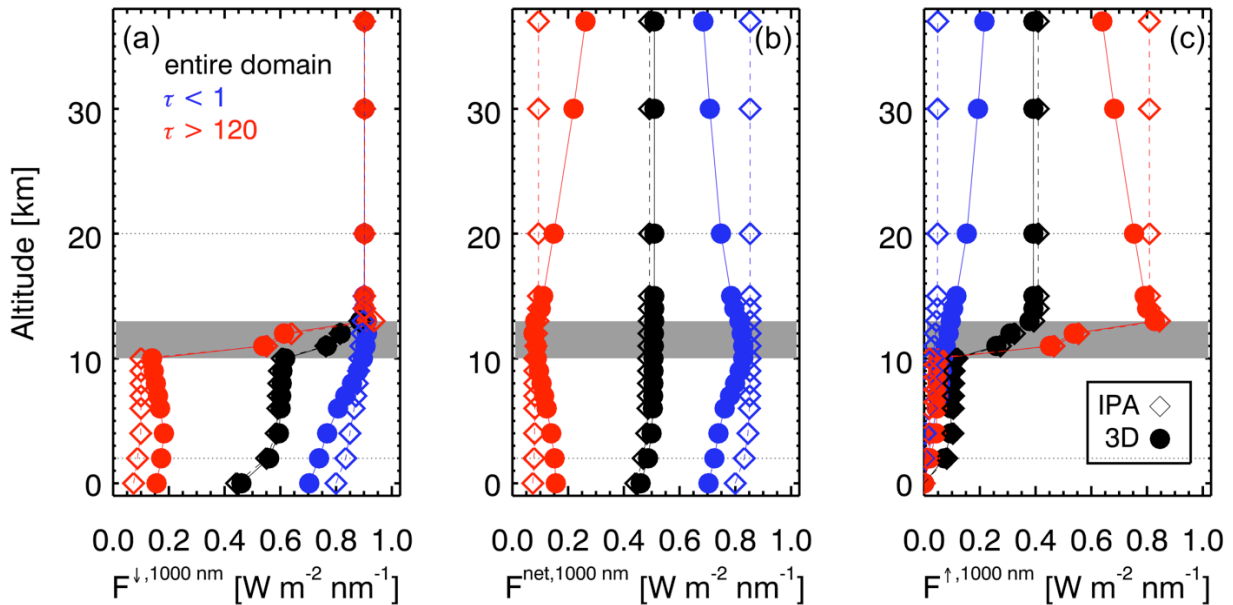


Figure 2.4: Profiles of (a) downwelling, (b) net, and (c) upwelling irradiance at 1000 nm for cloud field from Figure 2.1. The location of the cloud layer is marked in gray. Both IPA (dashed line, hollow symbols) and 3D calculations (solid line, full symbols) are shown, averaged over the full domain (black), over all columns with $\tau < 1$ (blue) and over columns with $\tau > 120$ (red).

1. The constant offset H_∞ is caused by column-to-column radiation exchange between cloud elements. This is illustrated by Figure 2.4, which shows the vertical profile of (a) downwelling, (b) net, and (c) upwelling irradiance at 1000 nm wavelength for the cloud field from Figure 2.1. A change of net irradiance between altitudes z_0 and z_1 corresponds to net radiation loss or gain within that layer. In this case, the domain-averaged profile of net irradiance (black line in Figure 2.4b) decreases slightly near the surface, due to small absorption in the wing of the 936 nm water vapor band⁸. When subsampling over columns with a cloud optical thickness $\tau < 1$, or $\tau > 120$, the 3D calculations differ from the IPA calculations because column-to-column radiation transfer is enabled. Above the cloud field, columns with high cloud optical thickness have higher reflectance than the domain average (Figure 2.4c) and collectively lose radiation to those with lower optical thickness; the opposite is true below the cloud where columns with high optical thickness have lower transmittance (Figure 2.4a). The magnitude of the net horizontal photon transport (the difference of net irradiances at the bottom and top altitude of a layer) increases with the geometrical layer thickness. Figure 2.5 conceptually depicts the processes at work. Above clouds, net horizontal photon transport (reflected radiance, projected into a horizontal plane) occurs from the high- to low-reflectance column. Below clouds, the direction is reversed because the transmittance of thin clouds is larger than that of thicker clouds.⁹ This simplified figure should *not* be interpreted to suggest that the net

⁸ Alternative choices would be 860 nm (although with non-negligible molecular scattering) or 1040 nm (with small cloud absorption under certain conditions, see *LeBlanc et al.* [2015]).

⁹ Note that below $\tau \approx 4$, directly transmitted radiation dominates the downwelling irradiance, and the cloud may not act as a “diffuser” as shown in Figure 2.5. The direction of the green arrows is then along the direct beam.

horizontal transport generally occurs along gradients of cloud optical thickness. As stated above, its direction and magnitude depends not only on directly adjacent columns, but also on the large-scale context, which is why a parameterization of 3D cloud effects in clear-sky areas in terms of the distance to the nearest cloud is only possible in a statistical way, but not on an individual pixel basis [Wen *et al.*, 2007]. The value of H_∞ can be obtained from H_λ for wavelengths where molecular scattering becomes negligible and where cloud and gas absorption are small compared to H_λ : $A_\lambda \ll H_\lambda$. For the purpose of this study, we chose $\lambda = 1000 \text{ nm}$: $H_\infty \approx H_{\lambda=1000 \text{ nm}}$.

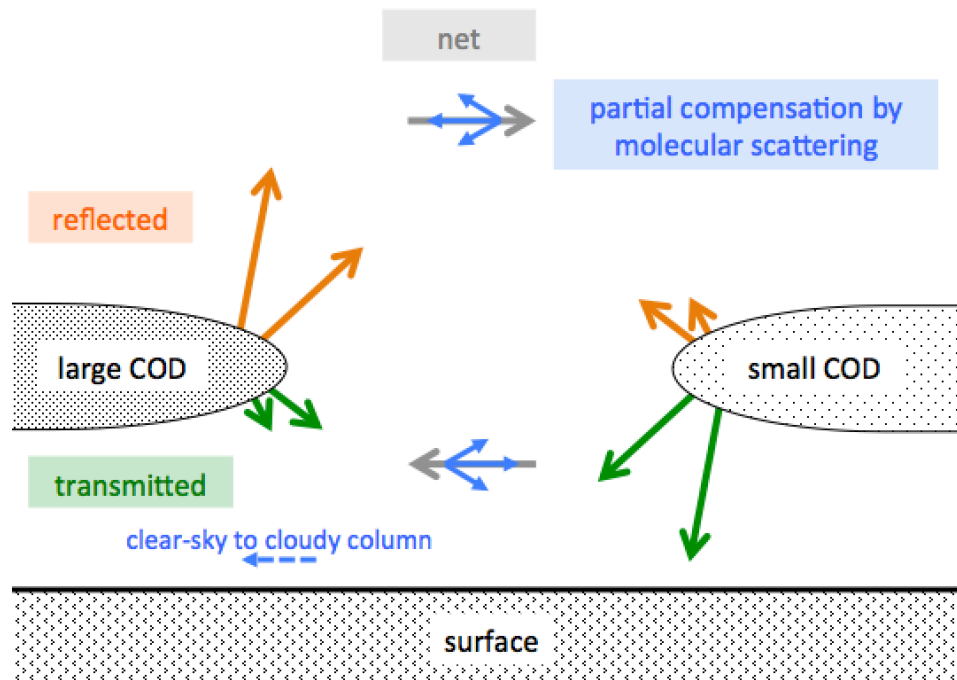


Figure 2.5: Conceptual visualization of the mechanism of horizontal photon transport.

2. The spectral perturbation $\delta\lambda$, superimposed on H_∞ , introduces the wavelength dependence of H_λ . It is perhaps not immediately intuitive why molecular scattering would reduce the magnitude of H_λ as indicated by the symbolic blue arrows in Figure 2.5. Molecular scattering essentially reduces the directionality of horizontal photon transport by redistributing radiation, part of which can then be detected as enhanced clear-sky reflectance of clouds [Marshak *et al.*, 2008]. A different, secondary process occurs when radiation is scattered out of the direct beam in clear-sky areas into cloud shadows (dashed blue arrow in Figure 2.5). It is spectrally dependent as $\delta\lambda$ but, unlike $\delta\lambda$, *independent* of H_∞ and its direction—thus increasing the net radiation under both optically thick and thin clouds. For 550 nm wavelength and shorter (not shown in Figure 2.4), the net irradiance does indeed increase towards the surface, both for $\tau > 120$ and for $\tau < 1$. This secondary effect is not explicitly captured by the first-order parameterization given below.

We express the proportionality of $\delta\lambda$ to H_∞ as

$$\delta(\lambda) = -\varepsilon \left(\frac{\lambda}{\lambda_0} \right)^{-x} H_\infty \quad (\varepsilon \geq 0, \lambda_0 = 500 \text{ nm}), \quad (2.8)$$

where $(\lambda/\lambda_0)^{-x}$ describes the wavelength dependence, and ε is the constant of proportionality. The layer thickness for which H_λ is derived affects both H_∞ and $\delta\lambda$, but only marginally changes the correlation *between* them. Therefore, ε is a general parameter that can be used for relating spatial inhomogeneities and spectral signature of a cloud scene as a whole. It depends on scene parameters such as surface albedo, solar zenith angle, and cloud micro- and macrophysics (including vertical structure). This dependence and the secondary effect due to molecular scattering mentioned above will be explored in a follow-on

publication (§4.1). Using Eq. (2.8), the spectral slope S_0 from the previous section can then be derived as

$$S_0 = \left. \frac{dH_\lambda}{d\lambda} \right|_{\lambda=\lambda_0} = \left. \frac{d\delta(\lambda)}{d\lambda} \right|_{\lambda=\lambda_0} = x\varepsilon \frac{H_\infty}{\lambda_0}, \quad (2.9)$$

By combining Eqs. (2.7) and (2.8), one obtains $H_0 = H_{\lambda=500 \text{ nm}} = H_\infty (1 - \varepsilon)$, and Eq. (2.9) can be rewritten as

$$S_0 = \frac{x\varepsilon}{1 - \varepsilon} \frac{H_0}{\lambda_0}, \quad (2.10)$$

where $x\varepsilon/(1 - \varepsilon)\lambda_0$ is the slope of the linear regression derived using all pixels in the cloud domain (for example, Figure 2.3b). Alternatively, one can derive both ε and x for each individual pixel from the regression of

$$\log\left(-\frac{\delta(\lambda)}{H_\infty}\right) = \log\varepsilon - x \log\frac{\lambda}{\lambda_0} \quad (2.11)$$

with $\log\varepsilon$ as the intercept and x as the slope, as shown in Figure 2.6a. In this example, the fit parameter is about 4 as would be expected if molecular scattering is the underlying physical mechanism. The two-dimensional PDF $p(x, \varepsilon)$ for the population of pixels in the domain peaks at $\{x, \varepsilon\} \approx \{3.85, 0.065\}$ but has a considerable spread in both parameters, which is caused by pixels with negligible horizontal photon transport (and consequently large uncertainties in the fit parameters). The dashed lines in Figure 2.3a show the fitted spectra (labeled “theoretical”) from this approach. For practical purposes, we fix $x \equiv 4$ for the remainder of this paper. This allows using

$$H_\lambda = H_\infty \left(1 - \varepsilon \left(\frac{\lambda}{\lambda_0} \right)^{-4} \right) \quad (2.12)$$

instead of Eq. (2.11) and deriving ε and H_∞ for each pixel from a linear regression of H_λ versus $(\lambda/\lambda_0)^{-4}$ (i.e., H_∞ is no longer a required input parameter as for the logarithmic regression).

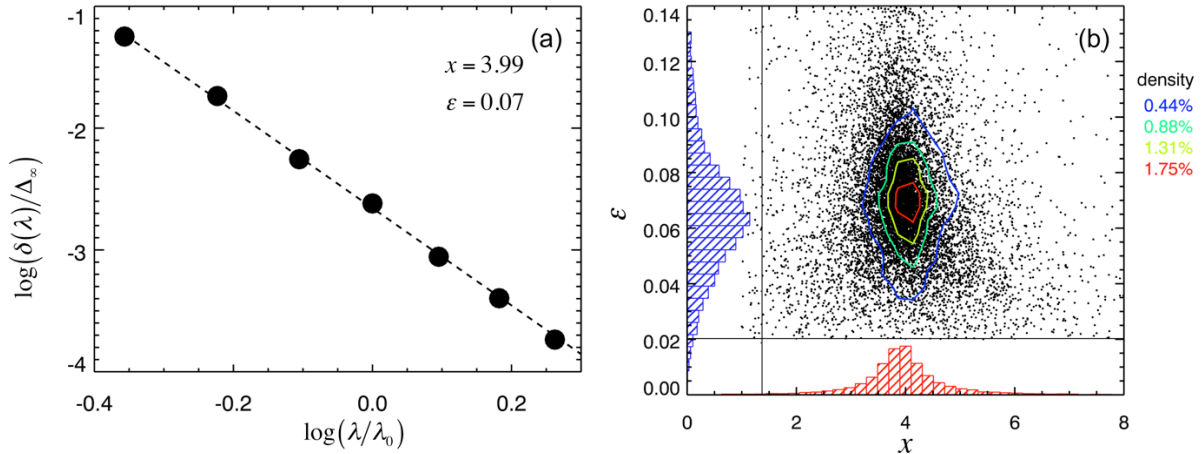


Figure 2.6: (a) An example of the linear regression between $\log(\delta(\lambda)/H_\infty)$ versus $\log(\lambda/\lambda_0)$, from which the values of x and ε can be derived. (b) The scatter plot of x versus ε for all pixels, joint PDFs $p(x, \varepsilon)$ (contours) as well as the marginal PDFs $p(x)$ and $p(\varepsilon)$ (histograms). The peak of $p(x, \varepsilon)$, and thus the most likely $\{x, \varepsilon\}$ values for the cloud field, is located at $\{3.85, 0.065\}$, and the domain-averaged values are $\{3.91, 0.070\}$.

With ε known, S_0 can be calculated from Eq. (2.9)¹⁰, and a domain-wide “effective” ε can be derived from the slope of the regression line of S_0 versus H_0 for all pixels (Eq. (2.10) with $x = 4$). Figure 2.7 shows the distribution of ε as derived from (2.12) for all those pixels with $\Delta(\varepsilon) < 5\%$. The median of this distribution (0.069) is almost identical to the “effective” value of ε (0.067). The standard deviation of the distribution is about 0.01. This means that the parameterized correlation between net horizontal transport and its spectral

¹⁰ This is more accurate than derivation of the slope from a linear fit to the spectrum as used for Figure 2.3, which, due to the non-linearity of the spectral dependence, differs from that of the tangent if finite wavelength intervals are used.

dependence can be applied to the domain as a whole as well as for individual pixels; if the spectral shape of H_λ is known, one can infer its magnitude throughout the near-ultraviolet and visible wavelength range. The correlation is robust regardless of the cloud context of a pixel, which is remarkable given the considerable variability in distance-based measures of 3D cloud effects [Várnai and Marshak, 2009].

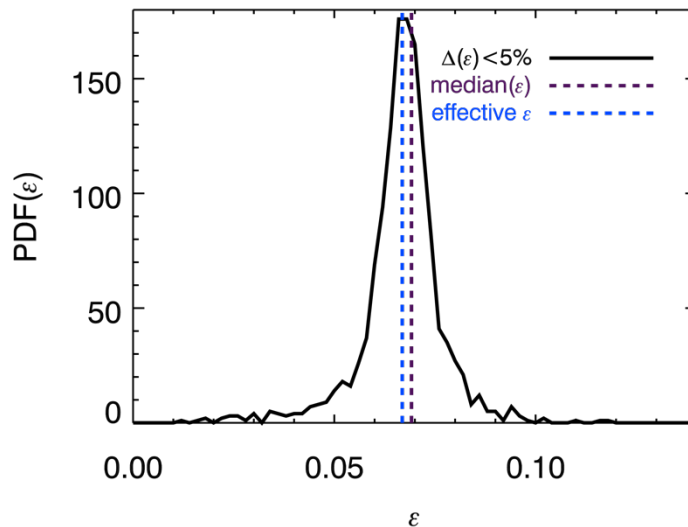


Figure 2.7: PDF of ϵ for all pixels with $\Delta(\epsilon) < 5\%$, median (purple dashed line), and domain-wide effective ϵ derived from regression of S_0 vs. H_0 (blue dashed line).

Although our study was instigated by aircraft measurements, its findings are also relevant for satellite-based derivations of cloud radiative effects since the spectral perturbations δ_λ propagate into observed radiances and imprint a spectral signature of H_λ [Song *et al.*, 2016b]. In this context, it is important to emphasize the fundamental difference between radiance and irradiance and their observation from space and aircraft, respectively. Radiances are mainly affected by radiative smoothing and roughening within a cloud layer (e.g., [Marshak *et al.*, 2006]). In addition, aircraft measurements also exhibit geometrical smoothing in their power spectra [Schmidt *et al.*, 2007a], especially when

acquired high above a cloud field. For this reason, radiance-derived cloud albedo products such as from aircraft imagers [*Schmidt et al.*, 2007b; *Kindel et al.*, 2010] often do not match their measured counterparts. Through our study, we now understand why this mismatch (Figure 7 in *Kindel et al.* [2010]) is associated with a spectral inconsistency in the albedo spectra [*Schmidt and Pilewskie*, 2012]—it can simply be explained by the term δ_λ in Eq. (2.7).

In principle, the mean albedo of an inhomogeneous cloud field derived from CERES observations should be fairly insensitive to 3D effects because they are folded into empirical anisotropy models of such scene types.¹¹ By contrast, surface cloud radiative effects are much less constrained by direct CERES observations because cloud transmittance has to be derived from concomitant imagery. This is where biases introduced by H_λ are most significant. For the remainder of this paper, we therefore analyze the significance of H for varying degrees of spatial aggregation (§2.7) and make the connection to cloud transmittance (§2.8).

2.7 Scale dependence and spatial aggregation

The results presented so far (e.g., in Figure 2.3b) are based on calculations at a resolution of 0.5 km. The question is whether the correlation between the magnitude and spectral shape of H is scale invariant, and to what extent the effect of horizontal photon transport can be mitigated by spatial aggregation. To answer this question, we successively coarsened the pixel resolution to 15 km, the largest super-pixel contained within the MAS swath (Figure 2.1).

¹¹ This is only true if the empirical anisotropy models adequately accomplish the radiance-to-irradiance conversion.

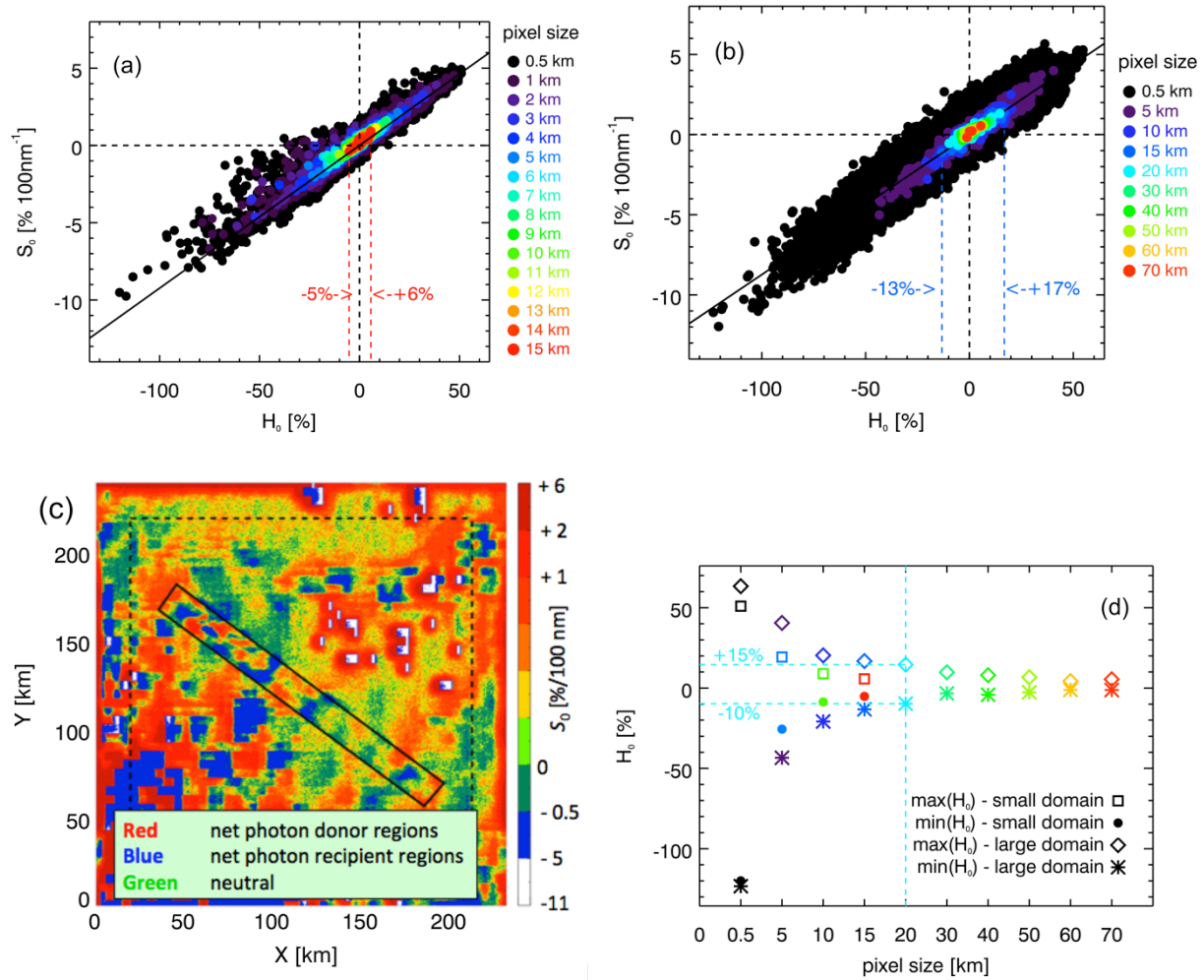


Figure 2.8: Scatter plot of S_0 versus H_∞ as obtained from linear regression of Eq. (2.12) for (a) the small domain from Figure 2.1 and (b) the large-scale domain from Figure 2.2, spatially aggregated to different scales, including the 20-km “super pixels” as highlighted in Figure 2.2 (red squares). The dashed lines indicate the range for 15 km pixels. (c) Spatial distribution of S_0 from (b). Red (blue) indicates net photon “donor” (“recipient”) pixels, and green “neutral zones” ($H_\lambda \approx S_0 \approx 0$). (d) Dependence of $\max(H)$ and $\min(H)$ on spatial aggregation scale (km). The color is the same as in (b).

Figure 2.8a shows that the correlation is indeed independent of the spatial aggregation scale and thus pixel size. The magnitude of H_0 decreases with pixel size: it ranges from +6% to -5% at 15 km resolution (close to CERES for nadir viewing), compared

to about $\pm 50\%$ at 1-5 km (resolution of various MODIS level-2 products). Eq. (2.1) suggests that neglecting horizontal photon transport will cause biases in pixel-level products such as cloud transmittance and surface insolation. In the next section, we will examine to what extent horizontal photon transport translates into 3D-1D transmittance biases. Here, we use the large cloud scene (Figure 2.2) to estimate for which aggregation scale beyond 15 km the magnitude of H_0 drops below the radiometric uncertainty of typical space- or ground-based radiometers (3-5%), at which point 3D cloud effects become insignificant from a radiative energy budget point-of-view.

The results for the large scene, shown in Figure 2.8b, confirm that the correlation is preserved for scales up to 70 km. However, H_0 at 15 km resolution varies from +17% to -13% throughout the large-scene domain, much more than in the MAS-only domain (+6% to -5%). One explanation for this larger range is the greater complexity of the large domain, providing a more extensive sample of cloud variability than the smaller sub-scene. This becomes quite clear when looking at the spatial distribution of horizontal photon transport: in Figure 2.8c, we chose to plot S_0 (y-axis in Figure 2.8b) rather than H_0 . They are practically interchangeable thanks to the correlation between the two. The distribution of effective donor, recipient, and neutral regions (red, blue, green, respectively) bears almost no resemblance to the optical thickness field from Figure 2.2. This demonstrates once again that horizontal photon transport cannot be derived from the spatial distribution of clouds in any simple way; strong contrasts between negative and positive H_0 (or S_0) can arise in optically thin boundary layer clouds (southwest corner of Figures 2.2 and 2.8c) as well as in optically thick areas (deep convection, northeast corner of cloud scene). Extracting the GOES-MAS large-scene results within the boundaries of the small MAS-only scene (marked by the green rectangle in Figure 2.8c) allows estimating the large-scale exchange of the

small domain with its context. The average value of H_0 within the small-scene subset is +7.9%, which means that the small scene effectively loses photons to its surroundings. This would not be detectable for such a large aggregation scale (where the entire MAS domain represents a single “super-pixel”). This net energy export is not reproduced by the calculations based on the MAS-only domain where the mean value of H_0 is zero, in keeping with energy conservation (satisfied by periodic boundary conditions in the radiative transfer model). The range of H_0 in the MAS-only sub-scene of the GOES-MAS scene is +17% to -6% at 15 km aggregation scale. This is still a larger range than obtained from the MAS-only calculations (+6% to -5%), even after sub-setting the results from the large scene to the boundaries of the small ones. The reason is simply that 15 km super-pixel size is already half the width of the MAS-only domain. Boundary conditions enforce the convergence of H_0 to zero as the area ratio of pixel to domain size approaches 1, which causes an underestimation of the variability of H_0 for large aggregation scales. By contrast, photons can also travel outside the confines of the domain in the real world as represented by the larger GOES-MAS cloud scene in our study.

This is illustrated in Figure 2.8d, which shows the range of H_0 for both the large and the small cloud scene as a function of aggregation scale. At small scales, the range is comparable for the small and large scene. At 15 km aggregation scale, the range obtained from the small scene has decreased to about half that of the large one. At 50 km pixel resolution, H_0 ranges from +7% to -3% (+5% to -1% at 70 km). It is likely that the boundary conditions imposed on the large domain also cause an underestimation of the H_0 variability at these large scales. Nevertheless, these results suggest that above 60 km super-pixel size (about 3×3 CERES nadir footprints), horizontal photon transport can be neglected for this cloud scene, based on a 3% uncertainty threshold. This is only true when

aggregating all native-resolution pixels, regardless of whether they are flagged as clear sky or as cloud-covered. However, sampling cloudy and clear pixels *separately* would result in much larger biases than 3% because high optical thickness pixels are more likely to be effective photon donors than low-optical thickness or clear pixels, causing an asymmetry in the distribution of H_0 [Song *et al.*, 2016b].

2.8 Significance for cloud radiative effect

In this section, we evaluate the ramifications of net horizontal photon transport on estimates of cloud radiative effects. For any atmospheric column, H is connected to R and T through Eq. (2.1) and manifests itself in a transmittance and reflectance bias:

$$\Delta T = T^{\text{IPA}} - T^{\text{3D}} \quad (2.13\text{a})$$

$$\Delta R = R^{\text{IPA}} - R^{\text{3D}}. \quad (2.13\text{b})$$

Juxtaposing energy conservation for a horizontally homogeneous atmosphere ($T^{\text{IPA}} + R^{\text{IPA}} = 1$) with Eq. (2.1) for conservative scattering ($T^{\text{3D}} + R^{\text{3D}} = 1 - H$) yields the plausible relationship

$$H = \Delta T + \Delta R, \quad (2.14)$$

which means that the error introduced by horizontal photon transport is partitioned into transmittance and reflectance bias. Since the bias ΔR is folded into the empirical radiance-to-irradiance conversion employed by CERES, we focus on ΔT in this study.

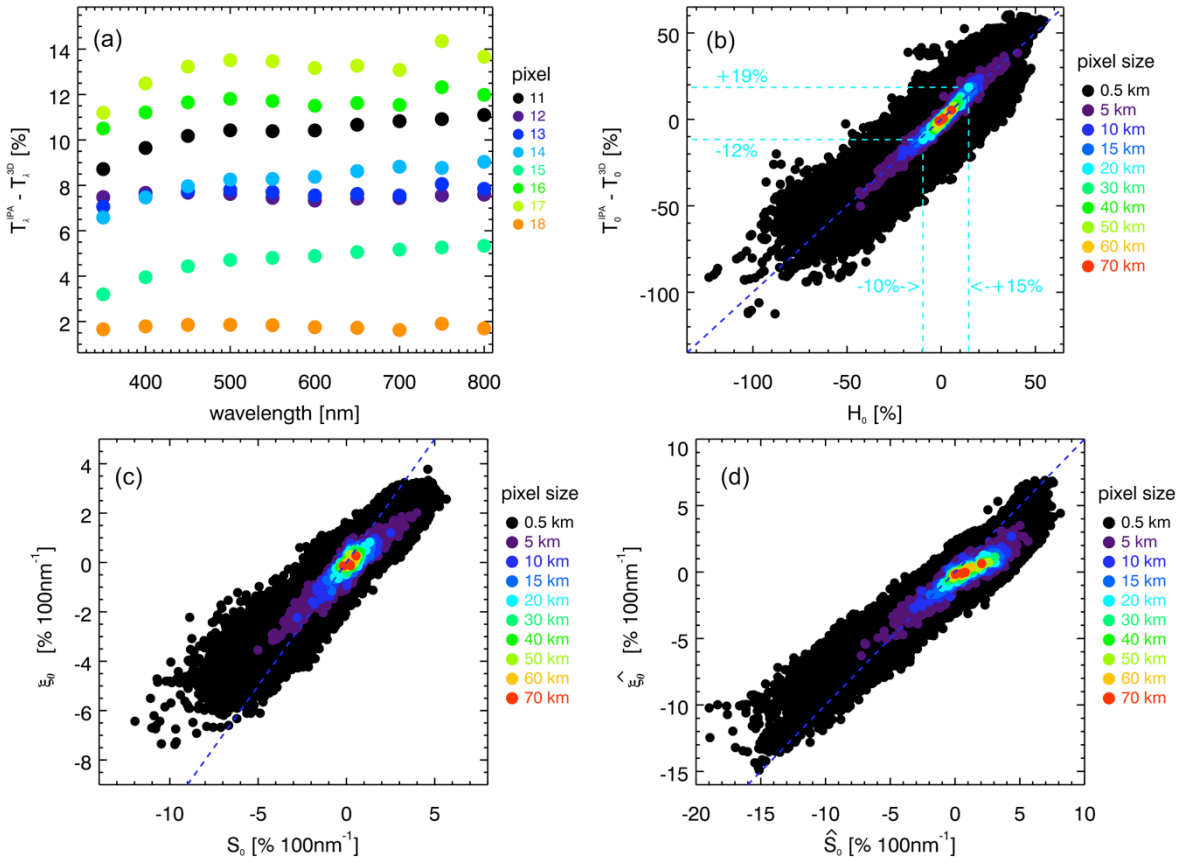


Figure 2.9: (a) Transmittance biases (IPA-3D transmittance) for the eight super-pixels from Figure 2.2. (b) Correlation between net horizontal photon transport from Figure 2.8b and transmittance bias for multiple spatial aggregation scales. The dashed lines indicate the range of variability for 20 km super-pixel size. (c) Correlation of the *slopes* of the quantities from (b). (d) Same as (c), but for a bracket from the surface to cloud top, rather than the cloud layer only.

For the eight super-pixels #11-#18 from Figure 2.2, Figure 2.9a shows the IPA bias ΔT , ranging from +2% to +14% in the mid-visible. Its spectral dependence is more complicated than the one shown for H in Figure 2.3a, with a less obvious correlation between magnitude and spectral shape. Nevertheless, Figure 2.9b shows a remarkable correlation between H_0 and ΔT_0 ($T^{\text{IPA}} - T^{\text{3D}}$ at 500 nm) for the same aggregation scales as in Figure 2.8b. For example, the H_0 range of +15% to -10% translates into +19% to -12% in ΔT_0 for a horizontal resolution of 20 km. Linear regression between H_0 and ΔT_0 suggests

that in this case, H_0 propagates mainly into ΔT_0 , whereas it is uncorrelated with ΔR_0 for scales below 20 km (Figure 2.10).

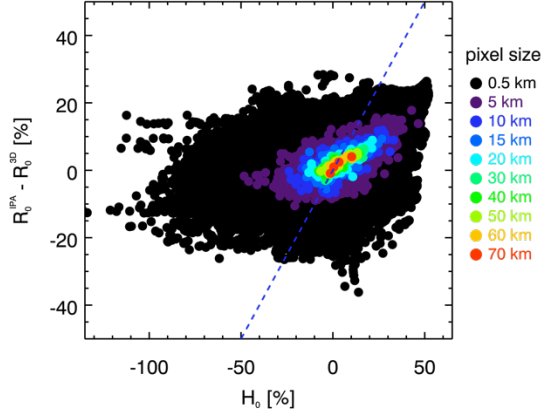


Figure 2.10: H_0 is only weakly correlated with ΔR_0 at scales below 15 km, which means that, statistically, biases introduced by horizontal photon transport propagate primarily into transmittance, not albedo. This changes for larger scales.

For simplicity, the spectral dependence of ΔT as shown in Figure 2.9a is approximated by

$$\Delta T_\lambda = T_\lambda^{IPA} - T_\lambda^{3D} = \xi_0 \Big|_{350-600nm} \times (\lambda - \lambda_0) + (T_0^{IPA} - T_0^{3D}); \lambda_0 = 500 \text{ nm} \quad (15)$$

where ξ_0 is the spectral slope of $T_\lambda^{IPA} - T_\lambda^{3D}$ calculated from the spectrum between 350 and 600 nm. Figure 2.9c shows that the spectral slopes of H and ΔT , S_0 and ξ_0 , are correlated despite the more complicated spectral dependence of T compared to that of H (Figure 2.9a). However, there is clearly no 1:1 relationship as found between H_0 and ΔT_0 above. For example, $S_0 = -10\%/100 \text{ nm}$ corresponds to only $\xi_0 = -6\%/100 \text{ nm}$. This changes when extending the vertical layer boundaries (8-13 km so far, bracketing only the cloud layer itself) to the atmosphere reaching from the ground to cloud top. This distinction is indicated by carets above all quantities. This is slightly different from the definition of \hat{T} in §2.2

where the upper boundary is the top of atmosphere, not the top of the cloud. Figure 2.9d not only shows a much stronger spectral dependence of $\Delta\hat{T}$ (surpassing that of \hat{H}) compared to that of ΔT and H in Figure 2.9c, but also that the correlation is no longer scale invariant. This means that the vertical bracket for deriving T , R , and H has to be chosen with consideration of the vertical location of the cloud layer. By contrast, the correlation between H and S as discussed in §2.6 is fairly independent of the layer boundaries.

For future studies of IPA-3D biases in satellite-derived estimates of surface cloud radiative effects, Figure 2.4b suggests the center of a cloud as upper boundary of the bracket where $\left|dF_{net}/dz\right|$ reaches a domain-wide minimum because 3D effects can be vertically separated into a transmittance and reflectance part below and above this level, respectively. Moreover, the correlation between ΔT and its spectral dependence x_0 (not shown) can be exploited to detect IPA-3D biases in ground-based irradiance measurements below cloud fields (§4.3). While our study suggests that horizontal photon transport mainly propagates into transmittance biases, there is some indication (Figure 2.10) that at scales above 20 km, non-zero values of H_0 translate into albedo (reflected irradiance) biases as well. This increasing correlation with scale is probably associated with the gradual de-correlation between \hat{S}_0 and $\hat{\xi}_0$ observed in Figure 2.9d. In order to improve satellite-based estimates of cloud radiative effects, it is important to understand how H_0 is partitioned into ΔT and ΔR [Eq. (2.14)] at different aggregation scales. A detailed study would need to be conducted for different cloud morphologies, sun angles, and surface albedos and is left for the future. Meanwhile, *Song et al.* [2016b] investigate the link between net horizontal transport in cloud fields and spectral perturbations in reflected *radiance*.

2.9 Summary and conclusions

Deriving the radiative effects of inhomogeneous cloud scenes from observations by satellite, aircraft, or at the surface is often portrayed as an intractable problem because it cannot be accomplished by isolating a pixel from its spatial context. At the core of the issue is pixel-to-pixel exchange of radiation, or net horizontal photon transport, which occurs over a range of scales. The original motivation for this study was to gain a physical understanding of this phenomenon's spectral dependence in the near-ultraviolet and visible wavelength range, which had been found in aircraft irradiance observations [Schmidt *et al.*, 2010]. We were able to identify molecular scattering as the underlying mechanism for the spectral dependence using three-dimensional radiative transfer calculations with cloud imagery and radar observations as input. When de-activating molecular scattering in the radiative transfer model, the wavelength dependence disappeared almost entirely in the vertical flux divergence V , which comprises net horizontal flux density H as well as true layer absorption A . To simplify the analysis, we limited our study to conservative scattering by choosing wavelengths with negligible gas or cloud absorption ($A \approx 0$), and by excluding aerosols. When activated in the model, molecular scattering manifested itself as a spectral perturbation (more accurately: modulation) $\delta\lambda$ to an otherwise *spectrally neutral* horizontal flux density H_∞ , which in turn could be traced back to horizontal exchange of radiation due to spatial inhomogeneity of cloud elements within the domain. Beyond the original scope of this study, we made a few surprising discoveries:

- (1) The spectral perturbation $\delta\lambda$ is not independent of the spectrally neutral part H_∞ caused by the clouds themselves. Instead, the mid-visible spectral slope of H_λ is

correlated with H itself (i.e., with the magnitude of the spectrally neutral part H_∞), which led to the simple parameterization

$$\delta_\lambda = -\varepsilon \left(\frac{\lambda}{\lambda_0} \right)^{-x} H_\infty.$$

(2) We were able to show that the exponent x is close to 4, which further confirmed molecular scattering as the dominating physical mechanism behind the spectral perturbation. The constant of proportionality, ε , can be regarded as universally valid for all pixels within the cloud domain, independently of the vertical or horizontal spatial distribution of clouds. This means that the spectrally dependent horizontal photon transport can be represented as

$$H_\lambda = H_\infty + \delta_\lambda = H_\infty \left(1 - \varepsilon \left(\frac{\lambda}{\lambda_0} \right)^{-4} \right)$$

for *each pixel* within the domain with $\varepsilon = 0.7 \pm 0.1$. It seems remarkable that one single value of ε should suffice to describe the relationship between the magnitude of H (caused by clouds) and its spectral dependence (imprinted on H by a completely different physical process, molecular scattering) – especially considering the range of different clouds within the domain. The correlation holds for each pixel, no matter what its spatial context may be. Once ε is established for a given cloud scene, the spectral perturbations associated with horizontal photon transport can be derived for each pixel if the value of H is known. Conversely, if the spectral shape of H is known, the value of H can easily be inferred. This may be especially significant considering that H cannot be directly observed from space. It is likely that the spectral perturbations will propagate into the observed radiances. Indeed, *Song et al.* [2016b] found evidence of this connection in aircraft data. In fact, *Várnai and*

Marshak [2009] previously reported this effect in clear-sky radiance observations near clouds. The close correlation that we found in our study may be a pathway to inferring the magnitude of H from its spectral manifestation in the observed radiances.

- (3) The correlation and parameterization hold for a range of spatial aggregation scales, and are fairly independent of the location of the bracketing altitudes that define the layer. This scale invariance only breaks down when extending a layer very close to the surface where a secondary spectral effect has to be factored in (see §2.6 and dashed arrow in Figure 2.5).
- (4) The observed correlation between H and its spectral shape can also be found between transmitted irradiance T and its spectral shape, although it is not scale invariant beyond 20 km.
- (5) H is correlated with ΔT , the IPA bias for each pixel, but not ΔR (at least at small scales). This means that 3D cloud effects in the form of horizontal photon transport translate almost exclusively into a transmittance bias. At scales above 20 km, a correlation between H and ΔR does emerge, which requires further study. The correlation between H and ΔT can potentially be exploited for ground-based spectral irradiance observations (§4.3).

Few of these findings could be expected at the outset of our research, and they evoke a number of new questions:

- (1) How does the discovered correlation and the constant of proportionality in its parameterization, ε , depend on scene parameters such as solar zenith and azimuth angle, surface albedo (magnitude and spectral dependence), and cloud morphology and microphysics? What “drives” the parameter ε ?

- (2) Can the spectral perturbations associated with H indeed be detected in reflected radiances, and can they be used to infer the magnitude of H indirectly?
- (3) Can the findings for the near-ultraviolet and visible wavelength range be generalized to the near-infrared wavelength range where clouds and atmospheric gases do absorb?
- (4) What are the implications of our findings for estimating aerosol radiative effects (such as heating rates) in presence of inhomogeneous cloud fields?
- (5) Can the method by *Ackerman and Cox* [1981] to correct for horizontal photon transport in aircraft measurements of atmospheric absorption by using a visible channel as basis for the correction of near-infrared absorption be upheld for future measurements, even in the modified form proposed by *Kassianov and Kogan* [2002]?
- (6) Can H and ΔT be derived from spectral perturbations in transmitted irradiance observations by ground-based spectrometers?

Question 2 will be partially addressed in Chapter 3 [*Song et al.*, 2016b]; questions 1, 3, 5, and 6 are discussed in Chapter 4 and will be further investigated in future publications. Furthermore, questions 3 and 4 are the subjects of active research in the framework of an ongoing or planned field missions (e.g., NASA ORACLES, dedicated to the radiative effects and remote sensing of aerosol in vicinity to clouds). This publication is a further contribution to the emerging field of cloud-aerosol spectroscopy [*Schmidt and Pilewskie*, 2012], which is expected to improve the estimation of cloud-aerosol parameters and their radiative effects through spectrally resolved observations from the ground, aircraft, and, ultimately, space.

Acknowledgement:

The research presented in this paper was supported by NASA grant NNX14AP72G (“Linking the Radiative Energy Budget and Remote Sensing of Cloud and Aerosol Fields”) within the radiation sciences program. The calculations were performed on the supercomputer “Janus,” which is supported by the National Science Foundation (award number CNS-0821794) and the University of Colorado Boulder. It is a joint effort of the University of Colorado Boulder, the University of Colorado Denver, and the National Center for Atmospheric Research. Janus is operated by the University of Colorado Boulder.

Chapter 3

Quantifying the spectral signature of heterogeneous clouds in shortwave radiation measurements

3.1 Introduction

Horizontal photon transport of shortwave radiation in spatially inhomogeneous scenes is one of the key processes causing biases in cloud remote sensing [*Marshak and Davis, 1996; Platnick, 2001*] and in radiative effect estimates from space [*Barker et al., 2012; Ham et al., 2015*]. In a recent study, *Song et al.* [2016a] examined this phenomenon with 3D radiative transfer calculations for an inhomogeneous cloud field observed by aircraft during the NASA Tropical Composition, Cloud and Climate Coupling (TC⁴) experiment. This led to the surprising discovery that the pixel-to-pixel net horizontal flux (H) of visible and near-ultraviolet radiation is accompanied by a characteristic spectral dependence, which can be described by a simple parameterization for each pixel in a domain:

$$H_{\lambda} = H_{\infty} \left(1 - \varepsilon \left(\frac{\lambda}{\lambda_0} \right)^{-4} \right) \quad (3.1)$$

where H_∞ is the asymptotic value of H_λ for $\lambda \gg \lambda_0 = 500 \text{ nm}$, and ε is a constant of proportionality, which *Song et al.* [2016a] found to be valid for all pixels within a domain. In absence of physical absorption A , H has the same magnitude as the vertical flux divergence V , as measured by aircraft legs above and below a cloud layer:

$$V_\lambda = \left[\frac{F_\lambda^{\downarrow,above} - F_\lambda^{\uparrow,above}}{F_\lambda^{\downarrow,incident}} - \frac{F_\lambda^{\downarrow,below} - F_\lambda^{\uparrow,below}}{F_\lambda^{\downarrow,incident}} \right] \times 100\% \quad (3.2)$$

because $V-H=A=0$.¹²

The discovery of the correlation between the magnitude and spectral slope of H evoked the first question of this chapter: Do the systematic spectral imprints in *irradiances* translate into spectral imprints in *radiances*, and can these be found in airborne *observations* of irradiances and radiances? Previous remote sensing studies that focused on clear-sky pixels in the vicinity of clouds [*Marshak et al.*, 2008; *Wen et al.*, 2008; *Várnai and Marshak*, 2009] reported that 3D cloud effects in radiance observations are indeed spectrally dependent in the near-ultraviolet and visible wavelength range. Our question generalizes these studies to clear-sky *as well as* cloudy pixels.

When establishing the connection between cloud remote sensing (based on radiance) and cloud radiative effects (that is, the cloud impact on irradiance fields), one needs to acknowledge that passive remote sensing does not allow direct measurements of H . If, however, the spectral dependence of the radiance fields were correlated with the magnitude of H , this could be an indirect way to estimate net horizontal photon transport from space, and ultimately correct for it.

¹² The “minus” sign ($-H$ instead of $+H$) on the left-hand side (total flux divergence) is simply due to the sign convention used throughout this thesis, as introduced by *Schmidt et al.* [2010] and employed by *Song et al.* [2016a].

Therefore, the second question of this chapter explores how such a radiance-irradiance connection can be established: Does it hold at the pixel level or through pixel populations? How does it vary between clear-sky and cloudy pixels? How does the relationship depend on scene parameters such as cloud spatial structure and surface albedo?

Finally, the third question addresses radiation closure, which in this context is understood as the consistency between the irradiance fields as obtained from remote sensing (cloud retrievals) and the measurements (in this case, below a cloud field): How large is the bias in the retrieval-based irradiance due to spatial cloud inhomogeneity? How can it be attributed to 3D effects on the retrievals (via radiances) and on the irradiances themselves when neglecting 3D radiative transport in the calculations?

Figure 3.1 and its caption provide a roadmap through this chapter and outline the relationship between the three science questions. The observations (marked in orange) were acquired during the NASA field experiment Studies of Emissions and Atmospheric Composition, Clouds and Climate Coupling by Regional Surveys (SEAC⁴RS, 2013 [*Toon et al.*, 2015]). The multi-spectral radiance fields were measured by the Enhanced MODIS Airborne Simulator (eMAS [*King et al.*, 1996; *Meyer et al.*, 2016]) onboard the NASA ER-2 aircraft, and the spectral irradiance fields by the Solar Spectral Flux Radiometer (SSFR [*Pilewskie et al.*, 2003]) onboard the ER-2 and the NASA DC-8. For a number of flight legs, the two aircraft were closely coordinated spatially and temporally. The ER-2 served as remote sensing platform at its nominal 20-km flight altitude, accompanied by the DC-8 within or below the cloud layer. From eMAS measurements of reflected radiances, cloud optical thickness fields (τ_{eMAS}) were retrieved using a one-dimensional (1D) radiative transfer framework, which ignores the context of a given pixel (Independent Pixel

Approximation, IPA). As a result, τ_{eMAS} may be biased with respect to τ_{true} . In this chapter we call this the *remote sensing bias*: $\Delta\tau_1 = \tau_{eMAS} - \tau_{true}$. The radiance and irradiance calculations (marked in green) were performed with the Monte Carlo Atmospheric Radiative Transfer Simulator (MCAraTS [Iwabuchi, 2006]). In lieu of the unknown true cloud optical thickness and effective radius, the eMAS retrievals were used as primary input. In addition to the remote sensing bias $\Delta\tau_1$, which propagates into the calculated irradiance fields, another error arises when ignoring 3D effects in these calculations, which we call *irradiance bias*. By isolating these two distinct biases, we aim to establish their relative importance in the radiation closure for inhomogeneous cloud scenes.

After introducing the data and model calculations in §3.2 and §3.3, the three science questions are addressed in §3.4 (SQ1 – spectral signature in radiances), §3.5 (SQ1 – spectral signature in irradiances), §3.6 (SQ2 – relationship between radiance and irradiance spectral perturbations), and §3.7 (SQ3 – radiation closure in transmitted irradiance), concluding with a summary. In Appendix §3.A, the remote sensing bias is estimated using model calculations, and Appendix §3.B discusses additional cloud cases that were left out for clarity in the body of the chapter. They provide a first glimpse into the impact of scene parameters such as surface albedo on the spectral perturbations caused by cloud inhomogeneities.

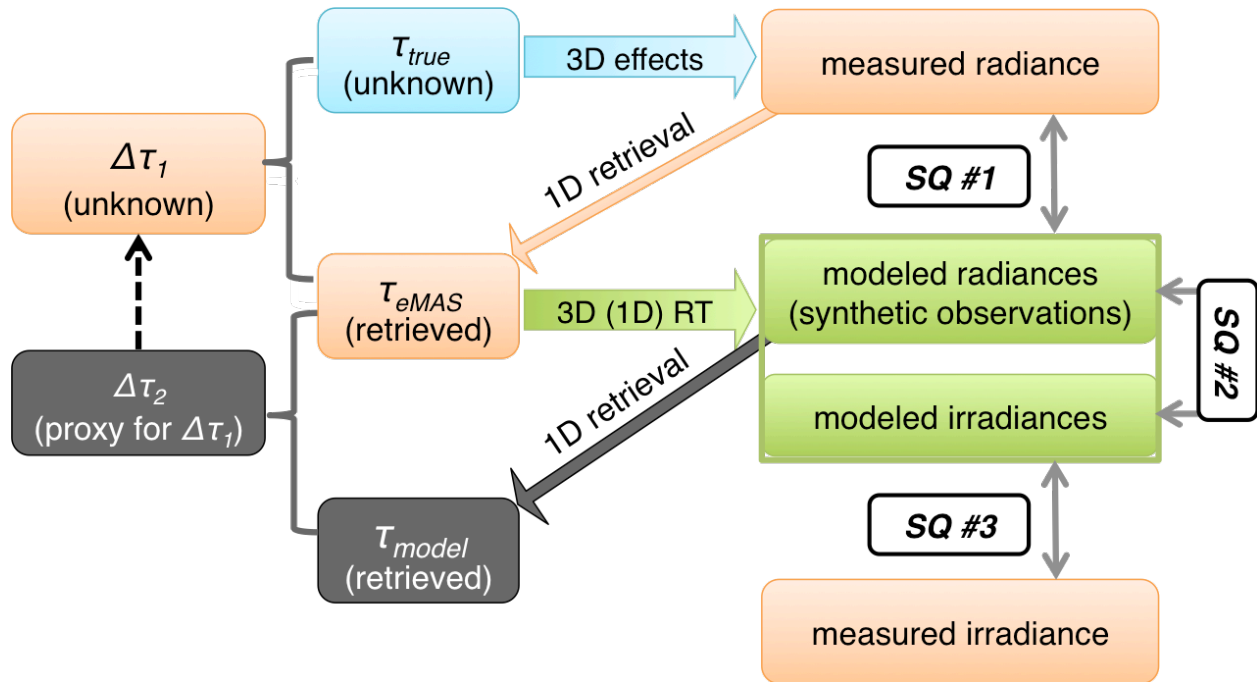


Figure 3.1: Visualization of the three science questions (SQ). The cloud distribution in a given scene (blue) translates into a reflected radiance field, which is measured by eMAS (orange) and mapped to an optical thickness field on the basis of 1D radiative transfer calculations (1D retrieval). The *remote sensing bias* ($\Delta\tau_1$) is the difference between retrieved and true cloud optical thickness. For SQ1, the retrieved cloud field is used in lieu of the unknown truth to calculate the associated radiance field with and without consideration of 3D effects (green). The modeled radiance field is then compared to the measurements, and the spectral radiance perturbations caused by 3D effects are linked to those in the associated irradiance fields (SQ2). For SQ3, the modeled irradiance field is validated with measurements by SSFR (orange) below the cloud field. The bias can be partitioned into the difference between 3D and 1D calculations (*irradiance bias*) and the *remote sensing bias* ($\Delta\tau_1$) that propagates into both 3D and 1D irradiances calculations. The impact of $\Delta\tau_1$ on the calculated irradiance can be estimated through $\Delta\tau_2$, the difference between the original eMAS retrieval and τ_{model} (retrieved from the 3D-modeled radiance field in the same way as τ_{eMAS} was obtained from the observed radiance field).

3.2 Data

Many of the questions posed in the introduction require combined radiance and irradiance observations for a range of cloud conditions. SEAC⁴RS data provides an unprecedented data set in this regard because the ER-2 and DC-8 were frequently flown in

close collocation. Four cases (summarized in Table 3.1) were selected for this study, based on the following criteria:

- (1) Sufficient spatial and temporal synchronization between ER-2 and DC-8
- (2) Availability of eMAS spectral radiance observations and cloud retrievals (ER-2)
- (3) Availability of SSFR spectral irradiance observations above (ER-2) and below (DC-8) the cloud layer
- (4) Varied cloud and surface types from case to case

Table 3.1 shows the range of cloud type, cloud thermodynamic phase, cloud top height, solar zenith and azimuth angles, and surface conditions for the studied cases. The eMAS-retrieved cloud optical thickness fields (Figure 3.2) illustrate the variability in terms of spatial cloud distribution, range of optical thickness, and degree of cloud heterogeneity.

Table 3.1: Descriptions of the SEAC⁴RS cloud cases.

Cases	Cloud type	Cloud phase	Cloud top height	Solar zenith angle	Solar azimuth angle	Surface type
20130816	Convective cells	Liquid	Isolated cell at ~7 km	27°	140° (south southeast)	Bare Soil
20130823	Scattered boundary layer	Liquid	~2 km	35°	-120° (west southwest)	Forest and scattered farmland
20130913	Anvil outflow	Ice	~13 km	18°	-160° (south southwest)	Ocean
20130916	Scattered boundary layer	Liquid	~0.5-2 km	35°	125° (east southeast)	Ocean

Case 1 (2013/08/16), 1804 to 1830 UTC, NE Arizona: The main objective for the flight legs from 1714 to 1912 UTC was to sample an aged smoke plume. We chose this particular leg because the aircraft encountered a convective system surrounded by scattered boundary layer clouds. Figure 3.2a shows the cloud optical thickness field

of the entire leg. In the remainder of the chapter, we focus on the segment from 90–130 km with two convective cells.

Case 2 (2013/08/23), 2004 to 2028 UTC, S Arkansas: On this day, one of the science objectives was to characterize the diurnal variability in biogenic emissions and their impact on boundary layer aerosols and convective cloud development. This leg was selected because the scene consisted of scattered boundary layer clouds (Figure 3.2b) over a heterogeneous vegetated land surface (forest mixed with farmland). The clouds were embedded in an aerosol layer (primarily biogenic). In addition, there was a layer aloft (advected aerosols). The combination of these factors makes this case the most complex one.

Case 3 (2013/09/13), 1832 to 1845 UTC, Gulf of Mexico: The two aircraft observed an anvil outflow cirrus from the tropical storm “Ingrid” (Figure 3.2c) and allows to study overcast ice clouds.

Case 4 (2013/09/16), 1546 to 1616 UTC, Gulf of Mexico: Two of the conditions (1 and 3) were not met for this case because it was only observed by the ER-2, allowing to address only a sub-set of the science questions. The ER-2 observed boundary layer broken clouds (Figure 3.2d) while heading towards the Yucatán channel to sample stratospheric air for chemical analysis. Because this scene occurred over ocean surface, the surface albedo along the flight leg varied only slightly compared to the other cases and therefore allows isolating the impact of cloud inhomogeneity on spectral perturbations in the radiance field.

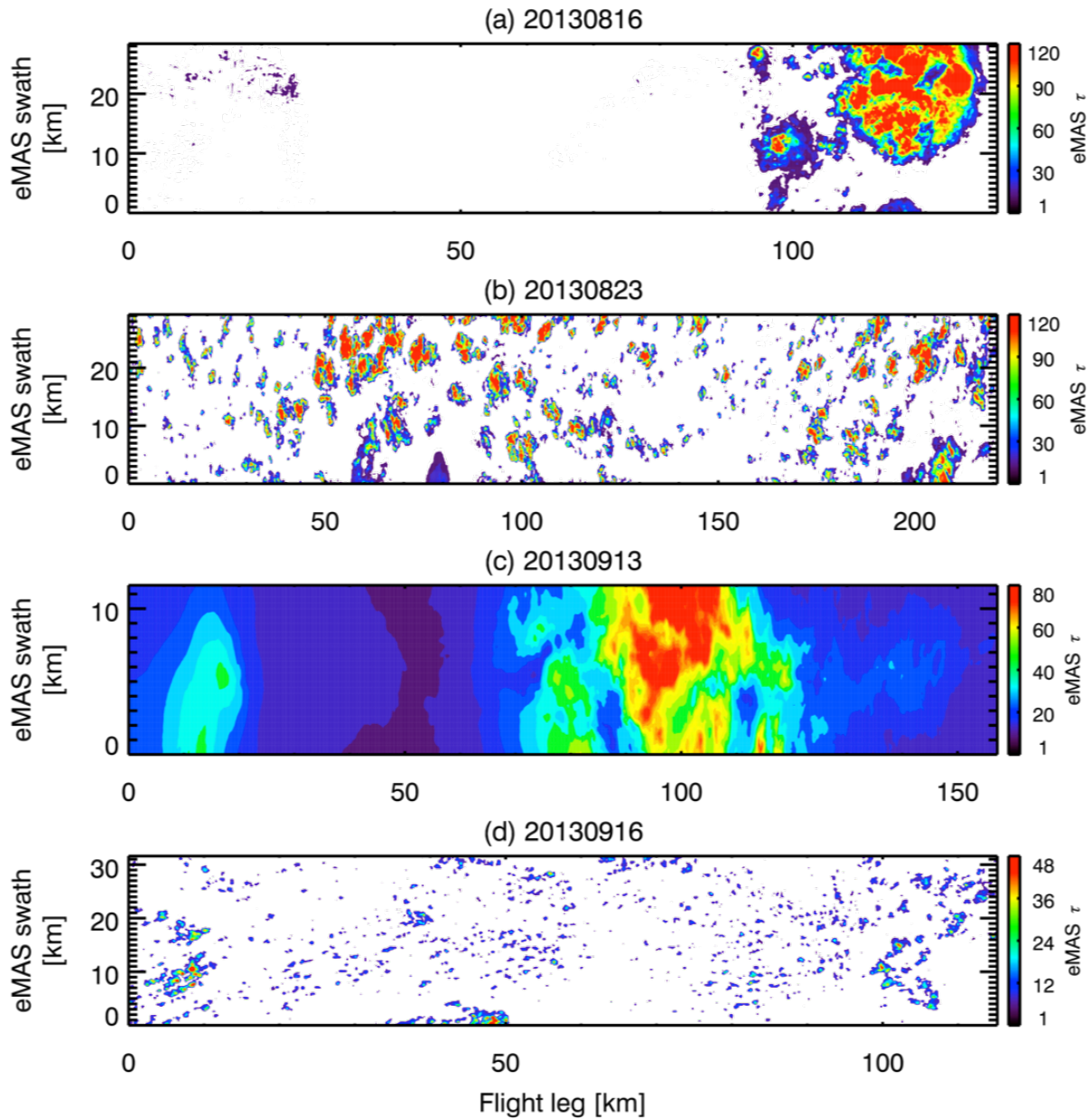


Figure 3.2: eMAS-retrieved cloud optical thickness fields for the four SEAC⁴RS cloud cases listed in Table 3.1. Note that the color bar varies from case to case.

For the first two cases, aerosols have to be accounted for in the radiative transfer calculations. However, as mentioned above, the SEAC⁴RS data set does not provide adequate data to study the radiative signature of aerosols in the context of inhomogeneous clouds. For this reason, this chapter focuses on clouds, which dominate the overall radiation

field in each of the studied cases. The minor contributions of aerosols to the spectral perturbations are not discussed separately, although they are included in the calculations.

Table 3.2: Data obtained during SEAC⁴RS, with instruments and platforms (boldface).

Instrument	Data Used
Enhanced MODIS Airborne Simulator (eMAS, ER-2) [<i>King et al.</i> , 1996; <i>Meyer et al.</i> , 2016]	Spectral radiance and cloud retrievals (optical thickness, effective radius, thermodynamic phase, and cloud top height)
High Spectral Resolution Lidar (HSRL, DC-8) [<i>Hair et al.</i> , 2008]	Vertical position of cloud and aerosol layers
Spectrometer for Sky-Scanning and Sun-Tracking Atmospheric Research (4STAR, DC-8) [<i>Dunagan et al.</i> , 2013]	Spectral aerosol optical thickness
In-Situ Aerosol Optical Properties (AOP, DC-8) [<i>Brock et al.</i> , 2011]	Aerosol asymmetry parameter
In-situ aerosol optical properties, NASA Langley Aerosol Research Group (LARGE, DC-8) [<i>Schafer et al.</i> , 2014]	Aerosol single scattering albedo
Solar Spectral Flux Radiometer (SSFR, DC-8 and ER-2) [<i>Pilewskie et al.</i> , 2003]	Spectral solar irradiance
MODIS Albedo product (MCD43C3 ¹³ [<i>Schaaf et al.</i> , 2002; 2011])	Spectral land surface albedo

Table 3.2 summarizes the data we used in this work along with the corresponding instruments and platforms. The eMAS-retrieved cloud properties were the main data source for generating the cloud input that is required for the radiative transfer model (introduced in §3.4). Additional information on the cloud top height distribution and the location of aerosol layers of a scene was obtained from the NASA Langley Airborne Differential Absorption Lidar – High Spectral Resolution Lidar (DIAL-HSRL [*Hair et al.*,

¹³ Land Processes Distributed Active Archive Center (LP DAAC), 2013, MODIS Albedo 16-Day Level 3 Global 0.05 Degree Climate Modeling Grid (MCD43C3). Version 5. NASA EOSDIS Land Processes DAAC, USGS Earth Resources Observation and Science (EROS) Center, Sioux Falls, South Dakota (<https://lpdaac.usgs.gov>), accessed October 1, 2013, at <http://e4ftl01.cr.usgs.gov/MOTA/MCD43C3.005/>.

2008]). The Advanced Airborne Precipitation Radar (APR-2) onboard the DC-8 [*Sadowy et al.*, 2003] is insensitive to non-precipitating clouds and therefore could not be used. Lacking pixel-by-pixel information on the cloud profile, a fixed cloud base was prescribed for each scene, based on visual records (in-flight camera and DC-8 SSFR operator’s logbook) and thermodynamic profiles (DC-8 and soundings). The eMAS-retrieved cloud optical thickness was then uniformly distributed between cloud base (fixed) and cloud top (variable). The resulting cloud layer boundaries for the four cases were 4-10 km (case 1), 1-4 km (case 2), 6-14 km (case 3), and 0.5-4 km (case 4).

The cloud droplet effective radius, defined as the ratio of the third moment to the second moment of the particle size distribution ($r_e = \overline{r^3} / \overline{r^2}$), was taken directly from the eMAS retrievals. It was assumed constant in the vertical in the radiative transfer model due to lack of information on cloud vertical structure. Cloud thermodynamic phase was also obtained from the eMAS retrievals. For water droplets, we derived the scattering properties by performing Mie calculations using the libRadtran radiative transfer package (www.libradtran.org; *Mayer and Kylling*, 2005). For ice particles, we used the scattering phase functions and single scattering albedos for the general habit mixture that are applied for retrieving Collection 6 cloud products for MODIS [*Baum et al.*, 2011].

For cases 1 and 2, the aerosol properties were obtained from a combination of DIAL-HSRL for the vertical structure of the extinction at 532 nm and the Spectrometer for Sky-Scanning and Sun-Tracking Atmospheric Research (4STAR [*Dunagan et al.*, 2013]) for the spectral optical thickness of the column above the aircraft. For case 1, the aerosol layer extended from the ground to 4 km altitude; for case 2 it resided between cloud tops and 4 km altitude. Averaged over the flight leg, the aerosol optical thickness at 501 nm was 0.091 and 0.245 for case 1 and 2, respectively. For cases 3 and 4 no aerosol information was

available, and the optical thickness was assumed to be below 0.05. At each pixel the aerosol optical thickness was distributed uniformly in the vertical within the aerosol layer. The nephelometer and the modified particle soot absorption photometer (PSAP) within the instrument package of the NASA Langley Aerosol Research Group (LARGE [Schäfer *et al.*, 2014], data version R2) were used to estimate ambient aerosol optical and microphysical properties [Virkkula *et al.*, 2005; Arnott *et al.*, 2003]. Based on these data, we used a spectrally constant value of 0.9 for case 1 and 0.95 for case 2. These numbers were based on the averaged value over the flight leg. The Aerosol Optical Properties (AOP [Brock *et al.*, 2011]) humidified ultra-high sensitivity aerosol size spectrometer (UHSAS) provided measurements of humidified aerosol size distributions; aerosol asymmetry parameters are included in the data set, derived from calculations for particles at ambient relative humidity. Based on the AOP data, we used a spectrally constant value of 0.6 for cases 1 and 2.

Since the ground speeds of the ER-2 and DC-8 were both approximately 200 m/s and the SSFR onboard both aircraft took measurements every second, the SSFR spatial sampling was approximately 200 meters. To allow direct comparisons with SSFR, the horizontal resolution of the 3D radiative transfer model (§3.3) was set at 200 meters. The eMAS native spatial resolutions ranged from roughly 15 to 45 meters depending on cloud top height of each case. We binned the eMAS cloud retrievals (level-2 products) and radiance data (level-1B products) to 200-meter resolution. The vertical resolution was 500 meters for boundary layer clouds (cases 1, 2, 4) and 1000 meters for anvil outflow (case 3).

3.3 Model calculations

Three-dimensional (3D) radiative transfer calculations are required for understanding irradiance and radiance measurements in scenes with a complex cloud or surface structure. Similarly to Chapter 2 [Song *et al.*, 2016a], we used the Monte Carlo Atmospheric Radiative Transfer Simulator (MCARaTS [Iwabuchi, 2006]), which performs irradiance and radiance calculations in forward photon tracing mode. For this study, the majority of radiative transfer calculations were conducted at thirteen wavelengths (380, 400, 420, 470*, 550*, 650*, 740*, 820*, 860*, 1000, 1240, 1640*, 2130* nm). Most of these were chosen to emulate eMAS channels (marked with asterisks, corresponding to eMAS channel numbers 1, 2, 3, 5, 6, 7, 10, 20). The spectral dependence of reflectance in the visible was derived from the three first eMAS channels with band centers at 465, 549, and 655 nm. In addition, the wavelengths 380, 400, 420, and 1000 nm were included to derive the spectral parameters related to H from Song *et al.* [2016a]. The wavelengths 1240, 1640 and 2130 nm correspond to MODIS channels. For consistency, the calculations were all performed for the SSFR instrument line shape with a full-width at half-maximum (FWHM) of 8-12 nm (depending on the wavelength). The radiance calculations were subsequently convoluted with the eMAS line shape (FWHM approximately 50 nm) for direct comparisons with the radiance measurements.

Because of the choice of wavelengths, the model calculations are not noticeably affected by gas absorptions. For simplicity, we therefore used a standard mid-latitude summer atmosphere, to prescribe the vertical profile of temperature, pressure, water vapor and other atmospheric gases. For molecular scattering, we calculated the optical thickness for each layer using the approximation of Bodhaine *et al.* [1999] and used the Rayleigh scattering phase function. For molecular absorption, we incorporated the absorption

coefficients calculated using a correlated k -distribution method [Coddington *et al.*, 2008] into the MCARaTS model. The spectral resolution of the absorption coefficients matches that of SSFR (8-12 nm). For the extraterrestrial solar spectrum, we used the spectrum published by Kurucz [1992].

For prescribing the spectral surface albedo in the model, we used the results from Coddington *et al.* [2010] for cases 3 and 4 (ocean) and the MODIS Albedo product MCD43C3 [Schaaf *et al.*, 2002] for cases 1 and 2 (land). The MODIS product provides a 16-day climatology at approximately 5.6-km spatial resolution. The quality and reliability of the MCD43C3 product is described by Schaaf *et al.* [2011] and is provided as a flag in the dataset. Since the spatial scale of the surface albedo inhomogeneity in the domain was usually smaller than the spatial resolution in the MCD43C3 dataset and because the MODIS product does not provide all the required wavelengths, we chose a domain-wide proxy spectrum from an ASTER-derived climatology [Baldrige *et al.*, 2009], based on the closest match with the domain-averaged MCD32C3 spectrum. This simplification has consequences for case 2 with pronounced surface albedo inhomogeneity (see §3.B.1). Obtaining the spectral surface albedo variability at an appropriate scale that is compatible with the horizontal model resolution is left to future studies. For case 1, the ground was sparsely vegetated, and the averaged MCD32C3 spectrum suggested the use of the “dry grass” albedo from the ASTER-derived climatology. For case 2, the MODIS product, as well as the high-resolution eMAS imagery (Figure 1.4) showed that the geographical area mainly consisted of forests with interspersed farmland, which was best represented by the “deciduous trees” spectrum (Figure 1.5).

For each wavelength and quantity (irradiance/radiance), 10^{11} photons were used in the Monte Carlo calculations, with period boundary conditions to ensure energy

conservation in the domain. Radiances were only calculated for one nadir-viewing angle (180°), corresponding to the center-swath eMAS pixels on the ER-2 flight track. In addition to the 3D calculations, the model was run in independent pixel mode (IPA, 1D calculations), in which horizontal photon transport is disabled.

3.4 Spectral signature of 3D cloud effects in radiance observations

In this section, we investigate the spectral imprint of heterogeneous clouds on measured and calculated radiances. Figure 3.3a shows the eMAS-measured reflectance field at 470 nm ($\mathfrak{R}_0 = \mathfrak{R}_{\lambda_0=470nm}$) for the case 1. The two convective cells were labeled #1 between 109.21°W and 109.02°W and #2 between 109.02°W and 108.88°W. On average, cell #1 had lower reflectance than cell #2. For pixels along the dashed line (~1 km off the ER-2 nadir track), the measured and modeled time series of \mathfrak{R}_0 are compared in Figure 3.3b. In general, the 1D model reproduces the measured reflectance because the input cloud optical thickness field for the model was originally retrieved from reflected radiances under 1D assumptions. However, the limitation of the 1D model is immediately obvious: In clear-sky regions near clouds, highlighted by the arrows, the 1D model is unable to capture the enhanced reflectance in sunlit zones or reduced reflectance in cloud shadows. These are 3D radiative transfer phenomena that are apparent only when the lateral radiation exchange between clear-sky and nearby cloud edge pixels is considered in the model. There are some cloudy regions, such as around 109.1°W, where the 1D-modeled reflectance does not match the measurements well. This mismatch indicates that the model cloud may not fully represent the real cloud in those regions, for example as a result of the simplified vertical cloud distribution assumption.

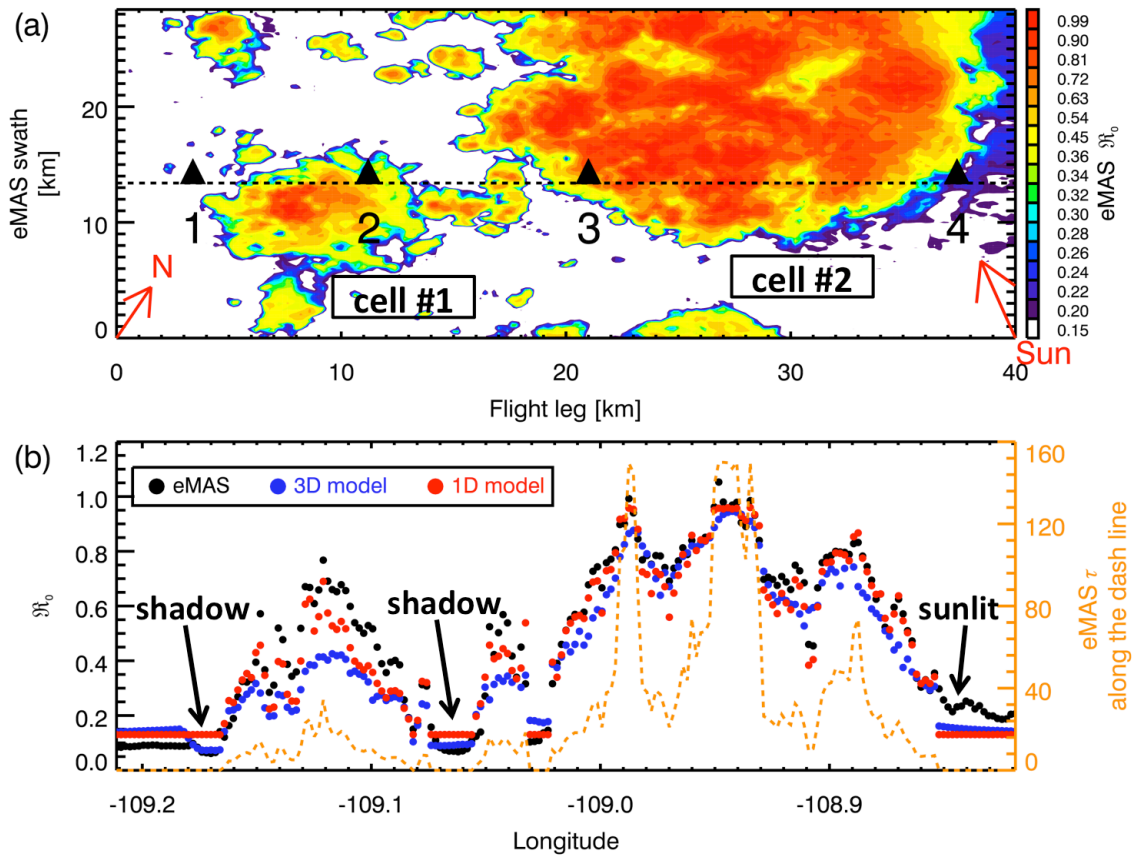


Figure 3.3: (a) eMAS-measured reflectance field at 470 nm (\mathfrak{R}_0) for case 1 (2013/08/16); the four pixels marked by triangles and numerical labels are placed in a shadow zone (1), on a cloudy pixel of cell #1 and #2 (2 and 3) and on a clear-sky pixel with enhanced reflectance (4); (b) Comparison of the measured (black), 1D- (red) and 3D-modeled (blue) reflectance along the dashed line in (a), plotted together with the eMAS-retrieved cloud optical thickness. The arrow “sunlit” marks a zone with enhanced reflectance.

Figure 3.4 shows the measured and modeled reflectance spectra within the spectral range from 470 to 600 nm ($\mathfrak{R}_{\lambda=470-600nm}$) for the four highlighted pixels along the ER-2 flight track. These pixels represent clear sky in cloud shadows (pixel #1), clouds with low reflectance (pixel #2), clouds with high reflectance (pixel #3), and clear-sky in sunlit zones (pixel #4). Previous studies have focused exclusively on the clear-sky regions in the vicinity of clouds, like that represented in pixel #4 (*Marshak et al.* [2008]; *Wen et al.* [2008]; *Várnai and Marshak* [2009]).

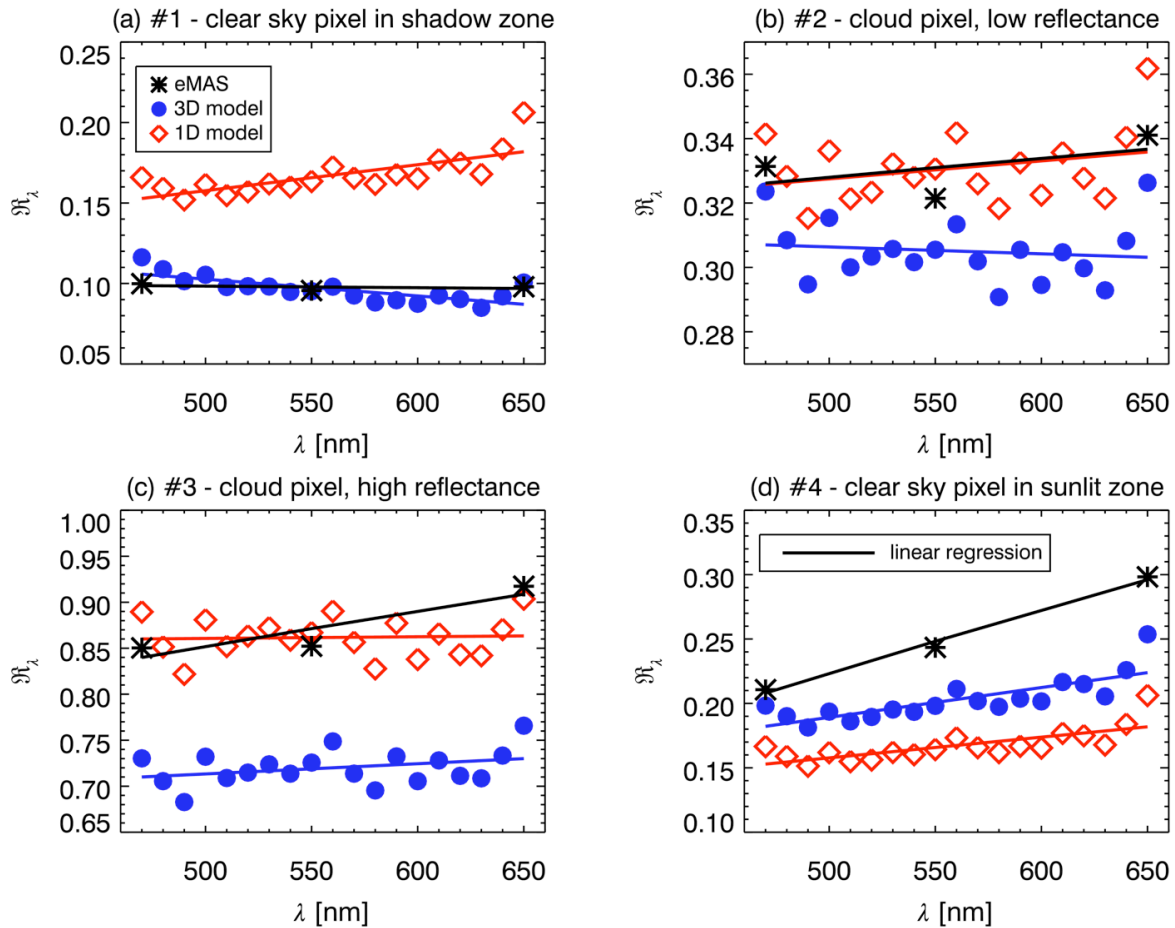


Figure 3.4: eMAS (black stars), 1D- (red diamonds) and 3D-modeled (blue dots) reflectance spectra (\mathfrak{R}_λ) as well as the linear regressions for the four pixels marked in Figure 3.3a.

For this cloud case, the reflectance was modeled at 10 nm intervals between 470 and 650 nm. The high sampling resolution adopted in the model reveals the spectral behavior resulting from gas absorption and variations in the scattering properties of cloud particles. These additional spectral features are not as obvious in the eMAS measurements because the eMAS spectral resolution is approximately 40-50 nm in this spectral region, significantly coarser than the 8 nm spectral resolution in the model calculations. In terms

of the reflectance magnitude, the 3D model reproduces the clear-sky pixels better than the 1D model; the opposite is true for cloudy pixels.

The spectral dependence of reflectance captured by the three eMAS channels can be approximated by the spectral slope, ζ_0 , at $\lambda_0=470$ nm obtained from a linear fit to \mathfrak{R}_λ : $\mathfrak{R}_{\lambda=470-650nm} \cong \zeta_0 \times (\lambda - \lambda_0) + \mathfrak{R}_0$. Figure 3.5a shows the relationship between \mathfrak{R}_0 and ζ_0 for nadir pixels of case 1. Error bars plotted next to the symbols denote the one-sigma variability estimates for ζ_0 averaged over all nadir pixels. Plotting the eMAS spectral reflectance in the \mathfrak{R}_0 - ζ_0 space reveals that the relationship between the magnitude of reflectance and its spectral slope can be understood in two distinct cloudy and clear-sky regimes. The cloudy regime consists of pixels with a wide range of reflectance magnitudes ($0 < \mathfrak{R}_0 < 1.2$) and extends horizontally in the \mathfrak{R}_0 - ζ_0 space. The clear-sky regime consists of low reflectance ($\mathfrak{R}_0 < 0.25$) pixels only and extends vertically in the \mathfrak{R}_0 - ζ_0 space. This double-branch feature is reproduced only in the 3D model, not the 1D model. In the 1D model, the vertical branch does not exist at all, and the orientation of the horizontal branch is noticeably different from that of the measurements and 3D model. The dashed rectangle around pixel #4 marks the sunlit zones that have been discussed in previous studies (*Marshak et al.* [2008]; *Wen et al.* [2008]; *Várnai and Marshak* [2009]).

For the measured and 3D-modeled horizontal branch of the \mathfrak{R}_0 - ζ_0 relationship, ζ_0 increases from negative to positive as \mathfrak{R}_0 increases. The 1D model results in the opposite: ζ_0 decreases from positive to negative as \mathfrak{R}_0 increases. With the information in the ζ_0 dimension, it is clear that even when the magnitude of 1D-modeled reflectance matches the measurements in cloudy regions, the 1D model gives statistically inaccurate spectral dependencies in the domain as a whole.

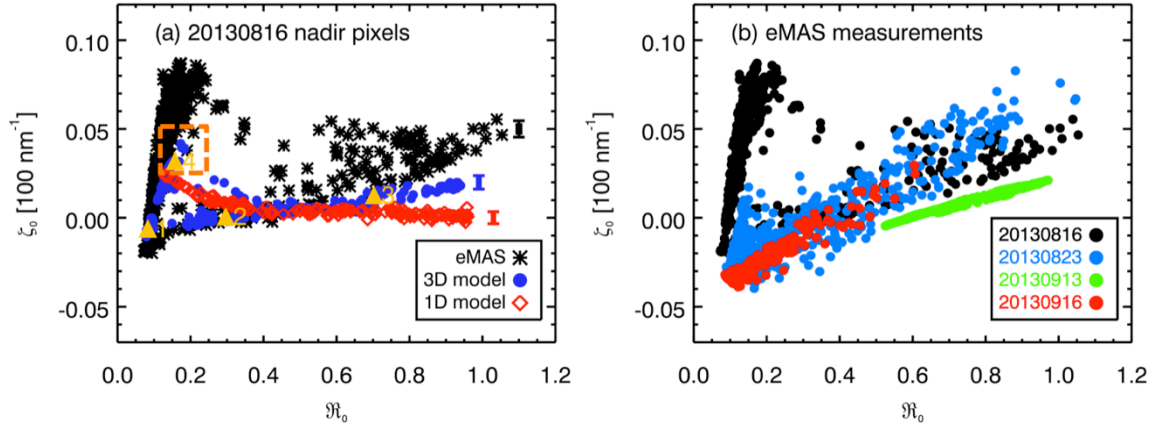


Figure 3.5: (a) The scattered plot of the measurement-derived (black), 1D- (red) and 3D-modeled (blue) reflectance at 470 nm (\mathfrak{R}_0) against spectral dependence (ζ_0) of reflectance for nadir pixels of case 1 (2013/08/16). The four pixels marked in Figure 3.2a are represented by their 3D-modeled \mathfrak{R}_0 - ζ_0 pairs. (b) Measurement-derived \mathfrak{R}_0 - ζ_0 relationships for all cases (nadir observations only).

In the vertical branch, both the measurements and the 3D model show that as \mathfrak{R}_0 increases, i.e., moving from shadow to sunlit regions, ζ_0 increases from negative to positive. Since there is no shadow or sunlit zone in the 1D model, this feature does not exist at all. The range of ζ_0 in the vertical branch is primarily determined by the magnitude and spectral shape of surface albedo, based on evidence from additional model calculations (not shown here, but discussed in detail in §3.B.1). Since the actual surface albedo varies along the flight track, the 3D model does not recover the full range of ζ_0 in the measurements because it assumes a spatially homogeneous surface albedo.

Figure 3.5b illustrates that similar relationships between the reflectance and its spectral shape are obtained for a range of cases. The shape of the horizontal branch is consistent across all cases, somewhat surprisingly considering the wide range of cloud types, cloud height, and surface conditions in these cases. Case 3 (9/13/2013) was overcast, and thus there was no pixel with reflectance lower than 0.5. Also, the orientation of the horizontal branch in this case is slightly different from the others. This is due to differences

in cloud microphysics because it is the only ice cloud case. The vertical branch appears in the two cases over land, case 1 (8/16/2013) and case 2 (8/23/2013). The surface albedo of the former case was higher and had a larger positive spectral slope in the spectral range from 470 to 650 nm (Figure 1.5). Thus the magnitude of ζ_0 in the former case is generally larger and spans a wider range than in the latter. For all cases, the 3D model reproduces the general features of the eMAS-derived \mathfrak{R}_0 - ζ_0 relationship, in contrast to the 1D model, which gives a distinctively different relationship. Additional analysis is presented in Figure 3.11 in §3.B.1 for the measurement-model comparison of case 2, with similar findings for the horizontal branch. The results for the vertical branch, however, are distinctly different to the ones from case 1.

3.5 Spectral signature of 3D cloud effects in irradiance observations

The initial motivation behind the study presented in the previous section was the discovery of the domain-wide H_0 - S_0 relationship in the irradiance field of heterogeneous clouds from a recent modeling study by *Song et al.* [2016a]. In this section, we present the first observational evidence of this H_0 - S_0 relationship using irradiance measurements.

Figure 3.6a shows a consistent correlation between the SSFR-derived H_0 and S_0 for pixels along the collocated flight track of case 1. The general shape of this H_0 - S_0 relationship is reproduced by the 3D model. Figure 3.6b, which shows the SSFR-derived H_0 - S_0 relationships for three cases, illustrates that the H_0 - S_0 relationship is a general phenomenon in radiation fields for a wide range of heterogeneous cloud scenes. The red dashed arrow in Figure 3.6a shows an example of deriving the effective ε from the slope of the regression line of S_0 versus H_0 for all pixels of case 1. The value is 0.09. The ε value derived from Figure 3.6b is 0.13 and 0.03 for cases 2 and 3, respectively. Thus ε does vary

from case to case. Its dependence on scene parameters such as solar zenith angle, cloud height, and surface albedo is investigated in §4.1. However, more studies are needed to understand how and why certain physical and optical parameters modulate ε .

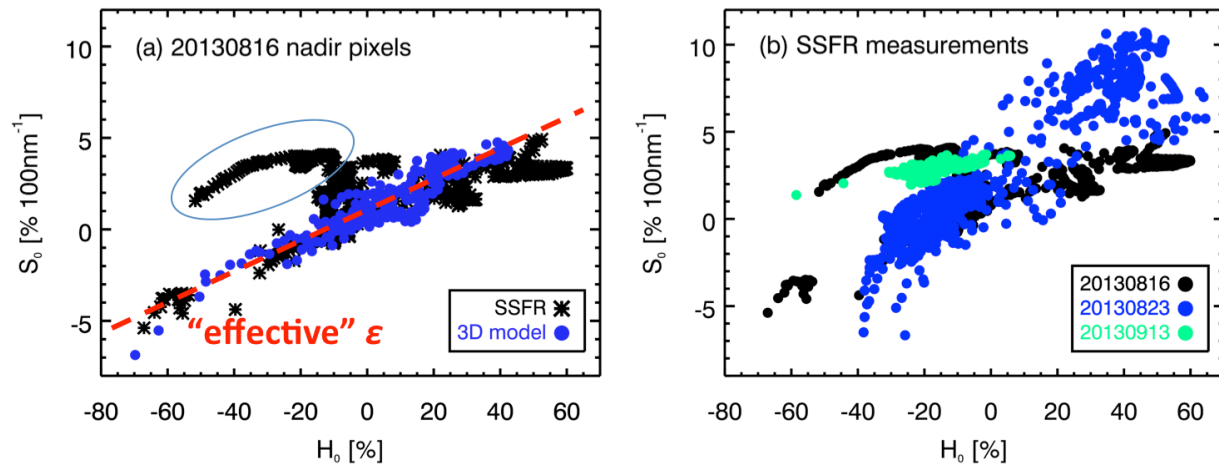


Figure 3.6: (a) Measurement-derived (black) and 3D-modeled (blue) H_0 – S_0 relationships for nadir pixels of case 1. (b) Measurement-derived H_0 – S_0 relationships for the three cases with collocated SSFR observations.

For certain cloud scenes, more than one ε may be required to describe the spectral signature of 3D cloud effects in irradiances. For case 1, the H_0 – S_0 pairs for some pixels (highlighted by the blue oval) do not follow the predominant behavior. These pixels are located between 109.25°W and 109.55°W. A probable explanation is that the SSFR measurements from either the ER-2 or DC-8, or both, were influenced by clouds outside the eMAS swath, which consequently affected H of these pixels. In addition, for pixels that have the largest H_0 (net radiation donors), their H_0 – S_0 relationship is offset with respect to the overall relationship. For this cloud case, the H_0 – S_0 relationship of net radiation donor pixels is slightly different from that of recipients. Another example of this phenomenon can be

seen from the 3D-modeled results of case 2 (Figure 3.11d in §3.B.1 and Figure 3.12b in §3.B.2).

3.6 Connecting the spectral signature of 3D cloud effects in radiances and irradiances

In this section, we explore whether the spectral signatures of 3D cloud effects in radiance (§3.4) and irradiance (§3.5) are related, and if so, whether the relationship can be established at the pixel level or through the pixel population within a domain (SQ2). Having validated the calculations with observations in the previous two sections, we only rely on model results in this sub-section. Figure 3.7 replicates the radiance and irradiance plots from Figure 3.5a and Figure 3.6, respectively, but includes all pixels in the domain (rather than nadir only). In the top row, the color for an individual pixel is defined according to reflectance bins. This allows to map (a) \mathfrak{R}_0 - ζ_0 to (b) H_0 - S_0 (b) space. As \mathfrak{R}_0 increases, H_0 clusters at positive values around 15%, which means that cloudy pixels with the highest optical thicknesses act primarily as net radiation donors. However, high-reflectance pixels (red) do not translate into maximum values for H_0 . Rather, the maximum range in H_0 is established by the collection of low-reflectance pixels (black). In other words, H is not solely governed by local cloud optical thickness, but depends on spatial *gradients* in cloud distribution. In this particular case, pixels with high optical thickness are mainly located close to the cloud center. The optical thickness contrast to the neighboring pixels is low, which results in a low or moderate H . By contrast, a cloudy pixel of relatively low optical thickness is more likely to be surrounded by clear-sky pixels. In these regions of the domain, the contrasts are more conducive to net horizontal photon transport away from and

towards a pixel. Collectively, the pixels with low reflectance act as net radiation recipients ($H<0$), balancing the high-reflectance pixels ($H>0$).

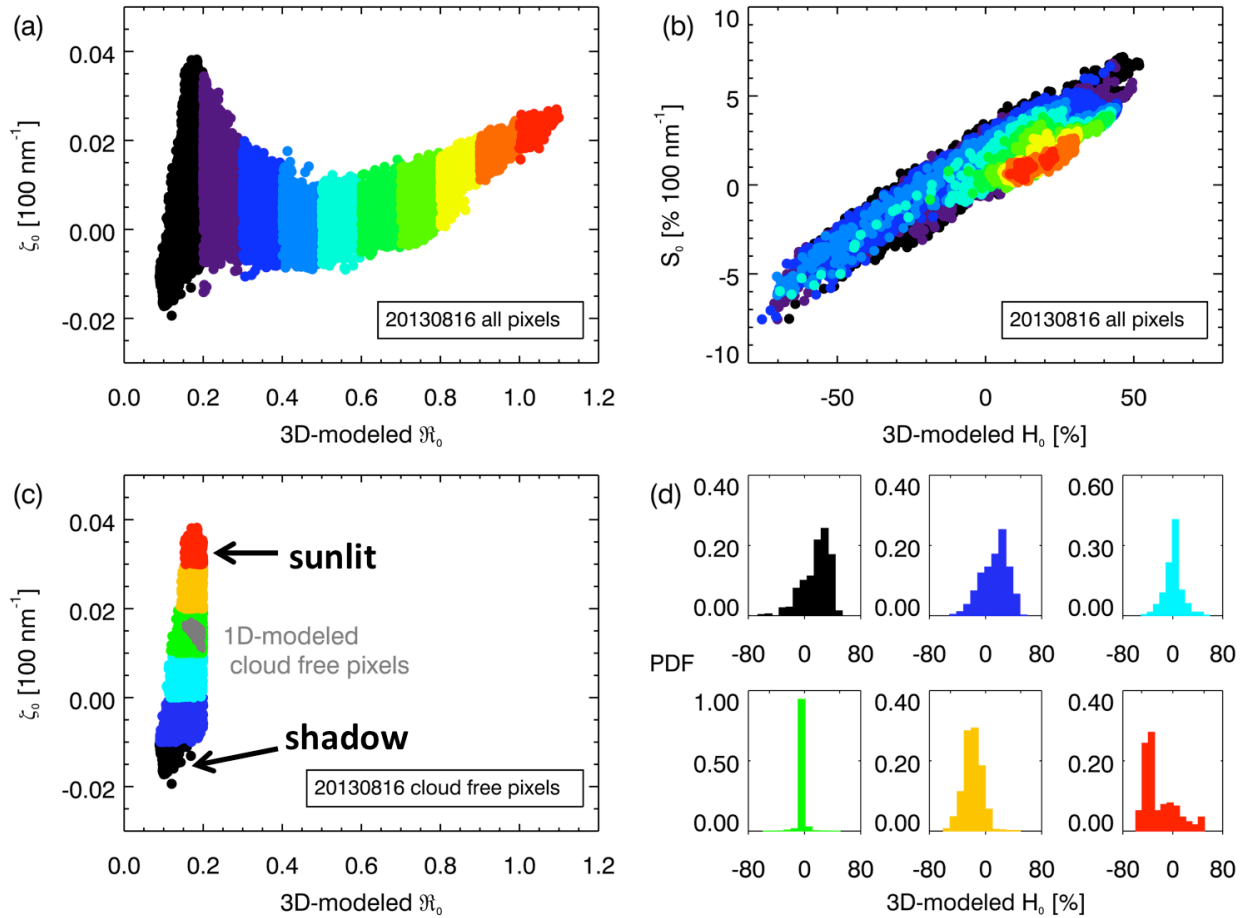


Figure 3.7: (a) 3D-modeled \mathfrak{R}_0 – ζ_0 relationships for all pixels of case 1; (b) 3D-modeled H_0 – S_0 relationships for pixels of the same colors in (a); (c) 3D-modeled \mathfrak{R}_0 – ζ_0 relationship for low reflectance pixels ($\mathfrak{R}_0 < \sim 0.2$); (d) Histograms of H_0 for pixels of the same colors in (c). The mean H_0 of the distributions from top-left to bottom-right are +17.1%, +13.1%, +0.43%, –0.91%, –18.4%, and –22.7%.

In this case, pixels with \mathfrak{R}_0 lower than 0.2 correspond to H_0 from –80% to +60%. Because this range is largest for these low-reflectance pixels, we now turn to the question whether the ζ_0 dimension constrains H_0 for these pixels. The two bottom panels share the

same color code to map changes in ζ_0 to H_0 . They illustrate the change in the probability distribution of H_0 as one moves from clear-sky pixels with negative ζ_0 (clear-sky bluing in shadows) to those with positive ζ_0 (clear-sky reddening in sun-lit zone) along the vertical branch. Note that the specific values for ζ_0 are scene-dependent; for case 2 (discussed in §3.B.2), negative ζ_0 correspond to sun-lit pixels (clear-sky bluing instead of reddening). For reference, the 1D calculations are overlaid on the 3D results in Figure 3.7c (gray). Interpreting the 3D-modeled results in the context of this reference, pixels with black or bluish colors are in shadows, and pixels with red or orange colors are zones with enhanced reflectance (“sun-lit”). As one moves from shadow to sunlit zones, the probability distribution of H_0 (Figure 3.7d) shifts from positive to negative values. These results suggest that clear-sky pixels in cloud shadows ($\zeta_0^{3D} < \zeta_0^{1D}$) collectively act as net radiation donors, although this connection cannot be made on the basis of individual pixels due to the spread in the H_0 histogram. The opposite is true for sun-lit pixels. These results make sense since the zones of enhanced 3D reflectance are net recipients of radiation ($H_0 < 0$). For shadow pixels, it is perhaps not immediately obvious that they should be dominated by positive H_0 values. It can be understood when considering that in terms of horizontal photon transport, shadow pixels are actually expected to behave similarly to cloudy pixels, which collectively act as photon radiation donors.

Although the results presented for case 2 (§3.B.2, Figure 3.12) differ in terms of the sign of ζ_0 , their results are qualitatively consistent in that the range of ζ_0 can be mapped to histograms of H_0 . The difference in terms of the sign of ζ_0 is due the spectral dependence of the surface albedo between 470 and 650 nm. It is important to point out that the non-shadow clear-sky pixels in the vicinity of clouds are subject to clear-sky *reddening* by comparison to the 1D baseline (i.e., $\zeta_0^{3D} < \zeta_0^{1D}$) for case 1, which is in contrast to earlier

studies (e.g., *Várnai and Marshak* [2009]). Case 2, on the other hand (§3.B.2), is consistent with earlier findings ($\zeta_0^{3D} > \zeta_0^{1D}$, i.e., bluing in these zones).

3.7 Radiation closure in transmitted irradiances

In this section, we consider the radiation closure in terms of the transmitted irradiance as measured by SSFR vs. the modeled counterpart from remote sensing (mainly eMAS retrievals in conjunction with 3D calculations). In addition to case 1 (discussed here), §3.B.3 examines case 2. In order to interpret discrepancies between measurements and calculations, we determine remote sensing and irradiance bias separately as described in §1.1.

Figure 3.8a shows the 3D-modeled transmitted irradiance field at 470 nm ($F^{\downarrow,470\text{ nm}}$) at the DC-8 altitude (~2 km), along with SSFR measurements along the DC-8 flight track. In locations where the color-coded measurement stands out against the contour plot (most obvious near 22 km), a measurement-model discrepancy occurs. As a quantitative assessment, Figure 3.8b shows the cross section along the flight track (plotted as function of latitude). SSFR measured lower transmitted irradiances below cell #1 than below cell #2 although the eMAS retrieval indicates that the former is generally optically thinner than the latter. This is because the 3D effects are much more prominent for cell #1 than for cell #2, where the discrepancy is negligible in most places. Indeed, §3.A shows that eMAS retrievals of optical thickness are collectively biased low for cell #1. Locations with poor agreement between the model and the measurements (for example at -109° latitude or 22km) are mainly near cloud edges where small misplacements of the cloud boundary in the model have a large effect on the modeled irradiance.

Aside from these outliers, the difference between the measurements (black) and 3D model results (blue) is generally due to the remote sensing bias as described in §3.1. The 1D calculations (red) fail to reproduce the measurement in clear-sky and cloudy regions, and are included here to visualize the irradiance bias (§3.1) the difference between the 1D and 3D calculations) caused by the 3D effects on irradiance rather than retrievals.

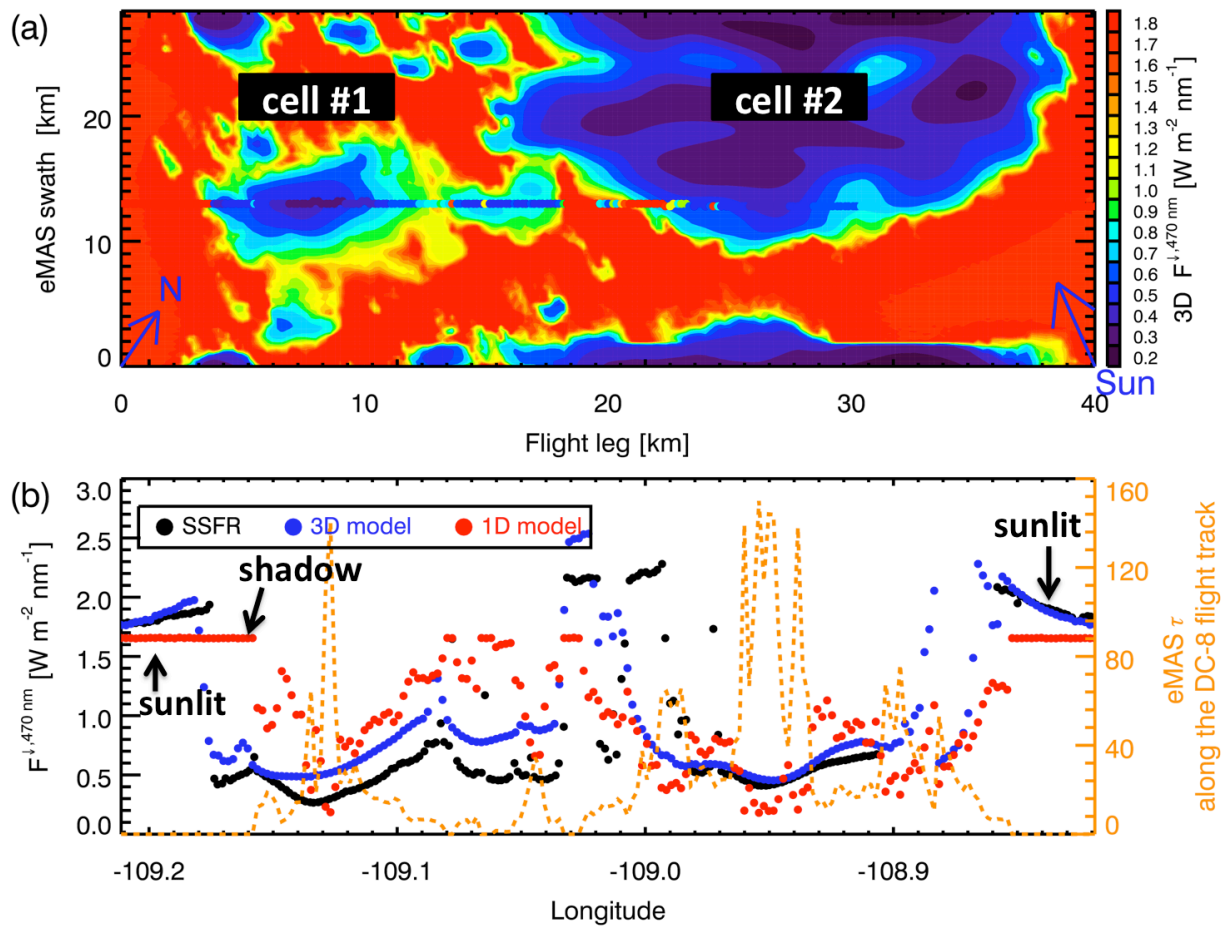


Figure 3.8: (a) 3D-modeled transmitted irradiance of case 1 at 470 nm ($F^{\downarrow,470\text{nm}}$) at the DC-8 altitude, over-plotted with the SSFR-measured $F^{\downarrow,470\text{nm}}$ along the DC-8 flight track using the same color code; (b) Comparison of the measured (black) and 1D- (red) and 3D-modeled (blue) $F^{\downarrow,470\text{nm}}$ along the flight track.

To attribute the discrepancy to these two biases on a more statistically meaningful basis, we sub-sampled pixels for cell #1 and #2 and assigned the measured and modeled spectra to the “cloudy” and “clear-sky” category using $F_{\lambda}^{\downarrow,470\text{ nm}} = 0.9\text{ Wm}^{-2}\text{ nm}^{-1}$ as threshold.

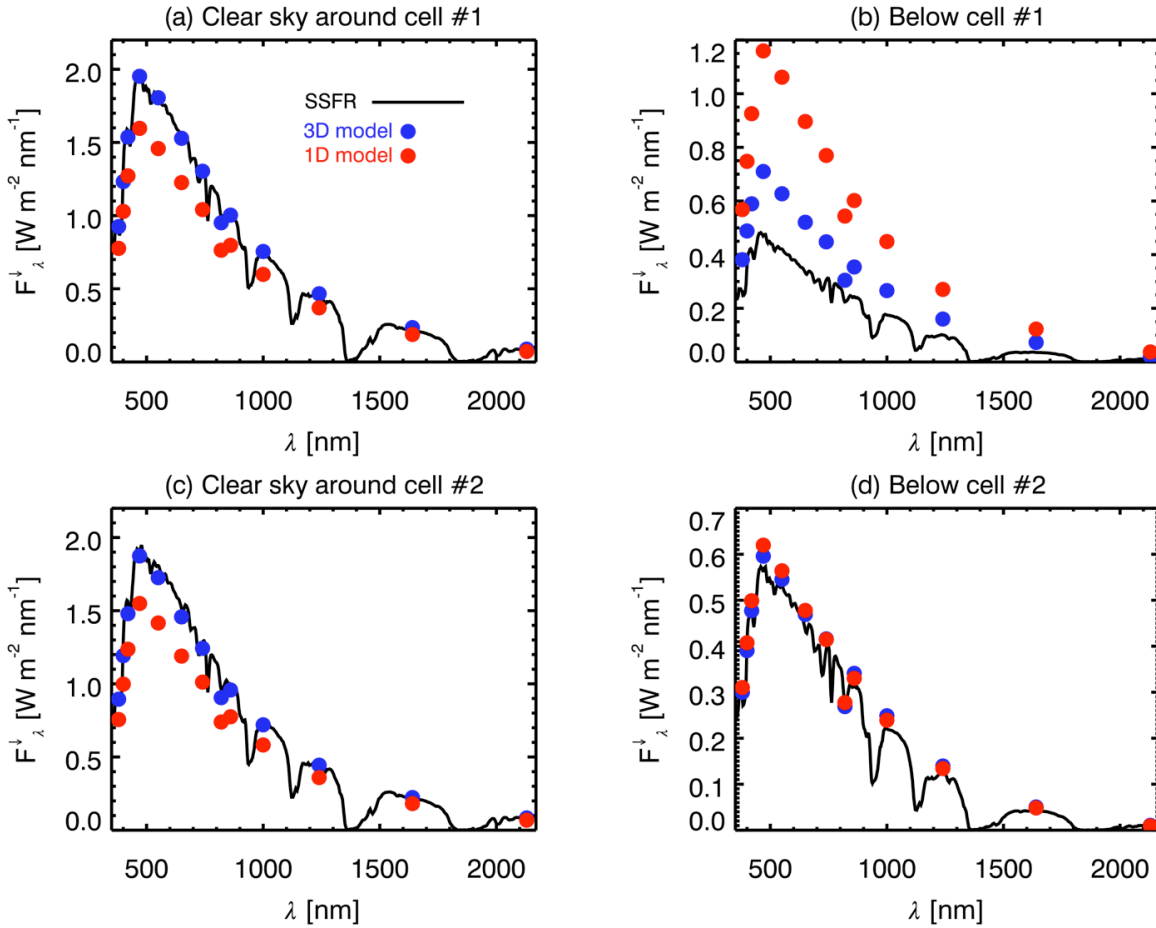


Figure 3.9: Measured (black line), 1D- (red dots) and 3D-modeled (blue dots) downward irradiance spectra ($\overline{F_{\lambda}^{\downarrow}}$) averaged over (a) clear sky pixels around cell #1; (b) cloudy pixels below cell #1; (c) clear sky pixels around cell #2; and (d) cloudy pixels below cell #2.

Figure 3.9 (left column) presents the averaged downward irradiance spectra for the pixels in the clear-sky category around the two cells (#1: top, #2: bottom). In contrast to the 1D calculations, which underestimate the downwelling radiation over the spectral range by

14%-22%, the 3D calculations are in agreement with the measurements to within the SSFR measurement uncertainty ($\pm 5\%$). We conclude that for clear-sky regions, the dominating source of error in the radiation closure is the *irradiance bias*, and that the cloud remote sensing bias is negligible.

For cloudy regions below cell #1 (Figure 3.9b), the 1D-modeled downward irradiances are more than twice as high as the measurements. Even after eliminating the irradiance bias by performing 3D radiative transfer calculations, the 3D-modeled downward irradiances are still 50% higher than the measurements. This 50% difference is well beyond the maximum measurement-model uncertainties and points to a discrepancy between the modeled cloud field and the truth. In contrast to the clear-sky region, the remote sensing bias (difference between 3D calculations and measurements) does contribute considerably to the total 3D bias. In this case, the remote sensing and irradiance biases are similar in magnitude (about 50% each). For cell #2, neither remote sensing nor irradiance bias is significant for reasons outlined in §3.A.

It should be noted that the 3D effect illustrated in Figure 3.9b is not an isolated extreme case. Section §3.B.3 presents the results of the same analysis for case 2 with a different cloud type, spatial distribution, cloud height, and surface albedo. Figure 3.13d shows that after eliminating the irradiance bias, the 3D-modeled downward irradiances are still 40% higher than the measurements, which is qualitatively similar to the result in Figure 3.9b.

3.8 Summary and conclusions

In this chapter, we used the SEAC⁴RS dataset to provide observational evidence for the connection between cloud inhomogeneity and spectral perturbations in irradiance and

radiance fields (SQ1 in §3.1). Using SSFR irradiance measurements on collocated aircraft above and below various cloud fields, we confirmed the correlation between the magnitude of net horizontal photon transport (H_0) and its spectral dependence in the mid-visible (S_0) that had been predicted on the basis of remote sensing observations during the TC⁴ experiment by *Song et al.* [2016a]. To test the hypothesis that cloud spatial structure also leaves systematic spectral imprints on radiances, we used eMAS observations for the same cases. While “clear-sky bluing” of radiances in the vicinity had been previously reported on the basis of satellite observations of clear-sky pixels, this work generalized the earlier studies to all pixels in a domain. As radiance counterparts to H_0 and S_0 , we chose the reflectance in the visible wavelength range \mathfrak{R}_0 and its spectral dependence ζ_0 . The calculations, based on the imagery from eMAS, showed that the \mathfrak{R}_0 - ζ_0 relationship for the population of pixels in the domain is distinctly different when enabling or disabling 3D radiative transfer in the model, and that only the 3D calculations reproduce the measurements in this regard. Two different pixel groups constituted “branches” in the \mathfrak{R}_0 - ζ_0 plots, which suggested that 3D cloud effects in radiances manifest themselves differently in cloudy (horizontal branch) and clear-sky (vertical branch) areas.

The clear-sky (vertical) branch of the \mathfrak{R}_0 - ζ_0 relationship can be put in context with earlier findings, e.g., *Várnai and Marshak*, [2009]. In contrast to these studies, we found clear-sky bluing as well as reddening in the vicinity of clouds. This was traced back to the spectral dependence of the surface albedo for different cases. Since earlier studies were primarily based on cases over ocean, this might explain why they only found bluing [*Várnai*, personal communication]. To our knowledge, the cloudy (horizontal) branch had previously not been considered in the context of spectral 3D effects. The relationship between the reflectance and its spectral dependence on this branch is surprisingly similar

for the considered cases. In each of those, only 3D calculations reproduced the measurements. The small differences are due to microphysics, and possibly other scene parameters.

Once we confirmed that the spectral signature of 3D cloud effects is detectable from measured radiances and irradiances, we investigated whether there is a connection between the two (SQ #2). We were able to demonstrate a mapping from the \mathfrak{R}_0 - ζ_0 space to the H_0 - S_0 space and showed that such a radiance-irradiance connection can only be established in terms of pixel populations rather than for individual pixels. The relationship is different for cloudy and clear-sky pixels (horizontal and vertical branch in \mathfrak{R}_0 - ζ_0 space). In the vertical branch, ζ_0 is correlated with H_0 , at least in the statistical sense. However, ζ_0 is also strongly affected by the surface albedo. Therefore, while future bias correction techniques might capitalize in the ζ_0 - H_0 connection, the dependence on specific scene parameters needs to be taken into consideration.

The final objective this chapter (SQ #3) was to study radiation closure in transmitted irradiances by comparing modeled and measured irradiance fields. Since our findings from the previous two science questions suggested that 3D cloud effects in radiances and irradiances manifest themselves differently in clear-sky and cloudy pixels, we assessed clear-sky and cloudy regions separately and found that for clear sky pixels the irradiance bias is the dominating factor. In other words, the mere presence of a cloud in the vicinity of a clear-sky pixel determines the irradiance field to a much greater extent than the properties of those clouds.

For cloudy pixels, on the other hand, the cloud properties themselves and the remote sensing bias associated with them accounted for about half of the total bias between calculations and model results, with the irradiance bias contributing the other half. The

total bias was close to 100% in one case. This was not an isolated occurrence, however, as one additional case showed. While SEAC⁴RS provided the basic data to contrast different cloud types and their impact on radiation fields, more measurements of similar quality would be desirable to give the findings higher statistical significance.

We acknowledge that cloud radiation studies are largely reliant on 1D calculations for the time being, which means that it would be desirable to incorporate 3D effects in a largely 1D retrieval framework. The correlations between spatial inhomogeneities and spectral perturbations might pave the way for such approaches. The results presented here should therefore be viewed as a starting point for developing corrections for 3D cloud effects based on their spectral signature. At the same time, the findings of this chapter evoke a number of new questions:

- (1) To first-order, can the \mathfrak{R}_0 - ζ_0 relationship be quantified using a similar parameter as the “effective” ε proposed by *Song et al.* [2016a]?
- (2) What modulates the \mathfrak{R}_0 - ζ_0 relationship? We proposed cloud microphysics as a dominating factor for the horizontal branch, as well as the magnitude and spectral shape of surface albedo for the vertical branch.
- (3) Are there other factors, such as solar zenith angle, azimuthal angle, and cloud cover?
- (4) Do remote sensing and irradiance biases always introduce comparable errors into the calculations of energy budget quantities? Are there cases where these biases partially compensate?
- (5) How are other key quantities, such as the upwelling irradiance above inhomogeneous cloud fields affected?

- (6) How can the \mathfrak{R}_0 - ζ_0 relationship be exploited to reduce the remote sensing bias in cloud retrievals and consequently in energy budget calculations?
- (7) How do the biases change in presence of an aerosol layer?

The answer to many of these questions may well lie in the spectral dimension, as well as in the combination of information from multiple pixels located in cloudy and clear-sky regions.

Acknowledgement:

This research was supported by NASA grant NNX14AP72G. The authors wish to thank Warren Gore and Antonio Trias of the NASA Ames Research Center for their support of SSFR during SEAC⁴RS, and Tom Arnold and Gala Wind of the NASA Goddard Research Center for their help with eMAS data. The modeling work was carried out with the Janus supercomputer, which is supported by the National Science Foundation (award number CNS-0821794) and the University of Colorado Boulder. The Janus supercomputer is a joint effort of the University of Colorado Boulder, the University of Colorado Denver, and the National Center for Atmospheric Research. Janus is operated by the University of Colorado Boulder.

3.A Approximating the remote sensing bias

In §3.7, we showed that for case 1, the 3D-modeled downward irradiances are 50% higher than the measurements even after eliminating the irradiance bias. In this section, we aim to estimate the eMAS retrieval bias in cloud optical thickness due to neglecting 3D cloud effects in the retrieval algorithm and investigate if the remaining discrepancy in

transmitted irradiances between the 3D model and measurements can be explained by the eMAS retrieval bias.

Figure 3.1 (§3.1) illustrates the approach of approximating the retrieval bias and the corresponding radiative effects in the form of cloud transmittance. The three major steps in this process are indicated, progressing from blue symbols (processes in nature) to orange (measurements and data processing) and then to green (radiative transfer modeling). To start, one does not know the true distribution of cloud optical properties because the observed radiances (in this case by eMAS) are already affected by 3D cloud effects such as the radiative smoothing and roughening within a cloud layer [Marshak *et al.*, 1995]. As a result, the retrieved optical thickness field (τ_{eMAS}) may be biased with respect to the truth (τ_{true}). Other cloud retrieval parameters such as effective radius (not discussed here) are similarly affected [Zhang *et al.*, 2010]. In absence of the true optical thickness field, we used the eMAS retrieval in model calculations to obtain the associated radiance and irradiance fields. On the radiance side, we used the 3D-modeled radiance field as synthetic cloud observations. We then retrieved τ_{Model} from the synthetic observations using 1D assumptions, which emulates how τ_{eMAS} was retrieved from the actual observation in the “ladder step” above. We obtained the synthetic retrieval bias $\Delta\tau_2 = \tau_{model} - \tau_{eMAS}$, and used it as a first-order proxy of the true retrieval bias $\Delta\tau_1$. The optical thickness bias was then translated into the associated transmittance bias that affects the irradiance field below clouds, ΔT .

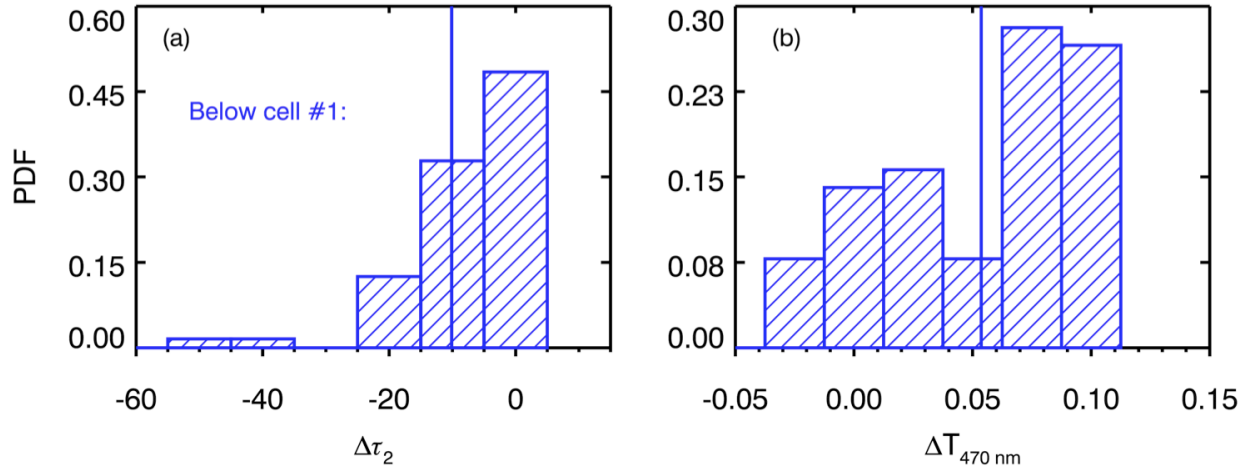


Figure 3.10: Probability distribution functions of (a) the retrieval bias in cloud optical thickness ($\Delta\tau_2$) due to remote sensing bias of 3D cloud effects; and (b) corresponding bias in cloud transmittance at 470 nm ($\Delta T_{470\text{ nm}}$) due to $\Delta\tau_2$; for pixels along the DC-8 flight track below cell #1 shown in Figure 3.8. The means in both quantities are indicated by the blue line.

For pixels along the DC-8 flight leg below cell #1, the distributions of $\Delta\tau_2$ and $\Delta T_{470\text{ nm}}$ are plotted in Figure 3.10. The majority of $\Delta\tau_2$ values is close to zero, but the average is $\overline{\Delta\tau_2} = -10.1$, which is a significant underestimation. It leads to a systematic overestimation in cloud transmittance. More than 80% of $\Delta T_{470\text{ nm}}$ is positive with an average of $\overline{\Delta T_{470\text{ nm}}} = 0.054$, which translates to $0.11 \text{ Wm}^{-2} \text{ nm}^{-1}$ in irradiance. Figure 3.9c shows that the discrepancy of transmitted irradiances at 470 nm is 0.24 Wm^{-2} between the 3D model and measurement. Therefore, $\overline{\Delta\tau_2} = -10.1$ in retrieval bias explains only 50% of the discrepancy between the 3D model calculations and the measurements at 470 nm. However, $\overline{\Delta\tau_2}$ is probably lower than the actual retrieval bias $\overline{\Delta\tau_1}$ because it is determined by way of synthetic observations that are smoother than the (unknown) true cloud optical thickness field. Other factors, such as the insufficiently known surface albedo might also contribute to the discrepancies in the downwelling irradiance below clouds.

3.B Supplementary results from case 2

In this appendix, results from case 2, observed on 2013/08/23 are provided to check the robustness of the findings from the body of the chapter.

3.B.1 Spectral signature of 3D cloud effects in radiances and irradiances

Figure 3.11a shows the eMAS-measured reflectance field at 470 nm (\mathfrak{R}_0) of case 2. In several respects, this cloud scene is significantly different from case 1 (Figure 3.3a): The horizontal cloud sizes are generally smaller (less than 10 km in diameter), and they are also shallower. The cross section of reflectance along the ER-2 flight track (Figure 3.11b) shows similar features as for case 1 (Figure 3.3b). The 1D model is in agreement with the measurements for cloudy pixels, whereas only the 3D model captures the enhanced and reduced reflectance near cloud edges. Due to the smaller scale of the clouds in case 2, it is less obvious from Figure 3.3b that the 1D calculations reproduce the measurements for cloudy pixels better than the 3D calculations – for the same reason as for case 1. For case 2, the cloud reflectance calculated the 3D model is even more affected by inhomogeneity, and is significantly lower than the measurements as a result. In clear sky regions far away from clouds, both 1D- and 3D-modeled reflectance are higher than the measurements, which suggests the surface albedo used as model input is unrealistically high.

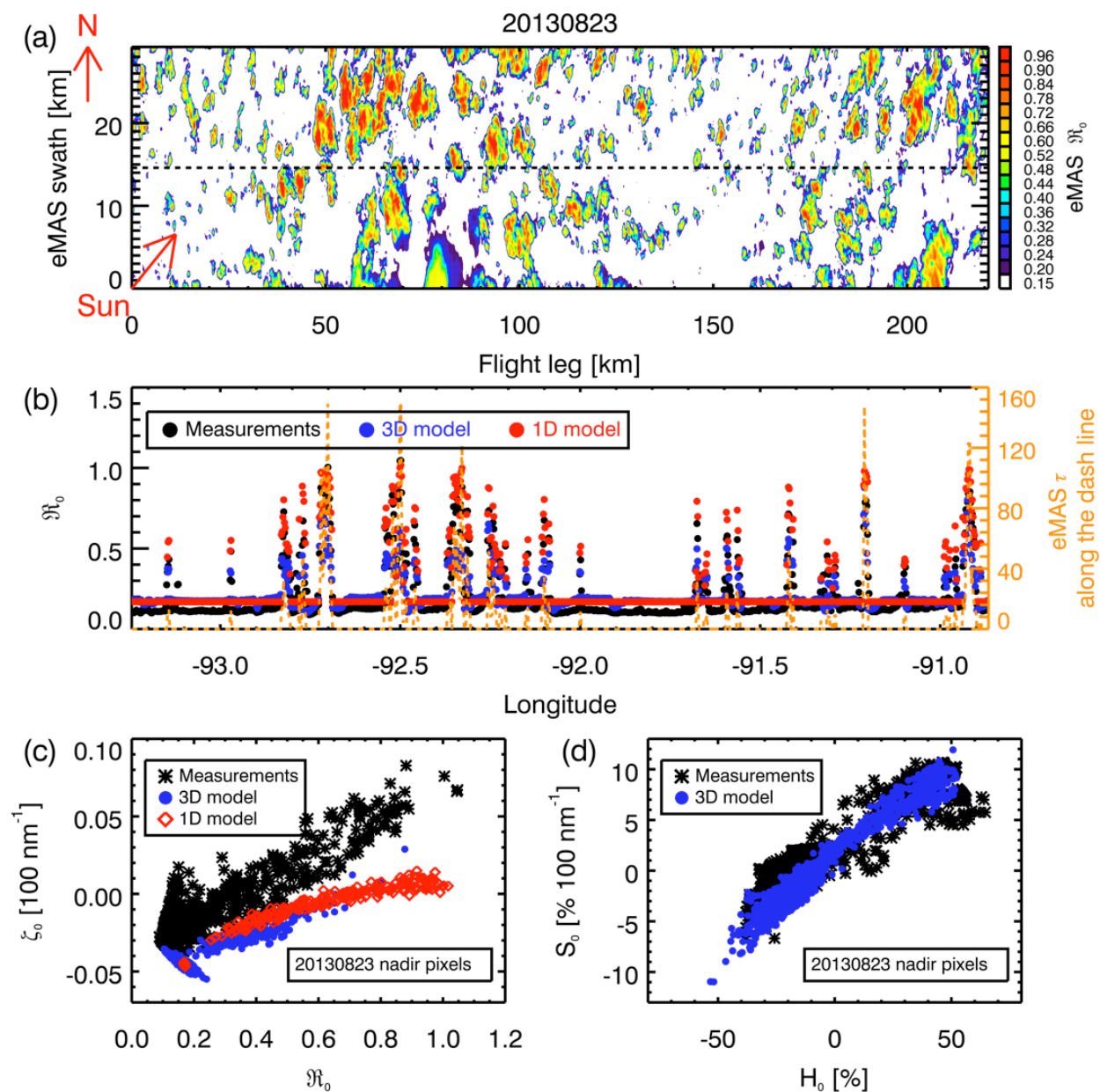


Figure 3.11: (a) The eMAS reflectance field at 470 nm (\mathfrak{R}_0) of case 2; (b) Comparison of the measured (black) and 1D- (red) and 3D-modeled (blue) \mathfrak{R}_0 along the nadir track, plotted together with the eMAS-retrieved cloud optical thickness; (c) The scatterplot of the measurement-derived (black stars), 1D- (red diamonds) and 3D-modeled (blue dots) \mathfrak{R}_0 against ζ_0 for nadir pixels; (d) The scatterplot of the measurement-derived (black stars) and 3D-modeled (blue dots) H_0 against S_0 for nadir pixels.

As discussed in Figure 3.5b, the measurement-derived \mathfrak{R}_0 - ζ_0 relationship of the nadir pixels (Figure 3.11c) consists of a horizontal and vertical branch. In the horizontal branch, \mathfrak{R}_0 increases along with ζ_0 . The 1D model reproduces the full range of \mathfrak{R}_0 as expected, but in contrast to the measurements, the \mathfrak{R}_0 - ζ_0 relationship becomes shallower with higher reflectance values. The 3D calculations, on the other hand, reproduce the correct behavior on the ζ_0 axis, even though the reflectance values are lower than measured (again as expected). This can be seen more clearly in Figure 3.12a, which shows the 3D-modeled \mathfrak{R}_0 - ζ_0 relationship for all pixels within the domain. The vertical branch in the measurements ($\mathfrak{R}_0 < 0.25$) is determined by the magnitude and spectral shape of the surface albedo along the flight leg. As indicated in the eMAS RGB imagery from the flight day (Figure 1.4), the geographical region consisted of forests with interspersed farmland. Because of this variability, the vertical branch could not be captured by one single spectral surface albedo in the radiative transfer model. The lower part (decreasing ζ_0 with increasing \mathfrak{R}_0) was reproduced using a forest albedo (the majority of the scene). The upper part (increasing ζ_0 with increasing \mathfrak{R}_0) seems to dominate the branch as a whole, but really only stems from a few pixels with farmland. This was confirmed with additional radiative transfer runs (not shown).

Finally, Figure 3.11d shows that the H_0 - S_0 relationship at nadir pixels as derived from SSFR measurements and 3D model are largely in agreement, with a few outliers in cases where the DC-8 was not perfectly collocated underneath the ER-2.

3.B.2 Connecting the spectral signature of 3D cloud effects in radiances and irradiances

For case 2, Figure 3.12 presents a similar analysis as Figure 3.7 for case 1. The top two panels show that as \mathfrak{R}_0 increases, H_0 increasingly cluster around 45%. These results are qualitatively consistent with the findings from case 1. However for case 2, H_0 converges to a higher value (45%) than for case 2 (15%). The 3D effects are stronger for case 2 due to the smaller cloud sizes and thus steeper horizontal gradients in optical thickness.

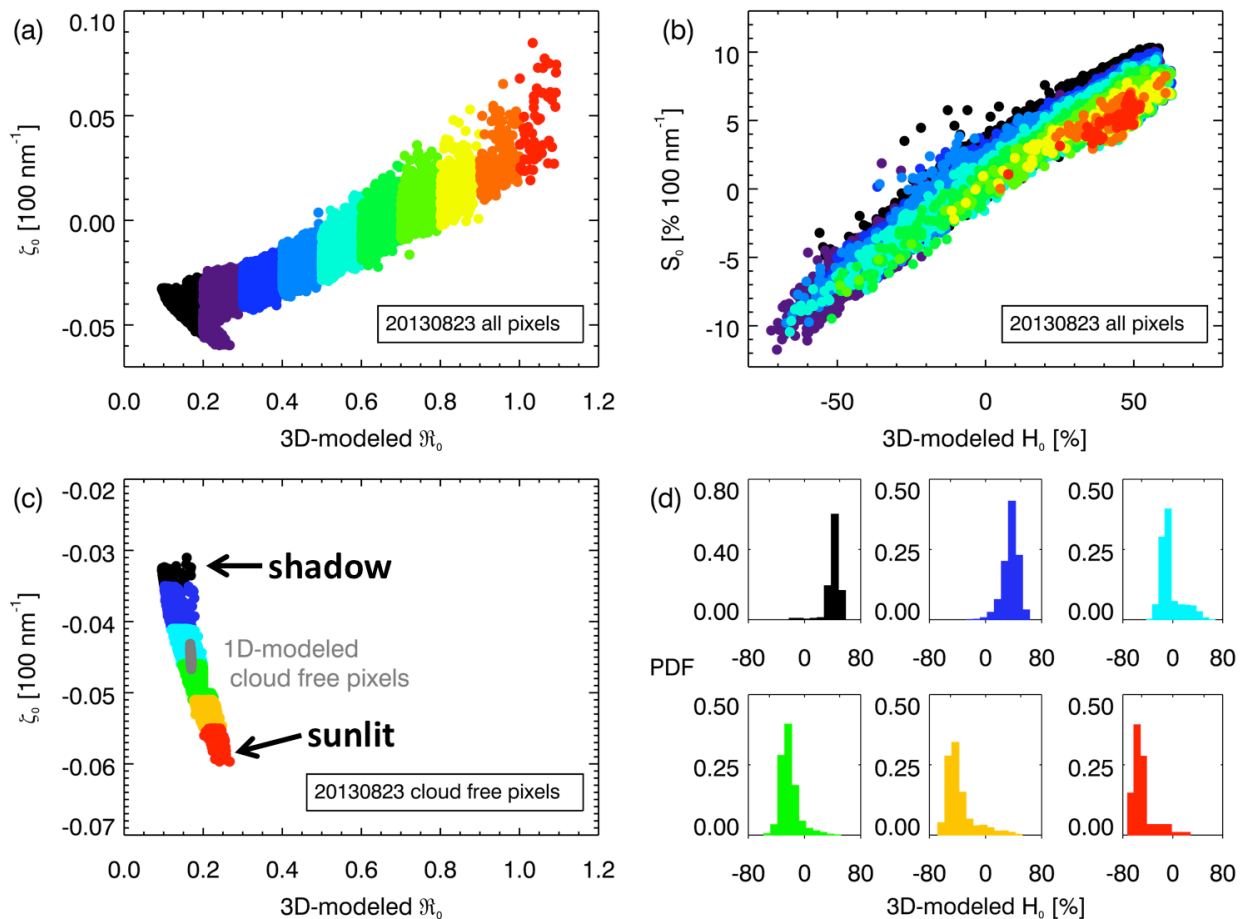


Figure 3.12: (a) 3D-modeled \mathfrak{R}_0 – ξ_0 relationships for all pixels of case 2; (b) 3D-modeled H_0 – S_0 relationships for pixels of the same colors in (a); (c) 3D-modeled \mathfrak{R}_0 – ξ_0 relationship for low reflectance pixels ($\mathfrak{R}_0 < \sim 0.2$); (d) Histograms of H_0 for pixels of the same colors in (c).

Pixels with \mathfrak{R}_0 lower than 0.8 are associated with H_0 values spanning -70% to 70% . The range in ζ_0 at any given reflectance could be used to constrain H_0 . This is illustrated with the lowest reflectance bin in Figure 3.12c and Figure 3.12d. Shadow pixels (cold colors) are primarily radiation donors, whereas sunlit pixels (warm colors) are primarily radiation recipients. This is consistent with our findings from the case 1, except that shadow pixels there have minimum ζ_0 values, and sunlit pixels maximum ζ_0 values – the opposite to case 2. This is due to the different spectral behavior of the surface albedo between 470 and 650 nm (Figure 1.5).

3.B.3 Radiation closure in transmitted irradiances

Figure 3.13a shows the 3D-modeled downward irradiance field at 470 nm (F_{470nm}^\downarrow) at DC-8 flight level ($\sim 2\text{km}$), over-plotted with SSFR measurements along the flight track using the same color code. Figure 3.13b shows a quantitative comparison of measured and modeled downward irradiance along the DC-8 flight track. The 3D model captures the cloud edge effects fairly well, although it overestimates radiation enhancements in some places. One reason for this small discrepancy could be the vertical distribution of the input cloud, which is not captured by the imagery.

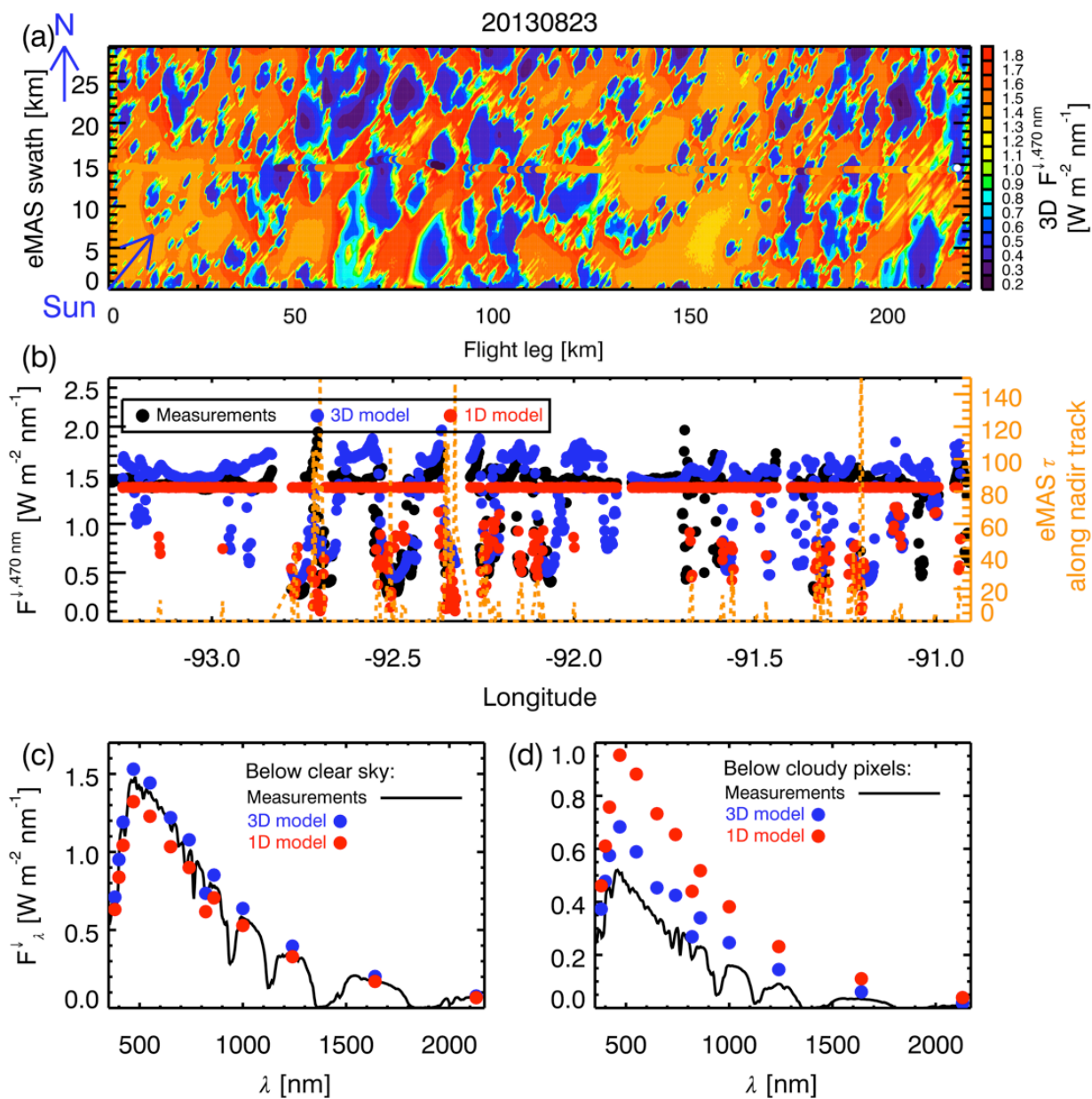


Figure 3.13: (a) 3D-modeled downward irradiance of case 2 at 470 nm ($F_{\downarrow, 470 \text{ nm}}^{\downarrow}$) below clouds at the DC-8 altitude, over-plotted with SSFR-measured downward irradiances along the flight track using the same color code; (b) Comparison of the measured (black) and 1D- (red) and 3D-modeled (blue) $F_{\downarrow, 470 \text{ nm}}^{\downarrow}$ along the flight track; (c) Measured (black line), 1D- (red dots) and 3D-modeled (blue dots) downward irradiance spectra (F_{λ}^{\downarrow}) averaged over clear sky pixels; (d) same as (c) but for cloudy pixels.

The bottom two panels of Figure 3.13 compare the average spectra of measured and modeled downward irradiance ($\overline{F_{\lambda}^{\downarrow}}$) at clear-sky and cloudy pixels along the DC-8 flight track. We followed the same methodology as used in Figure 3.9 to subsample pixels into “clear-sky” and “cloudy” categories. Similarly to the results of cell #1 in case 1, the clear-sky pixels are only affected by the irradiance bias. For cloudy pixels, however, the irradiance bias and remote sensing bias have comparable impacts on the calculated cloud transmittance. The 1D-modeled transmitted irradiance is almost twice as high as the measured. Even after removing the irradiance bias, the 3D-modeled transmitted irradiance is still 40% higher than measured (remote sensing bias).

We applied the approach introduced in §3.A to this case and estimated the retrieval bias in eMAS cloud optical thickness ($\Delta\tau_2$) and the corresponding bias in transmittance (ΔT_{470nm}). We found that, on average, eMAS cloud optical thickness retrieval is biasedly low by 13.4, which corresponds to a high bias in cloud transmittance of +0.073 and translates to +0.11 $\text{Wm}^{-2} \text{nm}^{-1}$ at 470 nm. This explains more than 60% of the observed remote sensing bias (discrepancy between 3D model and measurements, +0.18 $\text{Wm}^{-2} \text{nm}^{-1}$).

Chapter 4

Net horizontal photon transport: dependence on scene parameters and applications in airborne and ground-based cloud radiation measurements

4.1 Physical and optical parameters that modulate net horizontal photon transport and its spectral dependence: modeling analysis

In Chapters 2 and 3, we showed that for a broad range of realistic heterogeneous cloud scenes with varying conditions of cloud, aerosol, and surface type, the magnitude of net horizontal photon transport (H) at a non-absorbing wavelength (H_0) is closely correlated with the spectral dependence (S_0) of H in the near-ultraviolet and visible wavelength range. We introduced ε in Chapter 2 to parameterize the domain-wide correlation between H and its spectral dependence [Eq. (2.10)] that can be viewed as a measure of 3D cloud effects in irradiance fields. Once obtained for a given cloud scene, ε can be applied to infer the magnitude of H from its spectral dependency and vice versa, both for the scene as a whole and for individual pixels. In Chapter 3, we showed that ε varies, to different extent, from cloud scene to cloud scene (Figure 3.6b). Although ε can be potentially powerful to simplify the relationship between spatial structure and horizontal photon transport, it is also important to address the question how ε depends on domain scene

characteristics such as cloud optical thickness, cloud geometric height, depth, and horizontal extent, solar zenith angle, and surface albedo (magnitude and spectral dependence). For a certain constellation of these characteristics, one single ε value per scene may not adequately capture the relationship between horizontal photon transport and its spectral dependence. Extending the analysis from Chapter 2 to more cloud fields with a range of scene characteristics helps understanding conservative scattering in heterogeneous atmospheres at a more fundamental level.

The first step in this work is to find the dominating physical and optical modulators for ε . The focus in this section is thus to discuss “what” drives ε , which lays a solid foundation for future investigations on “why” as the next step. We designed four groups of radiative transfer experiments to study the dependence on four scene characteristics: cloud optical thickness (P1), surface albedo (P2), solar zenith angle (P3), and cloud geometric height (P4). Based on our findings from Chapters 2 and 3, these were a few key parameters that we expected to have strong impacts on ε .

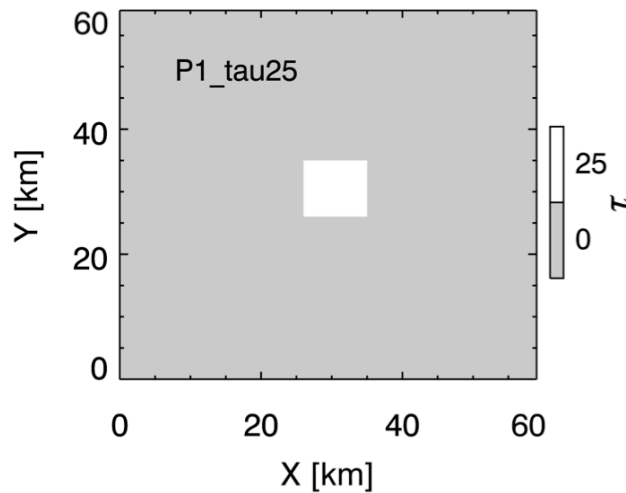


Figure 4.1: A single isolated cloud (optical thickness 25) surrounded by clear sky.

All experiments were based on a simple (idealized) cloud: the “single isolated cloud surrounded by clear skies” as shown in Figure 4.1¹⁴. The domain size was 60 km × 60 km, and the cloud size was 10 km × 10 km. The Sun was to the west of the cloud (solar azimuth angle 270°). More details of the experiments are given in Table 4.1.

Table 4.1: Details for experiments P1-P4 as discussed in §4.1, labeled by main variable under consideration.

Label/ Variable	Experiment	Cloud optical thickness	SZA	Cloud height	Vertical bracket to calculate H	Surface albedo
P1. Cloud optical thickness	P1_tau8	8	0°	1-3 km	1-4 km	0.0
	P1_tau15	15				
	P1_tau25	25				
	P1_tau50	50				
P2. Surface albedo	P2_alb0	25	0°	1-3 km	1-4 km	0.0 ¹⁵
	P2_alb0.3					0.3
	P2_alb0.5					0.5
	P2_alb_linear					see note ¹⁶
P3. Solar zenith angle	P3_sza0	25	0°	1-3 km	1-4 km	0.0
	P3_sza30		30°			
	P3_sza60		60°			
P4. Cloud height	P4_cld1_3km	25	0°	1-3 km	1-4 km	0.0
	P4_cld4_6km			4-6 km	4-7 km	
	P4_cld7_9km			7-9 km	7-10 km	

For the P1, P2, and P3 experiments, the cloud extended from 1 to 3 km and was vertically homogeneous. For the three P4 experiments, the cloud vertical location was 1-3 km, 4-6 km, and 7-9 km, respectively. The cloud thermodynamic phase was liquid, and the

¹⁴ More than one cloud geometry was studied, but only the most impactful scene characteristics are included here.

¹⁵ The surface albedo of “P2_alb0”, “P2_alb0.3” and “P2_alb0.5” experiments is prescribed as spectrally invariant value of 0.0, 0.3 and 0.5, respectively.

¹⁶ The surface albedo of “P2_alb_linear” experiment linearly increases from 0.0 to 0.27 from 350 to 800 nm, which is roughly representative of the surface type of dry grass (Figure 1.5).

effective radius of cloud droplets was fixed at $10 \mu\text{m}$. Single scattering albedo and asymmetry parameter were obtained from Mie calculations. For simplicity, the scattering was implemented as Henyey-Greenstein (HG) phase function in the model. As shown in §1.4.3, the HG phase function is sufficient for irradiance calculations of liquid water clouds. For the underlying surface, all experiments used a spectrally constant surface albedo with the exception of “P2_alb_linear” (see details in Table 4.1). Three-dimensional radiative transfer calculations were performed with MCARaTS at 10 wavelengths (350, 400, 450, 500, 550, 600, 650, 700, 750, and 800 nm), using 10^{11} photons each.

The magnitudes of net horizontal photon transport at $\lambda=500$ nm (H_0) and the spectral slopes (S_0) were calculated following the method described in §2.2. Since net horizontal photon transport is derived for a layer, it depends on the geometrical thickness of the layer and, strictly speaking, should be normalized by the thickness of the layer. Here, the layer thickness of the vertical bracket to calculate H_0 and S_0 was fixed to 3 km for simplicity.

Figure 4.2 shows the vertical profile of the net irradiance at 500 nm for the P1_tau25 experiment, partitioned into columns with clouds (red) and clear sky (blue). It illustrates that cloudy columns act as net radiation “donors” because they collectively lose radiation to neighboring clear sky columns. In this case, the loss is greater than the gain, but when weighting these effects by the fractional cloud and clear-sky area, the net effect throughout the domain is zero (as expected due to energy conservation).

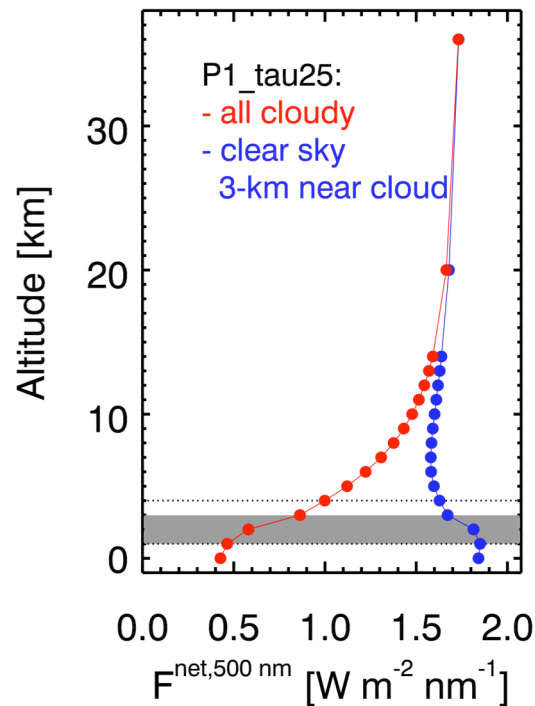


Figure 4.2: Vertical profiles of 3D-modeled net irradiance at 500 nm for the P1_tau25 experiment. The gray shaded area marks the location of the cloud layer. The dashed lines mark the vertical bracket of calculating H_0 . 3D calculations are averaged over all cloudy columns (red) and clear sky columns within 3-km of the cloud (blue).

A vertical cross-section of H_0 through the 3D domain along the x - z plane ($y=30$ km) shows that the largest magnitude of net horizontal photon transport occurs near the cloud edge. It decreases towards the cloud center (but remains positive); conversely, the most negative values are attained in clear sky right next to the cloud. Figure 4.3 also suggests that cloudy pixels do not *always* act as net radiation donors as seen in the P1 experiments, nor do clear sky pixels always act as net radiation recipients. In this case, this can simply be explained by low sun elevation angles, leading to shadows on the East side of the cloud, and irradiance enhancements on the West side. As stated before, there is no correction between cloud optical thickness and horizontal photon transport. The correlation between

H_0 and S_0 is maintained at the pixel level, as demonstrated below (Figure 4.4c), albeit with varying value of ε .

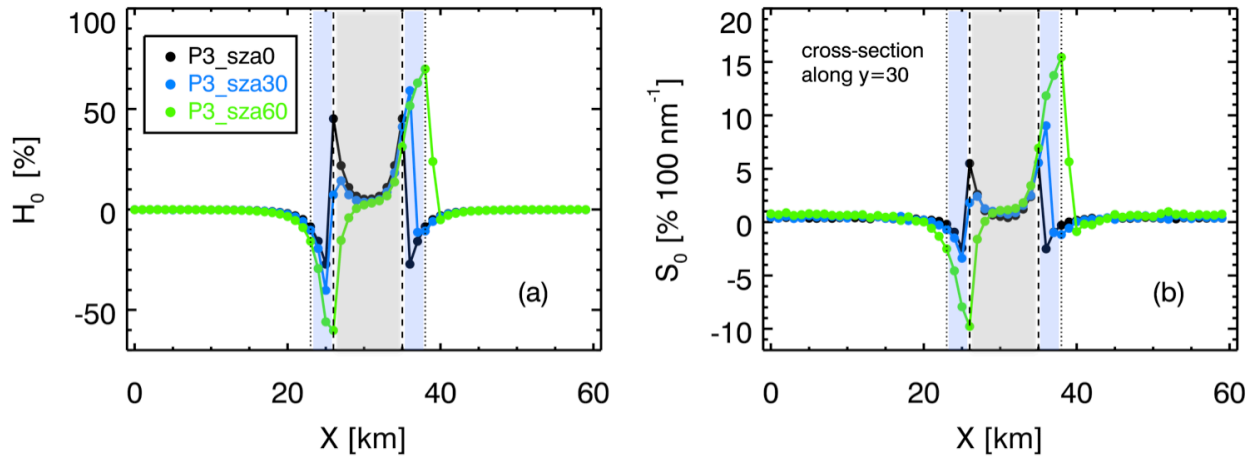


Figure 4.3: (a) Cross-sections of H_0 along the x - z plane at $y=30$ km in the model domain (Figure 4.1) for the P3 experiments. The gray shaded area denotes cloudy regions. The blue shaded area denotes clear sky regions that are 3-km near clouds. (b) same as (a) but for S_0 .

Figure 4.4 shows the H_0 - S_0 relationship for the four experiments. In general, it confirms that even for such highly idealized and simple clouds (as opposed to the ones considered in Chapters 2 and 3), the correlation between H_0 and S_0 is a general phenomenon in inhomogeneous atmospheres. The figure reveals the parameters that affect this relationship. The strongest modulators for ε are the spectral dependency of surface albedo (P2_alb_linear), solar zenith angle (P3), and cloud altitude (P4), each in different ways (see below). Cloud optical thickness (P1) and spectrally constant surface albedo (P2_alb_0*), by contrast, do not exert a strong influence on ε . These parameters determine the spatial distribution (scale) and magnitude of H_0 but have only minor impact on the relationship of H_0 with S_0 (ε unchanged). In the following, this is described in more detail for each of the four experiments:

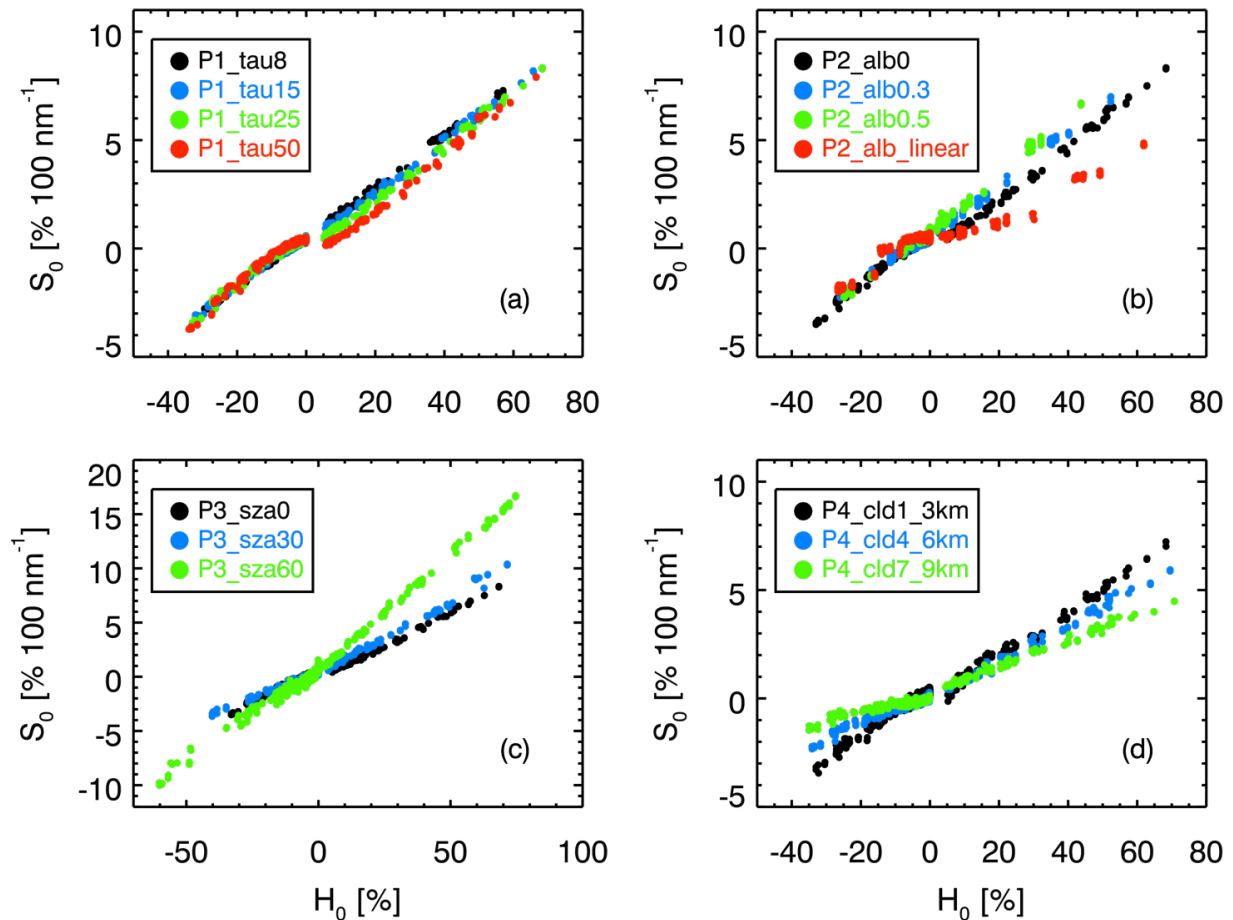


Figure 4.4: Scatterplot of S_0 versus H_0 for the experiments P1-P4.

The P1 experiments explore the impact of varying optical thickness on H_0 , S_0 , and ε . The results suggest that the range of H_0 slightly increases as cloud optical thickness increases (Figure 4.4a and Table 4.2). A wider range of H_0 indicates greater magnitudes of net horizontal photon transport between cloudy and clear-sky columns because the optical thickness contrast between cloudy and clear-sky regions is greater as the optical thickness of the “single isolated cloud” increases. Figure 4.4a also suggests that the H_0 - S_0 relationship can be different for clear-sky ($H_0 < 0$ in this case) and cloudy columns ($H_0 > 0$). For a given

value of H_0 , its spectral slope tends to depend on the optical thickness of cloudy columns (slightly decreasing with optical thickness). This leads to more spread in the H_0 - S_0 relationship on the right. However, S_0 is primarily determined by H_0 rather than the optical thickness, and ε changes only marginally.

Table 4.2: Range of H_0 and S_0 , as well as the effective ε calculated from the H_0 - S_0 relationships shown in Figure 4.4.

Group	Experiment	range(H_0) [%]	range(S_0) [% 100 nm ⁻¹]	ε ¹⁷ [100 nm ⁻¹]
P1. Cloud optical thickness	P1_tau8	86.4	10.1	0.11
	P1_tau15	97.9	11.4	0.11
	P1_tau25	101.3	11.8	0.10
	P1_tau50	100.5	11.6	0.10
P2. Surface albedo	P2_alb0	101.3	11.8	0.10
	P2_alb0.3	78.4	9.3	0.11
	P2_alb0.5	68.7	10.0	0.13
	P2_alb_linear	88.7	6.9	0.12; 0.03 ¹⁸
P3. Solar zenith angle	P3_sza0	101.3	11.8	0.10
	P3_sza30	111.7	14.1	0.12
	P3_sza60	134.8	26.7	0.21
P4. Cloud height	P4_cld1_3km	101.3	10.7	0.10
	P4_cld4_6km	103.7	8.3	0.08
	P4_cld7_9km	105.8	6.0	0.06

The impact of the surface albedo and its spectral dependence is shown in Figure 4.4b. Let us first focus on the results of the experiments with spectrally constant surface albedos. As the surface changes from purely absorptive (albedo=0) to fairly reflective (albedo=0.5), the range of H_0 decreases from 101.3% to 68.7% (see Table 4.2). These results

¹⁷ The uncertainties of ε are within 0.001 (100 nm⁻¹) for *all* experiments.

¹⁸ For the P2_alb_linear experiment, ε was calculated for left and right (divided at $H_0 = -7\%$) branches separately. The results are: $\varepsilon_{left}=0.12$ (100 nm⁻¹) and $\varepsilon_{right}=0.03$ (100 nm⁻¹).

indicate that a more reflective underlying surface tends to lower the magnitude of net horizontal photon transport between cloudy and clear sky regions. When considering the total atmospheric column, the first-order effect of increasing the surface albedo is the reduction in the reflectance contrast between clear-sky and cloudy columns, and this effect decreases the reflectance contrast resulting from the presence of clouds. Despite the differences in magnitude, H_0 - S_0 relationship is preserved for different surface albedo values. This changes when considering the P2_alb_linear experiment (red in Figure 4.4b) with a spectrally dependent surface albedo where three different regimes can be identified: (1) $H_0 < -7\%$ (clear-sky pixels near edge; similar relationship as for constant surface albedo), (2) $-7\% < H_0 < +40\%$ (cloud and clear-sky pixels that is away from edge; similar relationship as for constant surface albedo, but smaller spectral slope for a given magnitude), (3) $H_0 > +40\%$ (cloudy pixels near edge; different ε from rest of domain). The three regimes together cannot be parameterized by one linear relationship, and the non-linear H_0 - S_0 relationship indicates that one single ε is not adequate to characterize the domain-wide net horizontal photon transport in this cloud case. The non-linear relationship is probably due to reflections from the bottom of the cloud. In summary, it also suggests that the spectral dependency of surface albedo may have non-negligible impacts on the spectral behavior of net horizontal photon transport. Therefore, when using the H_0 - S_0 relationship for practical purposes, land surfaces with spectrally dependent surface albedo have to be considered with caution, and more research is necessary to exploit the correlation for remote sensing applications. For this cloud case, this effect is stronger for pixels with higher H_0 values.

The impact of the solar zenith angle (SZA) on net horizontal photon transport is the focus of the P3 experiments. These experiments reveal that the range of H_0 , the range of S_0 ,

and ε all increase as solar zenith angle increases. As the Sun elevation decreases (SZA increases), the effective cloud optical thickness along the slant path increases, and so does the effective cloud geometrical thickness. The former effect leads to an increase in the range of H_0 , which is consistent with the results from the P1 experiments. The latter effect is similar to an extension of the vertical bracket for calculating H_0 , which also increases the range of H_0 . The change in ε (see Table 4.2) is roughly proportional to the change in air mass ($\frac{1}{\cos(SZA)}$ ¹⁹). By contrast, the increase in the range of H_0 is less than the increase in air mass; whereas the increase in the range of S_0 is greater. It is also worth noting that the aspect ratio of the cloud is an important factor that comes into play when the solar zenith angle changes. For the studied case, the cloud aspect ratio ($\frac{\Delta z}{\Delta x} = \frac{\Delta z}{\Delta y} = \frac{2km}{10km}$) is 0.2 and is representative of the boundary layer clouds observed on August 23, 2013, during the SEAC⁴RS field mission (e.g., Figure 3.2b). The cross-section of H_0 in Figure 4.3a shows that when the solar zenith angle increases from 0° to 30°, the cloudy pixels near the sunlit edge (left) become weaker donors of radiation (H_0 decreases from black to blue line) because they receive additional illumination from the side. At SZA=60° (green line), H_0 becomes negative, which means that this cloud edge has become a net recipient of radiation. The critical solar zenith angle at which side illumination causes the transition from net donor to net recipient may vary for cloud scenes with different aspect ratios, and may depend on other scene parameters such as surface albedo and cloud optical thickness.

¹⁹ The value of $\frac{1}{\cos(SZA)}$ is 1.0 (SZA=0°), 1.15 (SZA=30°), and 2.0 (SZA=60°), respectively.

The P4 experiments investigate the impact of cloud height on net horizontal photon transport. As cloud height increases, the range of H_0 slightly increases and the range of S_0 decreases; consequently ε decreases. To understand this behavior, it is helpful to revisit some of the key concepts introduced in Chapter 2. Specifically, §2.6 stated that the spectral dependency of net horizontal photon transport (S_0) can be explained by molecular scattering. As altitude increases, the magnitude of molecular scattering decreases proportionally to the decrease in the number density of atmospheric molecules, which explains the decrease in the range of S_0 .

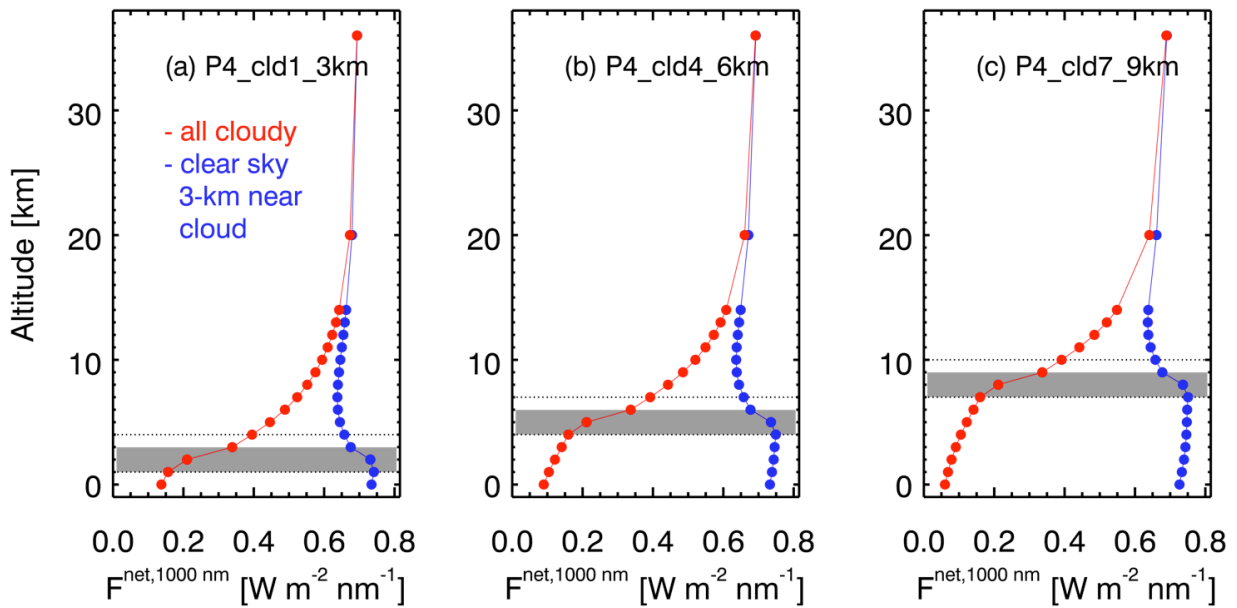


Figure 4.5: Vertical profiles of 3D-modeled net irradiance at 1000 nm for the P4 experiments. The gray shaded area marks the location of the cloud layer. The dashed lines mark the vertical bracket for calculating H , which brackets the layer from the bottom of the cloud to 1-km above. 3D calculations are averaged over all cloudy columns (red) and clear sky columns 3-km near the cloud (blue).

The increase in the range of H_0 can be explained by Eqs. (2.7) and (2.8). The two equations state that the magnitude of net horizontal photon transport at a non-absorbing

visible wavelength can be understood as the combination of two terms ($H_0 = H_\infty + \delta_0$). For the studied case, H_∞ is not affected by changing cloud height as shown in Figure 4.5. However, the absolute magnitude of the second term, $|\delta_0|$, decreases with increasing cloud height due to decrease in ε , which translated into a slightly larger range of H_0 .

In summary, this section addressed the question of “what drives H and ε ” based on a few experiments with different scene parameters. The results should be viewed as a starting point for future studies using more complex and realistic cloud scenes. Further research is needed to better understand the mechanism of why certain parameters do (not) affect ε in various different ways. Such research is prerequisite for using ε in future correction algorithms of 3D cloud effects in cloud remote sensing and energy budget applications. It is important to extend the analysis of net horizontal photon transport and its modulating parameters to wavelengths where clouds, aerosols, or atmospheric gases absorb. The expectation is that knowledge about horizontal photon transport at conservative scattering wavelengths is useful for studies dedicated to atmospheric absorption in spatially inhomogeneous scenes. In the next section, we will examine how cloud and aerosol absorption can be extracted from aircraft measurements under such difficult conditions, in a preliminary attempt to address this issue.

4.2 Extracting layer absorption from aircraft vertical flux divergence measurements

So far we have focused on understanding the net horizontal photon transport of inhomogeneous cloud layers. We now turn our attention to practical applications. In this section, we investigate the retrieval of layer absorption from airborne vertical flux divergence measurements. As discussed in Chapter 2, for any atmospheric layer, the layer

absorption A , net horizontal photon transport H , reflectance R , and transmittance T are connected via the simple energy conservation $A + H = 1 - R - T$. The findings from the previous chapters are useful in order to understand how well A can actually be derived from aircraft measurements. The left-hand side of the energy conservation equation ($A+V$) can be obtained from collocated aircraft irradiance measurements as the vertical flux divergence V . For example, during the TC⁴ and SEAC⁴RS field missions, the SSFR onboard the ER-2 measured upwelling and downwelling shortwave irradiance at an altitude of about 20 km, well above the clouds. The DC-8, equipped with an identical instrument, flew spatially and temporally synchronized flight legs with the ER-2 at a lower altitude, usually below the clouds. Thus the vertical flux divergence from the collocated legs can be obtained as follows:

$$V = (F_{ER-2}^{\downarrow} - F_{ER-2}^{\uparrow}) - (F_{DC-8}^{\downarrow} - F_{DC-8}^{\uparrow}) \quad (4.1)$$

Extracting A from the observations of V requires knowledge of H :

$$A_{nir} = V_{nir} - H_{nir} \quad (4.2)$$

where “nir” indicates that cloud absorption occurs in the near-infrared. H needs to be known at these wavelengths, but cannot be measured independently of V . Because clouds do not absorb in the visible spectral range, the vertical flux divergence equals the net horizontal photon flux: $H_{vis} = V_{vis}$, which can be used as a proxy for H_{nir} :

$$A_{nir} \approx V_{nir} - H_{vis} \quad (4.3)$$

This approach was first proposed by *Ackerman and Cox* [1981] who assumed $H_{nir=0.7-2.8\mu m} = H_{vis=0.3-0.7\mu m}$. It requires that H_{λ} be constant [*Welch et al.*, 1980]. However, the spectral dependence of H_{λ} , discussed in Chapter 2, suggests that this method should be applied with caution, firstly because of the significant spectral dependence of H_{λ} in the visible and near-ultraviolet wavelength range, and secondly because the assumption

$H_{nir} = H_{vis}$ may not always hold. To take the latter into account, *Kassianov and Kogan* [2002] proposed an improved method based on the Ackerman-Cox method that introduces a correction parameter α , with $H_{nir} = \alpha \times H_{vis}$:

$$A_{nir} = V_{nir} - \alpha \times H_{vis} \quad (4.4)$$

This approach requires a priori knowledge of α , which can vary from cloud scene to cloud scene although there are some physical constraints on its range as suggested by *Kassianov and Kogan* [2002]. Here, we study the dependence of α on the geometry of a scene, including the vertical location of the flux divergence legs with respect to the cloud layer. To do this, we revisited the 3D model calculations of the irradiance field of the TC⁴ cloud case observed by collocated DC-8 and ER-2 aircraft on July 17, 2007 (see Chapter 2). The cloud layer (anvil outflow, see Figure 2.4) was located between 8 and 13 km altitude, without any significant aerosol. The ER-2 flew at 20 km, and the DC-8 just below the clouds at 8 km. We consider three vertical brackets: 8-13 km, 8-20 km, and 2-20 km: The first bracket (8-13 km) was chosen to represent a hypothetical flight pattern that tightly encompasses the cloud layer of interest. The second bracket (8-20 km) was the actual observation bracket established by the DC-8 and ER-2 legs. The third bracket, 2-20 km, simulated another hypothetical flight pattern of collocated aircraft observations encompassing more of the lower atmosphere.

To minimize the spectral dependence of H in the near-ultraviolet and visible spectral range as shown in Figure 2.3a, we used H_{1000nm} instead of H_{vis} in Eq. (4.4). Since model calculations are used in this study, the true absorption can be obtained from model outputs, and be used to validate the absorption as estimated by Eq. (4.4). The left column of Figure 4.6 shows the correlation between H_{1600nm} and H_{1000nm} .

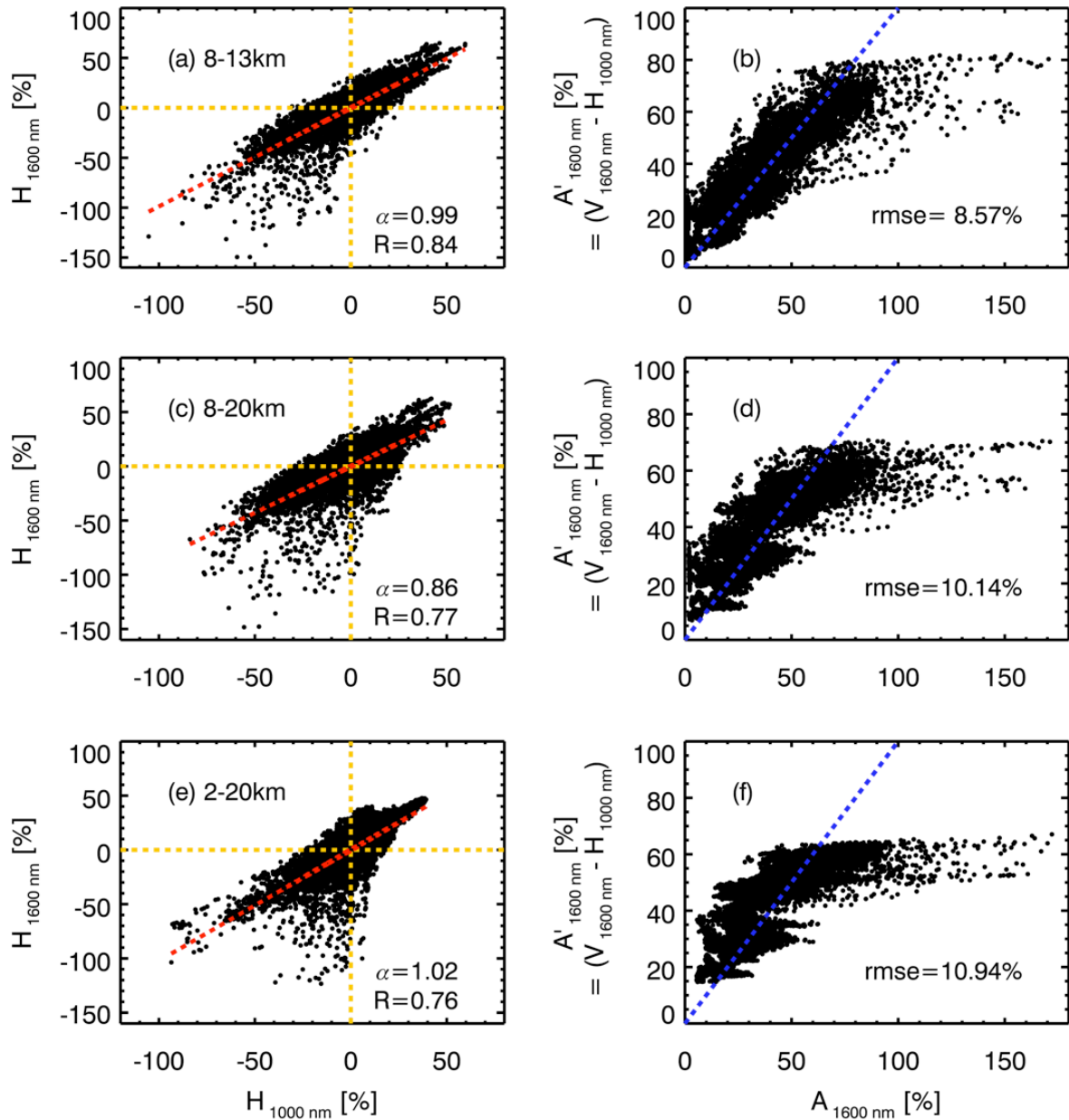


Figure 4.6: (a) Correlation between $H_{1600\text{ nm}}$ and $H_{1000\text{ nm}}$ calculated from the 8-13 km bracket. The red dashed line denotes the linear regression between the two variables. The yellow dashed lines denote x-axis and y-axis. (b) Correlation between the retrieved cloud absorption $A'_{1600\text{ nm}}$ and $A_{1600\text{ nm}}$ within the atmospheric layer of 8-13 km. The blue dashed line denotes the 1:1 relationship. (c) Same as (a) but for the 8-20 km bracket. (d) Same as (b) but for the 8-20 km layer. (e) Same as (a) but for the 2-20 km bracket. (f) Same as (b) but for the 2-20 km bracket. All quantities were normalized by the incident solar radiation at 20 km.

In general, H_{1600nm} is correlated to H_{1000nm} , with a higher correlation coefficient ($R=0.84$) for the bracket that encompasses the cloud most tightly (Figure 4.6a). For this bracket, the value of α is very close to unity ($\alpha=0.99$). For the other two non-ideal brackets (Figures 4.6c, e), the parameter α does change and deviate from unity, and the low correlation coefficients indicate that H_{1000nm} may no longer be used as a proxy for H_{1600nm} . For the 8-20km vertical bracket, $\alpha=0.86<1$, which indicate that $H_{1600nm} > H_{1000nm}$. It is slightly counter-intuitive because the absorption at 1600 nm would be expected to shorten the mean free photon path length. Similar results were reported by *Kassianov and Kogan* [2002] where they found $H_{1.65\mu m} > H_{0.7\mu m}$ (Table 3 and Figures 6 and 7). It is also noteworthy that even for the tightest bracket, there is considerable spread between the H values at the two wavelengths, pointing to the different physics underlying the photon transport in the non-absorbing vs. weakly absorbing regime. This requires further research as the spread was much larger than reported by *Kassianov and Kogan* [2002]. We also derived α from the idealized P1, P2, and P3 experiments discussed in the previous section with a fixed vertical bracket (1-4 km). Our results (not listed) show that α varies from case to case and ranges from 0.66 (P1_tau50) to 1.05 (P3_sza60).

In essence, α is a parameter that transfers 3D cloud effects in *irradiances* from a conservative scattering wavelength to a non-conservative scattering wavelength. A number of recent studies suggest that the spectral ratio of the satellite-measured radiance could be a pathway to transfer the 3D correction in *radiances* from a shorter visible wavelength to a longer wavelength [*Marshak et al.*, 2014; *Kassianov et al.*, 2010]. Although these studies mainly addressed clear sky regions in the vicinity of clouds, their findings of the transfer parameter of 3D cloud effects in *radiances* may be exploited in the future to infer α . Since

this is beyond the scope of this work, we chose not to consider α when extracting absorption from aircraft measurements:

$$A_{1600nm} = V_{1600nm} - H_{1600nm} \approx V_{1600nm} - H_{1000nm} = A'_{1600nm} \quad (4.5)$$

The right column of Figure 4.6 assesses the accuracy of this approximation by comparing A'_{1600nm} (as extracted from synthetic measurements) to the truth (A_{1600nm} , obtained from the model output). Since A_{1600nm} comprises the total absorption by cloud particles and atmospheric molecules (both H₂O and CO₂ absorb at 1600 nm [Coddington *et al.*, 2008]) within the atmospheric layer, it increases as the vertical bracket extends, thus affecting the results. For all three vertical brackets, A_{1600nm} exceeds 100% for roughly 1% of the pixels, which means that more radiation is absorbed than incident from the top. This can be explained by net horizontal photon transport towards these pixels.

The degree of the linear correlation between H_{1600nm} and H_{1000nm} determines the accuracy of A'_{1600nm} , which is quantified by the root-mean-squared-errors as given in the figure:

$$rmse = \sqrt{\sum \frac{1}{N} (A'_{1600nm} - A_{1600nm})^2} \quad (4.6)$$

where N is the number of pixels in the domain. The values of $rmse$ suggest that extending the vertical bracket reduces the accuracy for extracting the true absorption from V .

The results suggest that when using the ideal vertical bracket (Figure 4.6b), the approximation of A_{1600nm} through A'_{1600nm} has an estimated error of $rmse=8.57\%$. Given the complex nature of this problem, i.e., deriving true layer absorption from collocated measurements from above and below, this error is reasonably small. In any future studies of inhomogeneous cloud scenes, measurement-derived absorption and heating rates should be accompanied by such error estimates. This is possible with the method presented here if

imagery or large-eddy simulations of the cloud scene are available in addition to the irradiance measurements themselves. In this case, the estimate of A_{1600nm} becomes less reliable (with an increasing value of $rmse$) as the vertical bracket extends beyond the cloud layer (Figures 4.6d, f). For the ideal vertical bracket, $H_{1600nm} \approx H_{1000nm}$ largely holds and thus the approximation through Eq. (4.5) is the most robust. When extending the vertical bracket, H_{1000nm} becomes less representative of H_{1600nm} , and the bias for estimating H_{1600nm} and A_{1600nm} increases as a result.

Although this study is focused on cloud absorption, its findings are also applicable to the derivation of absorption by other atmospheric constituents such as water vapor or aerosols. During field missions, if the layer absorption from a certain atmospheric constituent is a major objective of a flight, it is essential to choose altitudes as close as possible to the top and bottom of the layer where the major absorbing constituent resides. However, one important requirement for deriving layer absorption from vertical flux divergence measurements is that the magnitude of the true absorption be comparable to, or larger than that of the net horizontal photon transport. If this requirement is not satisfied, it may not be practical to retrieve absorption from aircraft observations even when optimizing the flight pattern. The upcoming NASA ObseRvations of Aerosols above CLouds and their intEractionS (ORACLES) field mission in 2016 might provide an opportunity to build upon the work so far. One of the science objectives of this mission is to characterize the scattering and absorbing properties of aerosols when they co-exist with clouds. A possible scenario is an aerosol layer located above a cloud layer.

To assist with the development of a sampling strategy for the ORACLES mission, we used the “P1_tau25” cloud case discussed in the previous section as the basis for exploring the uncertainties in deriving aerosol absorption above inhomogeneous clouds from aircraft

measurements. We prescribed the aerosol properties in our model calculations as follows to emulate a scenario that would likely be observed: above the single cloud patch that occupies the atmospheric layer between 1 and 3 km with an optical thickness of 25, we added a homogeneous aerosol layer between 4 and 5 km. For simplicity, the aerosol optical thickness was set to decrease linearly from 0.36 at 350 nm to 0.31 at 600 nm. For the aerosol single scattering albedo and asymmetry parameter, we used spectrally constant values of 0.9 and 0.6, respectively. These aerosol properties were approximations to the averaged properties of the biomass burning aerosols in Zambia that exist above Namibian stratus clouds [Dubovik *et al.*, 2002]. Radiative transfer calculations were performed at 6 wavelengths (350, 400, 450, 500, 550, 600 nm) with 10^{11} photons each.

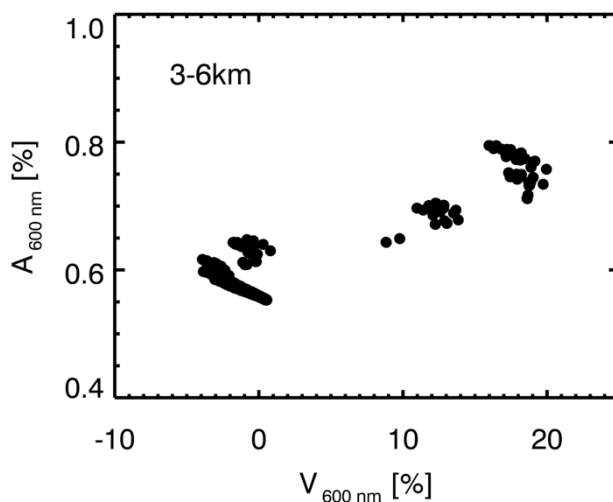


Figure 4.7: The scatterplot of $V_{600\text{ nm}}$ and $A_{600\text{ nm}}$ calculated from the vertical bracket of 3-6 km.

From these synthetic observations, we attempted to extract aerosol absorption from suppositional legs at 3 and 6 km, constituting a flux divergence bracket that would encompass the aerosol layer above the inhomogeneous cloud field. The optimal vertical

location of the legs with regard to the aerosol layer reflects a situation where the altitude of the aerosol layer is known, e.g., from lidar observations. The difficulty in this case is that the above-mentioned requirement is not met as shown in Figure 4.7.

Figure 4.7 illustrates that the aerosol absorption A_{600nm} is one to two orders of magnitude smaller than the vertical flux divergence V_{600nm} . Consequently, the absorption would be extracted as the (small) difference of two large quantities (V and H), even if one could find a way to estimate H independently of V (as discussed above for cloud absorption). The three pixel groups from left to right correspond to clear-sky pixels, cloudy pixels at the cloud edge, and the remaining cloudy pixels. The maximum of V_{600nm} is over 20% whereas the maximum of A_{600nm} is only about 0.8% (relative to the incident irradiance). This result suggests that the net horizontal photon transport due to clouds is the dominating signal that outweighs the true absorption by far – even for the clear-sky pixel group on the left. Moreover, the plot indicates that the true absorption increases (from 0.6% to 0.8%) above clouds. However, the conventional flux divergence sampling approach is ineffective to isolate the aerosol absorption from the cloud signal, let alone allow the detection of the absorption increase in response to the presence of the underlying cloud. Given the nature of this problem, it may not be practical in general, or specifically for the ORACLES mission, to directly retrieve aerosol absorption from collocated irradiance observations in presence of heterogeneous clouds. An alternative approach would be to use cloud imagery in conjunction with aerosol in-situ measurements (or remote sensing products) as input to 3D radiative transfer calculations, and then validate their output with irradiance measurements at various levels (e.g., DC-8 and ER-2 flight levels as for the SEAC⁴RS cases studied in Chapter 3).

4.3 Incorporating spectral information to the estimate of 1D bias in surface transmittance below heterogeneous clouds

Satellite-derived surface energy budget estimates, such as from the Clouds and the Earth’s Radiant Energy System (CERES [Wielicki *et al.*, 1996]), require knowledge of the atmospheric transmittance in addition to the top-of-atmosphere flux density. For the cloudy atmosphere, transmittance is usually obtained from 1D radiative transfer calculations on the basis of MODIS cloud retrievals and other input parameters. As explained in Chapter 2 1D calculations inherently neglect the H term in Eq. (2.1), leading to a bias in transmittance as introduced in Eq. (2.13a):

$$\Delta T_\lambda = T_\lambda^{1D} - T_\lambda^{3D} \quad (4.7)$$

Previous studies determined the 1D transmittance bias to validate satellite-derived surface budget quantities, using (mostly broadband) ground-based observations [e.g., Kratz *et al.*, 2010; Kato *et al.*, 2012]. Validating satellite-derived surface insolation with ground-based instruments is non-trivial because the field-of-view of space-borne instruments usually does not match the spatial sampling of ground-based radiometers [e.g., Zelenka *et al.*, 1999; Wang *et al.*, 2008]. In this section, we use model-calculated spectrally resolved transmitted irradiance in a heterogeneous cloud scene to investigate the scale of errors in 1D transmittance under 3D conditions. We introduce a quantitative metric that is based on spectral information for the degree of cloud heterogeneity and attempt to relate it to the magnitude of the transmittance bias from Eq. (4.7). As explained below, this allows us to assess which sub-set of ground-based data is adequate for validating satellite-derived surface insolation with ground-based observations under heterogeneous conditions.

The possibility of assessing the degree of cloud heterogeneity from spectral information was first considered by *Kindel et al.* [2010], in this case based on *albedo*. The authors retrieved cloud optical thickness and effective radius from the measured albedo at two wavelengths and reconstructed the full albedo spectrum with a 1D model. They then compared the modeled spectral albedo to the spectral measurements, expecting that the spectral residuals (difference between modeled and measured albedo) would be zero at the visible wavelengths. Instead, they found that as cloud fields became more heterogeneous, the residuals were neither zero nor spectrally neutral. Going further, *Schmidt and Pilewskie* [2012] suggested that the spectral inconsistency between 1D-modeled and measured albedo could be used as a metric for cloud heterogeneity.

We tested this concept for 1D- and 3D-modeled surface *transmittance* fields from the 20130816 SEAC⁴RS cloud scene, which was discussed in Chapter 3 (Figure 3.2a). It consisted of two convective cells over land. The 3D-modeled surface transmittance (T_λ^{3D}) was used as a synthetic ground-based observation. From this observation, cloud optical thickness and effective radius were retrieved using transmittance at 650 and 1640 nm [*McBride et al.*, 2011]. From this synthetic cloud retrieval, the full transmittance spectrum was reconstructed with a 1D model (similarly to *Kindel et al.* [2010] for albedo), and the spectral residual was calculated as:

$$T_\lambda^{residual} = T_\lambda^{1D, reconstructed} - T_\lambda^{3D} \quad (4.8)$$

For heterogeneous clouds, $T_\lambda^{residual}$ is expected to be spectrally dependent because T and H are correlated and consequently, the spectral dependence of H propagates into the transmittance as illustrated in Figure 2.9b. Rather than considering the full spectrum of the transmittance, we only use its value at 470 nm ($T_{470nm}^{residual}$) in the following.

Note that $T_{\lambda}^{1D, reconstructed}$ in Eq. (4.8) is different from T_{λ}^{1D} in Eq. (4.7); the latter is the 1D transmittance calculated from the input cloud field whereas the former is the 1D transmittance corresponding to the synthetic cloud retrievals at a wavelength (470 nm) other than the retrieval's (650 nm). Figure 4.8a shows the relationship between $T_{470nm}^{residual}$ [the synthetic observable from Eq. (4.8)] and ΔT_{λ} [the parameter of interest from Eq. (4.7)]. It shows no robust correlation when considering all measurements below clouds, which means that $T_{470nm}^{residual}$ cannot be used as a proxy for ΔT_{470nm} over the domain as a whole.

In Chapter 2 we demonstrated that below clouds, 3D cloud effects differ for atmospheric columns of low or high optical thicknesses. To take this into account here, we stratified the data from Figure 4.8a into cloudy columns that are optically thin ($\tau < 2$) and thick ($\tau > 50$) and found that the 1D bias in surface transmittance is mostly positive for thin clouds and negative for thick clouds. This means that compared to the observations, the surface insolation derived from satellites (via 1D radiative transfer calculations) would be overestimated below thin clouds and underestimated below very thick clouds. In contrast to the full data set, the low- and high-optical thickness sub-sets do show a correlation between ΔT_{470nm} and $T_{470nm}^{residual}$, although more work will be needed to establish whether it occurs for different types of cloud scenes as well, and to investigate the physical reasons.

These findings suggest that $T_{470nm}^{residual}$ may be used as a proxy for ΔT if the data are appropriately stratified, provided that the relationship can be generalized to other cloud scenes. To further study the correlation, we divided $T_{470nm}^{residual}$ into five ranges²⁰ and explored the probability distribution of ΔT_{470nm} within each range (Figure 4.8b and Table 4.3). We

²⁰ The $T_{470nm}^{residual}$ ranges were mainly determined to provide sufficient statistics.

refer to columns whose $T_{470nm}^{residual}$ value is less than -0.01 or greater than 0.01 as heterogeneous and to those with $|T_{470nm}^{residual}| < 0.01$ as quasi-homogeneous.

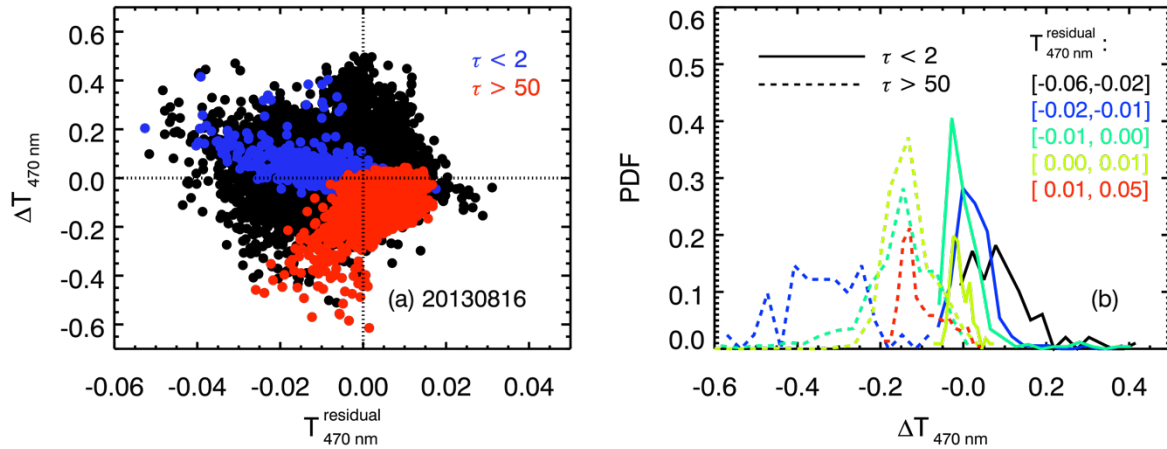


Figure 4.8: (a) Scatterplot of ΔT_{470nm} [calculated from Eq. (4.7)] against $T_{470nm}^{residual}$ [calculated from Eq. (4.8)] for all cloudy (black), optically thin (blue, $\tau < 2$), and optically thick (red, $\tau > 50$) columns of the 20130816 SEAC⁴RS cloud case. (b) Probability distributions of ΔT_{470nm} within five $T_{470nm}^{residual}$ ranges for both low (solid lines) and high (dashed lines) cloud optical thickness columns. The mean of each distribution is listed in Table 4.3.

Table 4.3: Retrieved heterogeneity and the mean of probability distribution, calculated from ΔT_{470nm} within five $T_{470nm}^{residual}$ ranges for both optically low (solid lines in Figure 4.8) and high (dashed lines in Figure 4.8) cloudy columns.

Retrieved heterogeneity	$T_{470nm}^{residual}$	$\overline{\Delta T_{470nm}}, \tau < 2$	$\overline{\Delta T_{470nm}}, \tau > 50$
heterogeneous	[-0.06, -0.02]	0.10	n/a (no enough pixels)
	[-0.02, -0.01]	0.04	-0.32
quasi-homogenous	[-0.01, 0]	0.02	-0.14
	[0, 0.01]	-0.003	-0.11
heterogeneous	[0.01, 0.05]	n/a (no enough pixels)	-0.09

When the cloudy column is highly heterogeneous (the 2nd, 3rd, and 6th rows in Table 4.3), the 1D-modeled surface transmittance is biased regardless of the cloud optical thickness. For optically thin cloudy columns (solid lines in Figure 4.8b and the 3rd column in

Table 4.3), as they become less heterogeneous and more homogeneous, the 1D bias decreases and eventually approaches zero. This means that the 1D model can accurately estimate the surface transmittance below homogeneous thin clouds. However, below thick clouds (dashed lines in Figure 4.8b and the 4th column in Table 4.3), the 1D transmittance bias does not decrease to zero with increasing homogeneity of the scene, and the 1D model underestimates the surface transmittance by about 10%.

The CERES algorithm for computing surface fluxes places all cloudy columns into the same cloud category [*Charlock et al.*, 1997]. Our results show the merit of further stratifying the data into optically thin and thick sub-categories. For these categories, assessing the degree of cloud heterogeneity from spectral information can be useful when comparing ground-based observations to satellite estimates of surface insolation. The approach would be to only use those observations where the residual in one of the categories suggests that $\Delta T \approx 0$. However, this is only possible if the spectral information is available in the observations. Furthermore, spectrally resolved irradiance measurements at the ground would be useful to verify the significant bias of 10% that we found above on the basis of synthetic measurements.

In this section, the 1D bias in surface transmittance below heterogeneous clouds and its connection with the degree of cloud heterogeneity was studied at the 0.2-km spatial scale, the native resolution in the radiative transfer model. Future studies, supported by actual measurements, are needed for a range of cloud conditions to ascertain the generality of our findings at aggregated spatial scales, up to at least tens of kilometers (the native resolution of CERES-like space-borne instruments).

Chapter 5

Summary

This thesis work was motivated by observing that the three-dimensional (3D) characteristics of clouds were not adequately considered in shortwave cloud radiation studies despite years of active research in this area. This is only partially due to lacking computer power because there is the more fundamental problem that 3D radiation transfer ignores the boundaries of pixels and columns, which are at the core of passive remote sensing as we know it today. Since the radiative properties of any given pixel depend on its spatial context, it is impossible to solve this problem in an isolated manner. This conceptual problem has limited progress in determining the cloud (and aerosol) radiative effects from remote sensing in spatially complex scenes.

The discoveries leading up to this dissertation offered a potentially new avenue for approaching this problem: New observations suggested that pixel-to-pixel net horizontal photon transport, one of the most important 3D effects, seemed to be accompanied by a spectral perturbation which, if propagated into radiances, could form the basis for spectrally-based corrections for biases from pixel-to-pixel exchange processes. Rather than explicitly considering the pixel-to-pixel photon transport in a computationally costly 3D retrieval framework, the effects could then simply be detected by means of their spectral signature.

Before such approaches can gain any practical significance, it was necessary to understand the physical mechanisms and find observational evidence for the relationship between spatial structure and spectral perturbations in irradiance and radiance. Recent NASA aircraft field experiments provided the data to pursue this research, which sought a comprehensive understanding of the relationship between spatially inhomogeneous cloud scenes, the biases in remote sensing and radiative effects, and the spectral dimension of the problem. In this dissertation, we focused primarily on clouds, in an effort to pave the way for later research that also considers aerosols.

In this work, we proved with measurements and 3D model calculations that cloud spatial structure manifests itself as spectral signature in (1) *irradiance* fields, specifically in the form of net horizontal photon transport and (2) *radiance* fields. The spectral signature of 3D cloud effects in irradiances is apparent as a domain-wide correlation between magnitudes (H_0) of net horizontal photon transport and its spectral dependence (S_0) in the near-ultraviolet and visible wavelength range (§2.5, §2.7, and §3.5). We also proved that the underlying physical mechanism for the spectral dependence of H is molecular scattering in conjunction with cloud inhomogeneity (§2.6). On this basis, we were able to develop a simple parameterization built upon a single parameter ε to describe the spectral signature of 3D cloud effects in irradiances. Since the parameterization holds for individual pixels and the domain as a whole, ε can be used as a new non-local *spectral* metric for describing *spatial* cloud heterogeneity in addition to the traditional metrics based on distance to the nearest cloud [Várnai and Marshak, 2015] or the standard deviation of cloud properties in a domain [Liang et al., 2009]. Combined, these metrics may become quite powerful tools for coping with complex cloud scenes in the future. It should be noted that ε depends on a number of scene parameters of a given cloud field. Our preliminary assessment showed that

in absence of aerosols, the primary modulators of ε are the solar zenith angle, surface albedo, and cloud height (§4.1).

The spectral signature of 3D cloud effects in radiances is apparent as a distinct relationship between the magnitude (\mathfrak{R}_0) of reflectance, the traditional observable in cloud remote sensing, and its spectral dependence (ζ_0) in the visible wavelength range (§3.4). Mapping the measurements and model results for all pixels in \mathfrak{R}_0 - ζ_0 space provides a new perspective on 3D effects throughout the domain. We showed that only 3D calculations reproduced the distribution of pixel populations in this space, and we identified two different branches that can be ascribed to cloudy and clear-sky pixels. In this sense, the spectral dependence as new observable in cloud remote sensing provides information on the macroscopic structure of the scene as a whole.

After establishing the connections between spectral perturbations and cloud inhomogeneities, we investigated whether irradiance and radiance perturbations are related (§3.6). We found this to be the case, although a correlation cannot be established on a pixel-by-pixel basis. This makes immediate sense because radiance and irradiance fields in inhomogeneous cloud fields are affected to different extent by the pixel context. Instead, the connection can be made on the basis of pixel *populations*, grouped into cloudy and clear-sky categories. The mapping from \mathfrak{R}_0 - ζ_0 to irradiance space was not independent of scene parameters such as cloud cover and surface albedo. It would be premature to say that the spectral signature in radiances can be used to infer the magnitude of net horizontal photon flux via its spectral signature because these other scene parameters have been insufficiently studied. However, this work systematically reconciled the model-predicted spectral perturbations with the measurements for a number of different cloud scenes. This gives rise to the hope that the spectral signature of 3D cloud effects can be used to

introduce first-order bias corrections for radiative cloud effects as derived from remote sensing.

To appreciate the magnitude of such biases, we carried out a radiative closure study of transmitted irradiance below broken cloud fields, which is understood as the consistency of the transmittance irradiance field (a) as predicted from airborne imagery from above versus (b) direct measurements from below (§3.7, §3.B.3). Since the distribution of downwelling irradiance under such an inhomogeneous cloud field is bi-modal (measurements below clouds where the direct beam is attenuated and measurements below cloud gaps), any such analysis needs to consider the two modes separately [Schmidt *et al.*, 2009]. For the cases we analyzed, we found that the total bias between the model calculations and observations was significant, resulting in an underestimation of downwelling irradiance below clouds (up to a factor of two), and an overestimation below cloud gaps. In an earlier study [Schmidt *et al.*, 2010b], measurement-model discrepancies arose when neglecting 3D effects in the irradiance calculations from cloud remote sensing products, which themselves were not significantly biased. By contrast, we found in our analysis that the cloud products were also affected by 3D radiative transport. We recognized the need for a separate assessment of *irradiance vs. remote sensing* bias, and developed a methodology to estimate them for cloudy and clear pixels. We found that the two biases contributed about equally to the total error below clouds, in stark contrast to the earlier study. The reason for the contradictory findings probably lies in the scale of the cloud inhomogeneity (much larger in the earlier study). A more systematic assessment of the scale-dependence of the bias partitioning is left to future studies. For clear-sky pixels in the vicinity of clouds, the remote sensing bias is negligible, which means that the optical

properties of the clouds are less relevant for the 3D distribution of irradiance around clouds than the location of clouds.

Although the connections between spatial structure and spectral effects need to be studied more thoroughly in the near future, we turned our attention to potential applications at the end of this work. Most importantly, adding aerosols to inhomogeneous clouds introduce another degree of complexity to this problem by adding further spectral perturbations to the radiance and irradiance fields. Isolating the relatively weak aerosol signal against the strong background established by the cloud is a challenging endeavor. This became immediately obvious in a so-called proxy study for a hypothetical aircraft experiment that targets the radiative effects of an aerosol layer above inhomogeneous clouds. We showed that “flux divergence legs”, bracketing the aerosol layer, cannot be used to derive the aerosol absorption and heating rate because the signal as detected by the aircraft irradiance sensors would be dominated by the variability in the net horizontal flux, due to the inhomogeneity of the underlying cloud field (§4.2).

It remains to be seen how aerosol absorption can be derived when conducting actual field experiments with this sampling strategy. The most promising approach seems to emerge from the closure study presented in Chapter 3, where cloud imagery and irradiance measurements are used in conjunction to determine the radiative effects of clouds. Since this closure is done through irradiance rather than through the derived quantities such as absorption, the measurement errors are small enough to allow a meaningful comparison of the measurements with the calculations. This is important because these measurement-validated calculations and their range of uncertainty (derived from the discrepancy between measured and modeled quantities) form the basis for isolating aerosol effects, which can be quantified separately *only if* their impact on the irradiance exceeds the range of uncertainty

in the measurement-validated irradiance calculations. This is, in essence, the approach of *Schmidt et al.* [2009], although they used large eddy simulations rather than cloud imagery to prescribe the cloud fields. In the case of SEAC⁴RS, the range of uncertainty in the measurement-validated irradiance spectra in cloud gaps was comparable to the aerosol effect itself (in cloud gaps) because of the low aerosol loading.

To cope with the complexity of cloud-aerosol fields in future field experiments, it will be essential to assess the impact of aerosols separately for cloudy and clear pixels, as was done for the cloud radiative closure study in this work. Grouping the pixels into distinct populations is helpful because the spectral perturbations from cloud inhomogeneities and aerosols can then be assessed statistically. The different spectral dependence of aerosol and cloud inhomogeneity in the cloudy and clear categories may be another way to segregate aerosol and cloud radiative effects. This will need to be explored in future research.

Another important practical application of spectrally resolved observations under inhomogeneous cloud conditions is the validation of satellite-derived surface insolation with ground-based measurements. We used model calculations to show that spectral information can be used as a proxy for the transmittance bias due to 3D effects (§4.3). Such approaches should be further developed and tested with ground-based observations.

Summarizing, we are only just beginning to understand the utility of spectral observations for cloud-aerosol scenes with a high level of complexity. Our research highlighted the connections between spatial structure and spectral perturbations in airborne observations of such scenes. After examining the robustness of such correlations for a wider range of cloud conditions, they could be the starting point for developing first-order 3D bias corrections by way of parameterizations in a 1D retrieval framework.

Bibliography

- Ackerman, S. A., and S. K. Cox (1981), Aircraft Observations of the Shortwave Fractional Absorptance of Non-Homogeneous Clouds, *J. Appl. Meteorol.*, *20*(12), 1510–1515, doi:10.1175/1520-0450(1981)020<1510:AOOTSF>2.0.CO;2.
- Arking, A. (1999), The influence of clouds and water vapor on atmospheric absorption, *Geophys. Res. Lett.*, *26*(17), 2729–2732, doi:10.1029/1999GL900544.
- Arnott, W. P., Moosmuller, H., Sheridan, P. J., Ogren, J. A., Raspet, R., Slaton, W. V., Hand, J. L., Kreidenweis, S. M., and Collett Jr., J. L. (2003). Photoacoustic and filter-based ambient aerosol light absorption measurements: instrument comparisons and the role of relative humidity, *J. Geophys. Res.*, *108*(D1), 4034, doi:10.1029/2002JD002165.
- Baldridge, A. M., S. J. Hook, C. I. Grove, and G. Rivera (2009), The ASTER spectral library version 2.0, *Remote Sens. Environ.*, *113*(4), 711–715, doi:10.1016/j.rse.2008.11.007.
- Barker, H. W., M. P. Jerg, T. Wehr, S. Kato, D. P. Donovan, and R. J. Hogan (2011), A 3D cloud-construction algorithm for the EarthCARE satellite mission, *Q. J. R. Meteorol. Soc.*, *137*(657), 1042–1058, doi:10.1002/qj.824.
- Barker, H. W., S. Kato, and T. Wehr (2012), Computation of Solar Radiative Fluxes by 1D and 3D Methods Using Cloudy Atmospheres Inferred from A-train Satellite Data, *Surv. Geophys.*, *33*(3-4), 657–676, doi:10.1007/s10712-011-9164-9.
- Baum, B. A., P. Yang, A. J. Heymsfield, C. G. Schmitt, Y. Xie, A. Bansemmer, Y.-X. Hu, and Z. Zhang (2011), Improvements in shortwave bulk scattering and absorption models for the remote sensing of ice clouds, *J. Appl. Meteorol. Climatol.*, *50*(5), 1037–1056, doi:10.1175/2010JAMC2608.1.
- Bergstrom, R. W., P. Pilewskie, B. Schmid, and P. B. Russell (2003), Estimates of the spectral aerosol single scattering albedo and aerosol radiative effects during SAFARI 2000, *J. Geophys. Res. Atmos.*, *108*(D13), 8474, doi:10.1029/2002JD002435.
- Bodhaine, B. A., N. B. Wood, E. G. Dutton, and J. R. Slusser (1999), On Rayleigh Optical Depth Calculations, *J. Atmos. Ocean. Technol.*, *16*(11), 1854–1861, doi:10.1175/1520-0426(1999)016<1854:ORODC>2.0.CO;2.
- Brock, C. A., J. Cozic, R. Bahreini, K. D. Froyd, A. M. Middlebrook, A. McComiskey, J. Brioude, O. R. Cooper, A. Stohl, K. C. Aikin, J. A. de Gouw, D. W. Fahey, R. A. Ferrare, R. S. Gao, W. Gore, J. S. Holloway, G. Hübler, A. Jefferson, D. A. Lack, S. Lance, R. H. Moore, D. M. Murphy, A. Nenes, P. C. Novelli, J. B. Nowak, J. A. Ogren, J. Peischl, R.

- B. Pierce, P. Pilewskie, P. K. Quinn, T. B. Ryerson, K. S. Schmidt, J. P. Schwarz, H. Sodemann, J. R. Spackman, H. Stark, D. S. Thomson, T. Thornberry, P. Veres, L. A. Watts, C. Warneke, and A. G. Wollny (2011), Characteristics, sources, and transport of aerosols measured in spring 2008 during the aerosol, radiation, and cloud processes affecting Arctic Climate (ARCPAC) Project, *Atmos. Chem. Phys.*, *11*(6), 2423–2453, doi:10.5194/acp-11-2423-2011.
- Bucholtz, A., R. T. Bluth, B. Kelly, S. Taylor, K. Batson, A. W. Sarto, T. P. Tooman, and R. F. McCoy (2008), The Stabilized Radiometer Platform (STRAP)—An Actively Stabilized Horizontally Level Platform for Improved Aircraft Irradiance Measurements, *J. Atmos. Ocean. Technol.*, *25*(12), 2161–2175, doi:10.1175/2008JTECHA1085.1.
- Cahalan, R. ., L. Oreopoulos, G. Wen, A. Marshak, S.-C. Tsay, and T. DeFelice (2001), Cloud characterization and clear-sky correction from Landsat-7, *Remote Sens. Environ.*, *78*(1-2), 83–98, doi:10.1016/S0034-4257(01)00251-6.
- Chambers, L. H., B. A. Wielicki, and K. F. Evans (1997), Accuracy of the independent pixel approximation for satellite estimates of oceanic boundary layer cloud optical depth, *J. Geophys. Res. Atmos.*, *102*(D2), 1779–1794, doi:10.1029/96JD02995.
- Charlock, T. P., F. G. Rose, D. A. Rutan, T. A. Alberta, D. P. Kratz, L. H. Coleman, G. L. Smith, N. M. Smith, and T. D. Bess (1997), Clouds and the Earth’s Radiant Energy System (CERES) algorithm theoretical basis document: Compute surface and atmospheric fluxes (subsystem 5), *CERES Algorithm Theor. Basis Doc.*
- Charlock, T. P., F. G. Rose, D. A. Rutan, Z. Jin, and S. Kato (2006), The global surface and atmosphere radiation budget: an assessment of accuracy with 5 years of calculations and observations, in *Proceedings of 12th conference on atmospheric radiation*, pp. 10–14.
- Coddington, O., K. S. Schmidt, P. Pilewskie, W. J. Gore, R. W. Bergstrom, M. Román, J. Redemann, P. B. Russell, J. Liu, and C. C. Schaaf (2008), Aircraft measurements of spectral surface albedo and its consistency with ground-based and space-borne observations, *J. Geophys. Res.*, *113*(D17), D17209, doi:10.1029/2008JD010089.
- Coddington, O. M., P. Pilewskie, J. Redemann, S. Platnick, P. B. Russell, K. S. Schmidt, W. J. Gore, J. Livingston, G. Wind, and T. Vukicevic (2010), Examining the impact of overlying aerosols on the retrieval of cloud optical properties from passive remote sensing, *J. Geophys. Res.*, *115*(D10), D10211, doi:10.1029/2009JD012829.
- Davis, A. B., and A. Marshak (2010), Solar radiation transport in the cloudy atmosphere: a 3D perspective on observations and climate impacts, *Reports Prog. Phys.*, *73*(2), 26801.
- Dubovik, O., B. Holben, T. F. Eck, A. Smirnov, Y. J. Kaufman, M. D. King, D. Tanré, and I. Slutsker (2002), Variability of absorption and optical properties of key aerosol types observed in worldwide location., *J. Atmos. Sci.*, *59*, 590–608.
- Dunagan, S., R. Johnson, J. Zavaleta, P. Russell, B. Schmid, C. Flynn, J. Redemann, Y. Shinozuka, J. Livingston, and M. Segal-Rosenhaimer (2013), Spectrometer for Sky-Scanning Sun-Tracking Atmospheric Research (4STAR): Instrument Technology, *Remote Sens.*, *5*(8), 3872–3895, doi:10.3390/rs5083872.

- Faure, T., H. Isaka, and B. Guillemet (2001), Neural network retrieval of cloud parameters of inhomogeneous and fractional clouds, *Remote Sens. Environ.*, *77*(2), 123–138, doi:10.1016/S0034-4257(01)00199-7.
- Fritz, S., and T. H. MacDonald (1951), Measurements of absorption of solar radiation by clouds, *Bull. Am. Meteorol. Soc.*, *32*, 205–209.
- Hair, J. W., C. A. Hostetler, A. L. Cook, D. B. Harper, R. A. Ferrare, T. L. Mack, W. Welch, L. R. Izquierdo, and F. E. Hovis (2008), Airborne High Spectral Resolution Lidar for profiling aerosol optical properties, *Appl. Opt.*, *47*(36), 6734–6752, doi:10.1364/AO.47.006734.
- Ham, S.-H., S. Kato, H. W. Barker, F. G. Rose, and S. Sun-Mack (2014), Effects of 3-D clouds on atmospheric transmission of solar radiation: Cloud type dependencies inferred from A-train satellite data, *J. Geophys. Res. Atmos.*, *119*(2), 943–963, doi:10.1002/2013JD020683.
- Heney, L. G., and J. L. Greenstein (1941), Diffuse radiation in the galaxy, *Astrophys. J.*, *93*, 70–83.
- Illingworth, A. J., H. W. Barker, A. Beljaars, M. Ceccaldi, H. Chepfer, N. Clerbaux, J. Cole, J. Delanoé, C. Domenech, D. P. Domenech, D. P. Donovan, S. Fukuda, M. Hirakata, R. J. Hogan, A. Huenerbein, P. Kollias, T. Kubota, T. Nakajima, T. Y. Nakajima, T. Nishizawa, Y. Ohno, H. Okamoto, R. Oki, K. Sato, M. Sastoh, M. W. Shephard, V. Velázquez-Blázquez, U. Wandlinger, T. Wehr, and G. J. van Zadelhoff (2015), The EarthCARE satellite: The next step forward in global measurements of clouds, aerosols, precipitation, and radiation, *Bull. Am. Meteorol. Soc.*, *96*(8), 1311–1332, doi:10.1175/BAMS-D-12-00227.1.
- Iwabuchi, H. (2006), Efficient Monte Carlo methods for radiative transfer modeling, *J. Atmos. Sci.*, *63*(9), 2324–2339, doi:10.1175/JAS3755.1.
- Iwabuchi, H., and T. Hayasaka (2003), A multi-spectral non-local method for retrieval of boundary layer cloud properties from optical remote sensing data, *Remote Sens. Environ.*, *88*(3), 294–308, doi:10.1016/j.rse.2003.08.005.
- Kassianov, E., M. Ovchinnikov, L. K. Berg, S. A. McFarlane, C. Flynn, R. Ferrare, C. Hostetler, and M. Alexandrov (2010), Retrieval of aerosol optical depth in vicinity of broken clouds from reflectance ratios: case study, *Atmos. Meas. Tech.*, *3*(5), 1333–1349, doi:10.5194/amt-3-1333-2010.
- Kassianov, E. I., and Y. L. Kogan (2002), Spectral dependence of radiative horizontal transport in stratocumulus clouds and its effect on near-IR absorption, *J. Geophys. Res.*, *107*(D23), 4712, doi:10.1029/2002JD002103.
- Kato, S., N. G. Loeb, F. G. Rose, D. R. Doelling, D. A. Rutan, T. E. Caldwell, L. Yu, and R. A. Weller (2013), Surface Irradiances Consistent with CERES-Derived Top-of-Atmosphere Shortwave and Longwave Irradiances, *J. Clim.*, *26*(9), 2719–2740, doi:10.1175/JCLI-D-12-00436.1.
- Kindel, B. C., K. S. Schmidt, P. Pilewskie, B. A. Baum, P. Yang, and S. Platnick (2010), Observations and modeling of ice cloud shortwave spectral albedo during the Tropical Composition, Cloud and Climate Coupling Experiment (TC⁴), *J. Geophys. Res. Atmos.*,

115(D10), D00J18, doi:10.1029/2009JD013127.

- Kindel, B. C., P. Pilewskie, K. S. Schmidt, O. Coddington, and M. D. King (2011), Solar spectral absorption by marine stratus clouds: Measurements and modeling, *J. Geophys. Res. Atmos.*, *116*(D10), D10203, doi:10.1029/2010JD015071.
- King, M. D., Y. J. Kaufman, W. P. Menzel, and D. Tanre (1992), Remote sensing of cloud, aerosol, and water vapor properties from the moderate resolution imaging spectrometer (MODIS), *IEEE Trans. Geosci. Remote Sens.*, *30*(1), 2–27, doi:10.1109/36.124212.
- King, M. D., W. P. Menzel, P. S. Grant, J. S. Myers, G. T. Arnold, S. E. Platnick, L. E. Gumley, S. C. Tsay, C. C. Moeller, M. Fitzgerald, K. S. Brown, and F. G. Osterwisch (1996), Airborne scanning spectrometer for remote sensing of cloud, aerosol, water vapor, and surface properties, *J. Atmos. Ocean. Technol.*, *13*(4), 777–794, doi:10.1175/1520-0426(1996)013<0777:ASSFRS>2.0.CO;2.
- King, M. D., S. Platnick, G. Wind, G. T. Arnold, and R. T. Dominguez (2010), Remote sensing of radiative and microphysical properties of clouds during TC⁴: Results from MAS, MASTER, MODIS, and MISR, *J. Geophys. Res. Atmos.*, *115*(D10), D00J07, doi:10.1029/2009JD013277.
- Kratz, D. P., S. K. Gupta, A. C. Wilber, and V. E. Sotthcott (2010), Validation of the CERES Edition 2B Surface-Only Flux Algorithms, *J. Appl. Meteorol. Climatol.*, *49*(1), 164–180, doi:10.1175/2009JAMC2246.1.
- Kurucz, R. (1992), Synthetic Infrared Spectra, in *Infrared Solar Physics: Proceedings of the 154th Symposium of the International Astronomical Union*, edited by D. M. Rabin, J. T. Jefferies, and C. Lindsey, pp. 523–531, Springer Netherlands.
- LeBlanc, S. E., P. Pilewskie, K. S. Schmidt, and O. Coddington (2015), A spectral method for discriminating thermodynamic phase and retrieving cloud optical thickness and effective radius using transmitted solar radiance spectra, *Atmos. Meas. Tech.*, *8*(3), 1361–1383.
- Li, L., G. M. Heymsfield, P. E. Racette, L. Tian, and E. Zenker (2004), A 94-GHz Cloud Radar System on a NASA High-Altitude ER-2 Aircraft, *J. Atmos. Ocean. Technol.*, *21*(9), 1378–1388, doi:10.1175/1520-0426(2004)021<1378:AGCRSO>2.0.CO;2.
- Liang, L., L. Di Girolamo, and S. Platnick (2009), View-angle consistency in reflectance, optical thickness and spherical albedo of marine water-clouds over the northeastern Pacific through MISR-MODIS fusion, *Geophys. Res. Lett.*, *36*, L09811, doi:10.1029/2008GL037124.
- Liou, K.-N. (2002), An introduction to atmospheric radiation, Academic press.
- Liu, C.-L., and A. J. Illingworth (2000), Toward More Accurate Retrievals of Ice Water Content from Radar Measurements of Clouds, *J. Appl. Meteorol.*, *39*(7), 1130–1146, doi:10.1175/1520-0450(2000)039<1130:TMAROI>2.0.CO;2.
- Loeb, N. G., and J. A. Coakley (1998), Inference of Marine Stratus Cloud Optical Depths from Satellite Measurements: Does 1D Theory Apply?, *J. Clim.*, *11*(2), 215–233, doi:10.1175/1520-0442(1998)011<0215:IOMSCO>2.0.CO;2.

- Loeb, N. G., S. Kato, K. Loukachine, and N. Manalo-Smith (2005), Angular Distribution Models for Top-of-Atmosphere Radiative Flux Estimation from the Clouds and the Earth's Radiant Energy System Instrument on the Terra Satellite. Part I: Methodology, *J. Atmos. Ocean. Technol.*, *22*(4), 338–351, doi:10.1175/JTECH1712.1.
- Marshak, A., and A. Davis (2005), *3D radiative transfer in cloudy atmospheres*, Springer Science & Business Media.
- Marshak, A., A. Davis, W. Wiscombe, and R. Cahalan (1995), Radiative smoothing in fractal clouds,
- Marshak, A., W. Wiscombe, A. Davis, L. Oreopoulos, and R. Cahalan (1999), On the Removal of the Effect of Horizontal Fluxes In Two-Aircraft Measurements of Cloud Absorption, *Q. J. R. Meteorol. Soc.*, *125*(558), 2153–2170, doi:10.1002/qj.49712555811.
- Marshak, A., S. Platnick, T. Várnai, G. Wen, and R. F. Cahalan (2006), Impact of three-dimensional radiative effects on satellite retrievals of cloud droplet sizes, *J. Geophys. Res. Atmos.*, *111*(D9), D09207, doi:10.1029/2005JD006686.
- Marshak, A., G. Wen, J. A. Coakley, L. A. Remer, N. G. Loeb, and R. F. Cahalan (2008), A simple model for the cloud adjacency effect and the apparent bluing of aerosols near clouds, *J. Geophys. Res. Atmos.*, *113*(D14), D14S17, doi:10.1029/2007JD009196.
- Marshak, A., K. F. Evans, T. Várnai, and G. Wen (2014), Extending 3D near-cloud corrections from shorter to longer wavelengths, *J. Quant. Spectrosc. Radiat. Transf.*, *147*, 79–85, doi:10.1016/j.jqsrt.2014.05.022.
- Mayer, B., and A. Kylling (2005), Technical note: The libRadtran software package for radiative transfer calculations - description and examples of use, *Atmos. Chem. Phys.*, *5*(7), 1855–1877, doi:10.5194/acp-5-1855-2005.
- McBride, P. J., K. S. Schmidt, P. Pilewskie, A. S. Kittelman, and D. E. Wolfe (2011), A spectral method for retrieving cloud optical thickness and effective radius from surface-based transmittance measurements, *Atmos. Chem. Phys.*, *11*(14), 7235–7252, doi:10.5194/acp-11-7235-2011.
- Meyer, K., S. Platnick, G. T. Arnold, R. E. Holz, P. Veglio, J. Yorks, and C. Wang (2016), Cirrus cloud optical and microphysical property retrievals from eMAS during SEAC⁴RS using bi-spectral reflectance measurements within the 1.88 μm water vapor absorption band, *Atmos. Meas. Tech.*, *9*, 1743–1753, doi:10.5194/amt-9-1743-2016
- Miller, S. D., J. M. Forsythe, P. T. Partain, J. M. Haynes, R. L. Bankert, M. Sengupta, C. Mitrescu, J. D. Hawkins, and T. H. Vonder Haar (2014), Estimating Three-Dimensional Cloud Structure via Statistically Blended Satellite Observations, *J. Appl. Meteorol. Climatol.*, *53*(2), 437–455, doi:10.1175/JAMC-D-13-070.1.
- Minnis, P., S. Sun-Mack, D. F. Young, P. W. Heck, D. P. Garber, Y. Chen, D. A. Spangenberg, R. F. Arduini, Q. Z. Trepte, W. L. Smith, Jr., J. K. Ayers, S. C. Gibson, W. F. Miller, V. Chakrapani, Y. Takano, K.-N. Liou, and Y. Xie (2011), CERES Edition-2 Cloud Property Retrievals Using TRMM VIRS and Terra and Aqua MODIS Data—Part I: Algorithms, *IEEE Trans. Geosci. Remote Sens.*, *49*(11), 4374–4400, doi:10.1109/TGRS.2011.2144601.

- Mlawer, E. J., and S. A. Clough (1997), On the extension of rapid radiative transfer model to the shortwave region, in *In Proceedings of the Sixth Atmospheric Radiation (ARM) Science Team Meeting*, pp. 223–226.
- Oreopoulos, L., A. Marshak, R. F. Cahalan, and G. Wen (2000), Cloud three-dimensional effects evidenced in Landsat spatial power spectra and autocorrelation functions, *J. Geophys. Res.*, *105*(D11), 14777, doi:10.1029/2000JD900153.
- Pilewskie, P., J. Pommier, R. Bergstrom, W. Gore, S. Howard, M. Rabbette, B. Schmid, P. V. Hobbs, and S. C. Tsay (2003), Solar spectral radiative forcing during the Southern African Regional Science Initiative, *J. Geophys. Res.*, *108*(D13), 8486, doi:10.1029/2002JD002411.
- Platnick, S. (2001), Approximations for horizontal photon transport in cloud remote sensing problems, *J. Quant. Spectrosc. Radiat. Transf.*, *68*(1), 75–99, doi:10.1016/S0022-4073(00)00016-9.
- Platnick, S., M. D. King, S. A. Ackerman, W. P. Menzel, B. A. Baum, J. C. Riedi, and R. A. Frey (2003), The MODIS cloud products: Algorithms and examples from Terra. *IEEE Trans. Geosci. Remote Sens.*, *41*, 459–473..
- Randall, D. A., R. A. Wood, S. Bony, R. Colman, T. Fichefet, J. Fyfe, V. Kattsov, A. Pitman, J. Shukla, and J. Srinivasan (2007), Climate models and their evaluation, in *Climate Change 2007: The physical science basis. Contribution of Working Group I to the Fourth Assessment Report of the IPCC (FAR)*, pp. 589–662, Cambridge University Press.
- Rothman, L. S., D. Jacquemart, A. Barbe, D. C. Benner, M. Birk, L. R. Brown, M. R. Carleer, C. Chackerian, Jr., K. Chance, L. H. Coudert, V. Dana, V. M. Devic, J.-M. Flaud, R. R. Gamache, A. Goldman, J.-M. Hartmann, K. W. Jucks, A. G. Maki, J.-Y. Mandin, S. T. Massie, J. Orphal, A. Perrin, C. P. Rinsland, M. A. H. Smith, J. Tennyson, R. N. Tolchenov, R. A. Toth, J. V. Auwera, P. Varanasi, and G. Wagner (2005), The HITRAN 2004 molecular spectroscopic database, *J. Quant. Spectrosc. Radiat. Transf.*, *96*(2), 139–204, doi:10.1016/j.jqsrt.2004.10.008.
- Sadowy, G. A., A. C. Berkun, W. Chun, E. Im, and S. L. Durden (2003), Development of an advanced airborne precipitation radar, *Microw. J.*, *46*(1), 84–86.
- Schaaf, C. B., F. Gao, A. H. Strahler, W. Lucht, X. Li, T. Tsang, N. C. Strugnell, X. Zhang, Y. Jin, J. P. Muller, P. Lewis, M. Barnsley, P. Hobson, M. Disney, G. Roberts, M. Dunderdale, C. Doll, R. d'Entremont, B. Hu, S. Liang, and J. L. Privette, and D. P. Roy (2002), First operational BRDF, albedo and nadir reflectance products from MODIS, *Remote Sens. Environ.*, *83*, 135–148.
- Schaaf, C. B., J. Liu, F. Gao, and A. H. Strahler (2011), Aqua and Terra MODIS albedo and reflectance anisotropy products, in *Land Remote Sensing and Global Environmental Change: NASA's Earth Observing System and the Science of ASTER and MODIS*, Remote Sensing and Digital Image Processing Series, Vol.11, B. Ramachandran, C. Justice, and M. Abrams, Eds, Springer-Cerlag, 549–561.
- Schafer, J. S., T. F. Eck, B. N. Holben, K. L. Thornhill, B. E. Anderson, A. Sinyuk, D. M. Giles, E. L. Winstead, L. D. Ziemba, A. J. Beyersdorf, P. R. Kenny, A. Smirnov, and I. Slutsker (2014), Intercomparison of aerosol single-scattering albedo derived from

- AERONET surface radiometers and LARGE in situ aircraft profiles during the 2011 DRAGON-MD and DISCOVER-AQ experiments, *J. Geophys. Res. Atmos.*, *119*(12), 7439–7452, doi:10.1002/2013JD021166.
- Scheirer, R., and A. Macke (2003), Cloud inhomogeneity and broadband solar fluxes, *J. Geophys. Res.*, *108*(D19), 4599, doi:10.1029/2002JD003321.
- Schmidt, K. S., P. Pilewskie, S. Platnick, G. Wind, P. Yang, and M. Wendisch (2007a), Comparing irradiance fields derived from Moderate Resolution Imaging Spectroradiometer airborne simulator cirrus cloud retrievals with solar spectral flux radiometer measurements, *J. Geophys. Res.*, *112*(D24), D24206, doi:10.1029/2007JD008711.
- Schmidt, K. S., V. Venema, F. Di Giuseppe, R. Scheirer, M. Wendisch, and P. Pilewskie (2007b), Reproducing cloud microphysical and irradiance measurements using three 3D cloud generators, *Q. J. R. Meteorol. Soc.*, *133*(624), 765–780, doi:10.1002/qj.53.
- Schmidt, K. S., G. Feingold, P. Pilewskie, H. Jiang, O. Coddington, and M. Wendisch (2009), Irradiance in polluted cumulus fields: Measured and modeled cloud-aerosol effects, *Geophys. Res. Lett.*, *36*, L07804, doi:10.1029/2008GL036848.
- Schmidt, K. S., E. Bierwirth, O. Coddington, P. Pilewskie, M. Wendisch, R. Bergstrom, W. Gore, J. Redemann, J. Livingston, and P. Russell (2010a), A new method for deriving aerosol solar radiative forcing and its first application within MILAGRO/INTEX-B, *Atmos. Chem. Phys.*, *10*(16), 7829–7843, doi:10.5194/acp-10-7829-2010.
- Schmidt, K. S., P. Pilewskie, B. Mayer, M. Wendisch, B. Kindel, S. Platnick, M. D. King, G. Wind, G. T. Arnold, L. Tian, G. Heymsfield, and H. Kalesse (2010b), Apparent absorption of solar spectral irradiance in heterogeneous ice clouds, *J. Geophys. Res.*, *115*(D10), D00J22, doi:10.1029/2009JD013124.
- Schmidt, K. S., S. Song, G. Feingold, P. Pilewskie, and O. Coddington (2014), Relating shortwave passive remote sensing and radiative effects of aerosol-immersed broken cloud fields, Presented at the *14th Conference on Atmospheric Radiation*, American Meteorological Society, Boston, July 2014.
- Schmidt, S., and P. Pilewskie (2012), Airborne measurements of spectral shortwave radiation in cloud and aerosol remote sensing and energy budget studies, in *Light Scattering Reviews, Vol. 6 SE - 6*, edited by A. A. Kokhanovsky, pp. 239–288, Springer Berlin Heidelberg.
- Song, S., K. S. Schmidt, P. Pilewskie, M. D. King, A. K. Heidinger, A. Walther, H. Iwabuchi, and O. M. Coddington (2016a), The spectral signature of cloud spatial structure in shortwave irradiance, *Atmos. Chem. Phys. Discuss.*, 1–42, doi:10.5194/acp-2015-911.
- Song, S., K. S. Schmidt, P. Pilewskie, M. D. King, and S. Platnick (2016b), Quantifying the spectral signature of heterogeneous clouds in shortwave radiation measurements, *to be submitted to J. Geophys. Res. Atmos.*, in preparation.
- Stamnes, K., S.-C. Tsay, W. Wiscombe, and K. Jayaweera (1988), Numerically stable algorithm for discrete-ordinate-method radiative transfer in multiple scattering and emitting layered media, *Appl. Opt.*, *27*(12), 2502, doi:10.1364/AO.27.002502.
- Stephens, G. L., S.-C. Tsay, P. W. Stackhouse, and P. J. Flatau (1990), The relevance of the

- microphysical and radiative properties of cirrus clouds to climate and climatic feedback, *J. Atmos. Sci.*, 47(14), 1742–1754, doi:10.1175/1520-0469(1990)047<1742:TROTMA>2.0.CO;2.
- Titov, G. A. (1998), Radiative horizontal transport and absorption in stratocumulus clouds, *J. Atmos. Sci.*, 55(15), 2549–2560, doi:10.1175/1520-0469(1998)055<2549:RHTAAI>2.0.CO;2.
- Toon, O. B., D. O. Starr, E. J. Jensen, P. A. Newman, S. Platnick, M. R. Schoeberl, P. O. Wennberg, S. C. Wofsy, M. J. Kurylo, H. Maring, K. W. Jucks, M. S. Craig, M. F. Vasques, L. Pfister, K. H. Rosenlof, H. B. Selkirk, P. R. Colarco, S. R. Kawa, G. G. Mace, P. Minnis, and K. E. Pickering (2010), Planning, implementation, and first results of the Tropical Composition, Cloud and Climate Coupling Experiment (TC⁴), *J. Geophys. Res.*, 115(D10), D00J04, doi:10.1029/2009JD013073.
- Toon, O. B., H. Maring, J. Dibb, R. Ferrare, D. J. Jacob, E. J. Jensen, Z. J. Luo, G. G. Mace, L. L. Pan, L. Pfister, K. H. Rosenlof, J. S. Redemann, J. S. Reid, H. B. Singh, R. Yokelson, G. Chen, K. W. Jucks, and A. Pszenny (2015), Planning, implementation and scientific goals of the Studies of Emissions and Atmospheric Composition, Clouds and Climate Coupling by Regional Surveys (SEAC⁴RS) field mission, *Submitt. to J. Geophys. Res.*
- Várnai, T., and A. Marshak (2009), MODIS observations of enhanced clear sky reflectance near clouds, *Geophys. Res. Lett.*, 36(6), L06807, doi:10.1029/2008GL037089.
- Várnai, T., and A. Marshak (2015), Effect of Cloud Fraction on Near-Cloud Aerosol Behavior in the MODIS Atmospheric Correction Ocean Color Product. *Remote Sensing*, 7(5): 5283-5299, doi:10.3390/rs70505283
- Virkkula, A., N. C. Ahlquist, D. S. Covert, P. J. Sheridan, W. P. Arnott, and J. A. Ogren (2005), A Three-Wavelength Optical Extinction Cell for Measuring Aerosol Light Extinction and Its Application to Determining Light Absorption Coefficient, *Aerosol Sci. Technol.*, 39(1), 52–67, doi:10.1080/027868290901918.
- Walther, A., and A. K. Heidinger (2012), Implementation of the Daytime Cloud Optical and Microphysical Properties Algorithm (DCOMP) in PATMOS-x, *J. Appl. Meteorol. Climatol.*, 51(7), 1371–1390, doi:10.1175/JAMC-D-11-0108.1.
- Wang, W., S. Liang, and T. Meyers (2008), Validating MODIS land surface temperature products using long-term nighttime ground measurements, *Remote Sens. Environ.*, 112(3), 623–635, doi:10.1016/j.rse.2007.05.024.
- Welch, R. M., S. K. Cox, and J. M. Davis (1980), Solar radiation and clouds, *Meteorol. Monogr.*, 17, 1–96.
- Wen, G., A. Marshak, R. F. Cahalan, L. A. Remer, and R. G. Kleidman (2007), 3-D aerosol-cloud radiative interaction observed in collocated MODIS and ASTER images of cumulus cloud fields, *J. Geophys. Res. Atmos.*, 112(D13), D13204, doi:10.1029/2006JD008267.
- Wen, G., A. Marshak, and R. F. Cahalan (2008), Importance of molecular Rayleigh scattering in the enhancement of clear sky reflectance in the vicinity of boundary layer cumulus clouds, *J. Geophys. Res.*, 113(D24), D24207, doi:10.1029/2008JD010592.

- Wendisch, M., D. Müller, D. Schell, and J. Heintzenberg (2001), An Airborne Spectral Albedometer with Active Horizontal Stabilization, *J. Atmos. Ocean. Technol.*, *18*(11), 1856–1866, doi:10.1175/1520-0426(2001)018<1856:AASAWA>2.0.CO;2.
- Wielicki, B. A., B. R. Barkstrom, E. F. Harrison, R. B. Lee, G. L. Smith, and J. E. Cooper (1996), Clouds and the Earth's Radiant Energy System (CERES): An Earth Observing System Experiment, *Bull. Am. Meteorol. Soc.*, *77*(5), 853–868, doi:10.1175/1520-0477(1996)077<0853:CATERE>2.0.CO;2.
- Wiscombe, W. J. (1980), Improved Mie scattering algorithms, *Appl. Opt.*, *19*(9), 1505, doi:10.1364/AO.19.001505.
- Wiscombe, W. J., R. M. Welch, and W. D. Hall (1984), The effects of very large drops on cloud absorption. Part I: Parcel models, *J. Atmos. Sci.*, *41*(8), 1336–1355, doi:10.1175/1520-0469(1984)041<1336:TEOVLD>2.0.CO;2.
- Zelenka, A., R. Perez, R. Seals, and D. Renné (1999), Effective accuracy of satellite-derived hourly irradiances, *Theor. Appl. Climatol.*, *62*(3-4), 199–207, doi:10.1007/s007040050084.
- Zender, C. (2001), Radiative transfer in the Earth system, *GNU Free Doc. Licens.*
- Zhang, Z., S. Platnick, P. Yang, A. K. Heidinger, and J. M. Comstock (2010), Effects of ice particle size vertical inhomogeneity on the passive remote sensing of ice clouds, *J. Geophys. Res.*, *115*(D17), D17203, doi:10.1029/2010JD013835.
- Zinner, T., and B. Mayer (2006), Remote sensing of stratocumulus clouds: Uncertainties and biases due to inhomogeneity, *J. Geophys. Res.*, *111*(D14), D14209, doi:10.1029/2005JD006955.
- Zuidema, P., and K. F. Evans (1998), On the validity of the independent pixel approximation for boundary layer clouds observed during ASTEX, *J. Geophys. Res.*, *103*(D6), 6059, doi:10.1029/98JD00080.